Spring 2021

HF Radar Signal Inversion for Wind and Swell Ocean Waves

Zaid Rahman Abed Al-Attabi

HF Radar Signal Inversion for Wind and Swell Ocean Waves

by

Zaid Rahman Abed Al-Attabi

Bachelor of Science
University of Basrah, 2007

Master of Science
University of Basrah, 2009

Submitted in Partial Fulfillment of the Requirements

For the Degree of Doctor of Philosophy in

Geological Sciences

School of the Earth, Ocean and Environment

University of South Carolina

2021

Accepted by:

George Voulgaris, Major Advisor

Alexander Yankovsky, Committee Member

Subrahmanyam Bulusu, Committee Member

Dana K. Savidge, Committee Member

Tracey L. Weldon, Interim Vice Provost and Dean of the Graduate School

DEDICATION

This dissertation is dedicated to my beloveds; My mother, My father, My wife, My Brothers and Sisters, and My Nieces.

ACKNOWLEDGEMENTS

This dissertation is a representation of my work on the project that I conducted in the last 6 years, and without support and help from many individuals, it could not have been possible to complete this study. First and foremost, I would like to express my sincere and profound gratitude for the supervision of professor Dr. George Voulgaris for outstanding leadership, his constant support, guidance, encouragement, valuable suggestions that he has given throughout different stages of the research. During these years in this study, Dr. Voulgaris showed much patience in his supervision. He was generous in that his office door and his house were always open to me for discussions about my work, and he was patient in answering my questions. He was straightforward with his opinion on me and measuring my productivity, and that certainly increased my confidence and knowledge in the field of HF radar. He provided me with insights and solid foundations that are now part of my knowledge. It has been a great opportunity and honor for me to work with him and be his PhD student.

My deep gratitude also goes to Dr. Nirnimesh Kumar who is no longer with us. Kumar was on my PhD committee as the external committee member for my qualifying and comprehensive exams. He was a wonderfully supportive mentor to me and many others. He helped me since the very beginning of my PhD program. Although I spent very limited time with him, he made a strong impression on me: hardworking, responsible, intelligent, gentle, and kind. He was very giving and enthusiastic, wonderful human being.

He gave me some ideas on how to write a code to do an analysis. I'm grateful and lucky enough for having had a chance to know him. May his soul rest in peace.

I would further like to extend my thanks and my sincere appreciation to my committee members: Associate Professor Dr. Dana K. Savidge for agreeing and taking the time to be the external committee member for my dissertation defense, Professor Dr. Alexander Yankovsky, and Professor Dr. Subrahmanyam Bulusu for their agreement to critically review this document at the early stages, and evaluating this dissertation and providing valuable suggestions, and helpful advice and discussion. Their participation helped in improving the quality of the research work to be as in this final form.

Special thanks are also owed to my colleagues in our Coastal Processes and Sediment Dynamics (CPSD) Lab for their constant encouragement, support, and friendship, especially Douglas Cahl, lab mate and co-author, for his insight, and his sharing ideas and programming and coding skills with me and other aspects at various phases of the work; Conor Ofsthun for helping me during my daily life, his kindness, generosity, supporting me and make me feel at home and between my family, we have tried to motivate each other to achieve our own goals; Xiaodong Wu for sharing some ideas, valuable discussion, and friendship. I always obtain help from him even when I don't ask.

I would like to express sincere thanks and gratitude to Jeff Jefferson for his technical assistance in fixing my workstation computer and network troubleshooting at any time throughout the research period. I would like to thank Mrs. Stephanie Bradley for being very helpful and making life easier with all the official paperwork and supporting me during the difficulties faced throughout my time here.

Finally, I would like to express sincere gratitude and deep appreciation to my family: my great mother Lyla Abdul Hassan and my dear father Rahman Abed Al-Attabi, for their constant encouragement and support, and patience being away from them for 7 years; my wonderful wife Brittany Al-Attabi for her patience, understanding and support, and for always being there for me; my brothers Aysar, Hyder, and Ali, especially Aysar for being always with me and for me; and my sisters, Israa, Maha, and Hala for their unconditional love, believing in me, affection, and support which helped me to reach this point in my life and career. This work could not have been completed without all of their love and support.

I gratefully acknowledge the financial support provided by the Higher Committee for Education Development in Iraq (HCED) and for offering me the scholarship. I owe my appreciation to my professors and colleagues at the University of Basrah/Marine Science Center and the Iraqi Cultural Office at Washington DC for their continuous support. The experimental work was also funded by the Carolinas Coastal Processes Project, a cooperative study supported by the U.S. Geological Survey Award G03AC00007. This work is also supported by the Southeast Coastal Observing Regional Association (SECOORA) pursuant to NOAA Award NA16NOS0120028 for data analysis and preparation for my publications. I would like to thank the faculty members of School of the Earth, Ocean and Environment for providing the opportunity to accomplish this work and for offering me Research Assistant during the summer semesters. Thanks are also owed the Department of Physics and Astronomy for offering me teaching assistantships.

ABSTRACT

Although High Frequency (HF) radars are used routinely for measuring ocean surface currents at high spatial and temporal resolution, their utilization for estimating ocean wave spectra is still limited, mainly because of the lack of extensive evaluation of the accuracy of wave inversion models, and lack of well-established methods, especially if swell is present in the area of study. Estimation of surface currents is based on analyzing the signal of the first-order Bragg peak, while extraction of wave information requires analysis of the signal contained in the second-order continuum of the Doppler spectra; its quality depends on a number of environmental (i.e., noise levels, ocean wave energy) and system-based (i.e., frequency of operation, range, azimuthal angle, etc.) parameters. A number of theoretical and empirical inversion methods have been developed to estimate wave parameters from the HF radar data, with the latter one being more attractive for routine operations due to easier implementation and reduced computational cost. Further, most research on HF radar wave inversion has been limited to <30 MHz radar frequency. In this dissertation, a hybrid radar wave inversion method that treats swell and wind waves separately is introduced and evaluated using a single Very High Frequency (VHF) 48 MHz radar site, two High Frequency (HF) 12 MHz radar sites, and in situ wave measurements.

Using a single VHF (48 MHz) covering the nearshore and in situ directional wave data from ranges between 0.7 and 4.2 km and beam angles between 22.3 and 55.8 deg, it

was concluded that wind wave inversion of the second-order spectra requires normalization by using Barrick's (1977b) weighting function. This removes no wind-wave energies from the second harmonic and corner reflection peaks and leads to better wave estimations. However, at lower operating frequencies the normalization removes some of the wind wave energy something that needs to be accounted for. Application of the weighting function in the wind wave inversion model results in empirical wind-wave regression coefficient that is not wave frequency-dependent and of similar in magnitude to those found in studies that used different radar operating frequencies but included the weighting function in the inversion. This is further confirmed using data from 12 MHz system sampling ocean conditions with significant swell energy being present at times.

The applicability of the empirical wave inversion method to increase the accuracy of the estimation of ocean wave spectra and wave bulk parameters by accounting for the presence of swell waves is examined and presented. The ability of the method to estimate wave directional spectra and bulk wave parameters from inverting Doppler spectra are investigated. Doppler spectra from single beam/site and two beams/sites WERA HF radar system operated with frequency 12 MHz are used over a one-month (March 30th-April 27th, 2012) data collection. Within the radar footprint, in situ wave spectra were collected using a buoy deployed offshore of the north coast of Cornwall in the UK, and used for comparisons.

To examine the influence of swell, three different swell inversion models developed by Lipa et al. (1981), Wang et al. (2016), and an empirical method, denoted as LPM, WFG, and EMP respectively are presented and evaluated. The methods were evaluated using (1) a single beam from a single radar site, (2) two beams from a single

radar site, and (3) two beams from two radar sites intersecting each other at the buoy location. The LPM swell method for two beams from two sites scenario was found to be the most accurate in estimating swell parameters (RMS Error of 0.24m), the inverted swell height correlated well with the partitioned in situ swell measurements. The swell spectrum can be reconstructed from the inverted swell wave heights and combined with the wind wave inversion results to create the total directional wave spectrum. The method presented in this dissertation is fully dependent on information from HF radar data and does not no need calibration against in situ data for implementation; it can be applied to any beam forming system and operating frequency.

TABLE OF CONTENTS

LIST OF TABLES

LIST OF FIGURES

CHAPTER 1

INTRODUCTION

1.1 Introduction

HF radar is an advanced shore-based instrument originally designed for mapping ocean surface currents over large coastal ocean regions. HF radars are able to cover large areas of the ocean (tens to hundreds of kilometers of range) with a resolution that depends on operating frequency and bandwidth. Their temporal resolution varies from a few hours to only 30 minutes depending on the need for averaging which in turn depends on the type of the system (direction-finding vs beam-forming) (Gurgel et al., 2006; Padaun and Washburn, 2013). Because of their relative easiness of deployment, maintenance, and operational efficiency they have been useful not only for a number of operational oceanographic applications (i.e., search and rescue operations, Bjorkstedt and Roughgarden, 1997; ship tracking, Dzvonkovskaya et al., 2008; iceberg monitoring, Srivastava and Ponsford, 1991; and identifying tsunamis approaching the coastline, Gurgel et al., 2011), but also for scientific investigations (e.g., identifying larval movement, Graber and Limouzy-Paris, 1997; monitoring of tidal flows, Wyatt, 2007).

The signal recorded by HF radars contains information about sea surface state and the extraction of the associated wave parameters has been the subject of numerous studies dating back to the seventies (e.g., Barrick, 1977a; Long and Trizna, 1973; and Lipa and Barrick, 1980 among others). However, the wave information is non-linearly convoluted with the backscattered EM signal and wave inversion has been challenging and not widely available to the scientific community although HFs were manufacturers that provide software for this. Data collected from HF radars can be combined with data from other sources such as; satellites, buoys, drifters, and mooring and can increase the

availability of high-quality sea state data, which can be used in numerical ocean modeling and for operational activities (Voulgaris et al., 2008).

HF radars are unique as they are able to provide data with spatial resolution similar to that of numerical models. Ocean surface currents estimated from HF radars are already being used in ocean modeling (data assimilation) to enhance forecasting accuracy (e.g., Barth et al., 2008). However, this is not the case for waves and currently the ocean wave modeling community relies on single point measurements from wave buoys. Improvement of the HF radar wave inversion methods is desirable as it would allow the estimation of wave parameters with a spatial resolution similar to that available for surface currents and for the identification of spatial gradients in wave conditions that could be assimilated into wave propagation models.

1.2 Objectives

The overall objective of this research is to develop a reliable and computationally effective wave inversion method that can be used to invert HF radar signal to obtain directional wave spectra and bulk wave parameters. The method needs to be simple and computational effective something that empirical methods usually achieve, but at the same time it should have a sound theoretical basis so that it can be applied to any HF radar independently of operational frequency and without the need for in situ calibration. It should be noted that this study focuses on beam forming systems as these systems are capable to provide wave information from a particular patch of the ocean with limited spatial averaging. The second-order spectrum continuum in direction finding systems is spatially integrated (along a circular arc at a particular range) providing spatially averaged signals that do not allow estimation of wave spatial gradients. In this

dissertation, existing methods are analyzed and tested against data from two different beam-forming HF radar systems: (i) a single VHF (48 MHz) system and (ii) a pair of HF (12 MHz) systems.

The research carried out to achieve the above stated overall objective is split into separate goals / specific objectives presented in Chapters 3 and 4 Following this introductory chapter, Chapter 2 describes the principle of operation of the HF radars as well as the different types of radars (i.e., beam-forming and direction-finding) available to the community. The scattering theory of the emitted electromagnetic (EM) waves and their interaction with ocean waves to generate the second-order signal used for wave inversion is presented with some detail.

Chapter 3 focuses on the ability of a single VHF radar system to predict directional wind wave conditions in the nearshore. The various empirical methods introduced are tested against in situ data and a new hybrid empirical method that accounts for swell and wave conditions separately is introduced. The method developed in Chapter 3 is further expanded to more general, offshore swell conditions in Chapter 4. In Chapter 4, the focus is placed on the best method to extract swell waves and existing methods are evaluated against data from a 12 MHz system and for a variety of swell conditions. In addition, the wind wave module developed in Chapter 3 for a 48 MHz system is also evaluated to test its robustness for use with beamforming HF radars of different operational frequency, without the need for in situ calibration.

Finally, Chapter 5 provides a summary of the main findings of this work and presents some recommendations for areas requiring further investigation.

CHAPTER 2

REVIEW

2.1 Radar Principle of Operation

HF radars are shore-based remote sensing systems developed during World War II (Crombie, 1955) and their principle is based on the well-known phenomenon of Bragg scattering (Crombie, 1955). HF radars transmit vertically polarized electromagnetic (EM) waves of a particular frequency. These EM waves are coupled with the highly conductive ocean surface (ground waves) reaching areas behind the horizon. The salinity of the ocean surface provides a suitable, highly conductive medium guide for the electromagnetic waves; the higher the salinity, the more conductive the medium and higher the range low power HF radars can cover. Bragg scattering in the ocean is the result of the interaction between the transmitted electromagnetic EM waves and ocean waves with a wavelength half that of the transmitted EM waves, which leads to scattering of the emitted electromagnetic waves back as given by:

$$\lambda_{EM} = 2\lambda_B \cos(\theta) \tag{2.1}$$

where θ is the grazing angle of the EM wave and λ_{EM} and λ_B are the wavelengths of EM and Bragg waves, respectively (see Figure 2.1). At very small grazing angles (i.e., radar transmitter array close to ocean surface), the angle between the incident EM waves and the ocean is nearly zero, so that we can write:

$$\lambda_{EM} = 2\lambda_B \tag{2.2}$$

The expression for the received backscattered power is given as (Barrick, 1972):

$$P_R = \frac{P_T G_T G_R F^2 \lambda^2 \sigma_o}{(4\pi)^3 r_T^2 r_R^2} \, . dA \tag{2.3}$$

In the equation above F is the Norton field attenuation factor over sea, that dependents on radar frequency, propagation distance, transmit and receive antenna gain and signal attenuation. It describes total signal loss due to the finite conductivity of sea water, earth's curvature, and sea surface roughness. P_T and P_R are the transmitted and received power, while G_T and , G_R are the gain factors for the transmit and receive antennas. r_R is the distance from transmitter to target and r_T from the target to receiver (r_R= r_T for monostatic systems), σ_o is the averaged radar cross section per unit area, λ is radar wavelength, and dA is the ocean surface area the signal is backscattered from (ocean patch).

2.2 Radar Configurations (Beam-forming and Direction-finding)

HF radar systems are classified into two types based on the method used to analyze the received signals: beam-forming and direction-finding radar systems.

Beam-forming radar systems use an array of spatially separated antennas (usually an equally spaced linear array). The signal received by the antenna array is be steered electronically to a specific direction (azimuth) through the application of phase shifts on the signals received by each antenna. Direction-finding radar systems calculate the direction of the Bragg scattered frequencies using a direction-finding algorithm, which allows for more diverse antenna configurations. These algorithms can exploit the directional properties of loop antennas for use in antenna arrays that cannot beamform but are capable of direction-finding.

The most common commercially available system, at least in the US, utilizes the direction-finding algorithms and uses a single pole transmitter antenna and a compact receiver consisting of three antennas (two antennas as a cross-loops element, and one antenna as omnidirectional monopole element (Barrick, 2008). These systems were developed by Barrick et al. (1977) at NOAA Wave propagation Laboratory and are known as Coastal Ocean Dynamics Applications Radar-CODAR. For each range ring sector, the azimuth of the surface current radial velocities is obtained using least squares method (Lipa and Barrick, 1986) or Multiple Signal Classification technique-MUSIC (Schmidt, 1986). Different configurations of antennas can also be used as described in detail in Kirincich et al. (2019).

Traditional beam-forming systems consist of a linear receiver array of antennas (8-16 elements) and a transmit antenna system separated by a distance from the receiver unit. Although a number of beam-forming radars have been developed over the years (i.e., PISCES, Wyatt et al., 2003, 2006, 2011; OSCR, Hammond et al., 1987) the latest commercially available beam-forming or phased array radar system are based on the design at the University of Hamburg by Gurgel et al. (1999) who called it WEllen RAdar (WERA). WERA systems transmit a frequency modulated continuous wave (FMCW), requiring a separation between the transmit and receive arrays. CODAR systems gate the FMCW signal, frequency modulated interrupted continuous wave (FMICW), thereby allowing the same antenna array to be used to transmit and receive. In both systems, the range is calculated by measuring the frequency difference between the transmitted and received signals which relates to range (Paduan and Washburn, 2013; Helzel and

Kniephoff, 2010; Teague et al., 1997; Gopalakrishnan, 2008; Laws, 2001; Gurgel et al., 1999; Wang and Gill, 2016).

The backscatter signal for each EM transmission is first FFTed to be sorted into ranges and then for each range a time-series is created (Gurgel and Schlick, 2009; Gurgel et al., 2003). This latter time-series is used to estimate the Doppler spectrum for the particular range and azimuth. The width of the Bragg peaks present in the Doppler spectra depends on the system/method used (beam-forming vs. direction-finding). Beam forming systems steer the beam to a particular direction and thus the signal is from a limited, single sector of the sea surface (Graber et al., 1997). In direction-finding systems, the return signals are scattered from a range of sectors (range ring) leading to wider peaks that could merge with the second-order region of the spectrum that carries the information on ocean waves. This and the fact that the whole second-order spectrum is averaged over a larger sector for direction finding systems makes beam-forming a better approach for obtaining information on ocean waves.

2.3 First and Second-order spectra

The Doppler backscatter spectrum is characterized by two main peaks (Bragg peaks, first-order spectra) and the regions on either side of the Bragg peaks (second-order spectra) as shown in Figure 2.2. The two regions represent different interaction mechanisms between the emitted EM signal and surface ocean waves.

First-order Bragg peaks appear as the two largest and narrowest peaks and assuming no surface current is present correspond to the frequency (Bragg frequency, f_B) of the ocean wave with wave length (λ_B). This frequency represents the Doppler shift of

the EM waves due to the phase speed of the Bragg ocean waves (see Figure 2.2). The positive and negative first-order Bragg peaks correspond to Doppler shifts induced by ocean waves that travel toward and away from the radar site, respectively. When a radial current is present in the ocean the frequency of the first-order peaks would be shifted from the theoretical Bragg frequency ($f_B = \sqrt{g/2\pi\lambda_r}$, where λ_r is radar wavelength). This shift in frequency corresponds to shift in the wave celerity of the ocean Bragg wave due to surface currents and it is used to estimate the latter in the direction of the radar beam (radial current).

Second-order spectra are the continuum spectra found around each side of the Bragg peaks. They are the result of the nonlinear interaction between the EM and ocean waves. This part of the spectrum contains all information pertaining to ocean waves (Hasselmann, 1971) and these nonlinear effects are attributed to two different types of interactions as shown, schematically, in Figure 2.3. First, the interaction between EM and ocean waves (Bragg waves) with a wavenumber the same as the Bragg wavenumber, k_B, which are generated by the interaction of two ocean waves with wave numbers $k_1$and k_2, such that they satisfy the condition $k_B = k_1 + k_2$, where $k_B = -2k_o$, with k_o being the radar wavenumber (Figure 2.3a). This process is called hydrodynamic coupling interaction. Another interaction occurs between an incident radar EM wave and two ocean waves at directions such that the projection of their wavelength along the direction of the incident EM wave is equal to the wavelength of a Bragg wave (Figure 2.3b). In this case, the incident EM waves interact with ocean waves that have wavenumber (k_{B1}) and create a scattered EM wave. Part of this already scattered EM wave interacts again with another Bragg ocean wave (k_{B2}) and the scattered wave propagates toward the radar

receivers. This process is known as an electromagnetic coupling effect. The second-order spectra resemble the shape of ocean wave spectra and information about the ocean wave parameters can be estimated by inverting these second-order spectra.

The first theoretical description of radar backscatter wave spectra was proposed by Barrick (1971,1972a, b) who derived a mathematical expression for the first and second-order cross sections of scattered waves based on perturbation analysis. The first order cross section (σ_1) is given by:

$$\sigma_1(f_D) = 2^6\pi k_o^4 \sum_{m_1=\pm 1} S(m_1\overrightarrow{k_B})\delta(f_D - m_1 f_B) \tag{2.4}$$

The second-order cross section (σ_2) includes the spectral density at each wave frequency from the product of two wave spectra with wave numbers $\overrightarrow{k_1}$ and $\overrightarrow{k_2}$ and was derived for short waves. Its expression for deep water is:

$$\sigma_2(f_D) = 2^6\pi k_o^4 \sum_{m1=\pm 1} \sum_{m2=\pm 1} |\Gamma|^2 S(m_1\overrightarrow{k_1}) S(m_2\overrightarrow{k_2}) \delta(f_D - m_1\sqrt{gk_1} - m_2\sqrt{gk_2}\ ) \tag{2.5}$$

$S(.)$ is the ocean wave spectrum, k_o is the radar wavenumber, $\overrightarrow{k_1}$ and $\overrightarrow{k_2}$ are wave vectors corresponding to two ocean waves that satisfy the Bragg scattering criteria $\overrightarrow{k_1} + \overrightarrow{k_2} = \overrightarrow{k_B}$, where $\overrightarrow{k_B}$ is the vector of Bragg waves ($|k_B| = 2k_o$), f_D and f_B are Doppler and Bragg frequencies respectively, $\delta()$ is Dirac delta function, $m_1 = \pm 1$ denotes the sign of Bragg waves moving toward (+1) or away (-1) from the radar, and $m_2 = \pm 1$ corresponds to the left (-1) and right (+1) sidebands around Bragg peaks. Those regions are numbered by j as:

$$\begin{array}{ll} f_D < -f_B & (j = 1, m_1 = -1, m_2 = -1) \\ -f_B < f_D < 0 & (j = 2, m_1 = -1, m_2 = +1) \\ 0 < f_D < f_B & (j = 3, m_1 = +1, m_2 = -1) \\ f_D > f_B & (j = 4, m_1 = +1, m_2 = +1) \end{array} \quad (2.6)$$

Finally, Γ in eq 2.5 is the total coupling coefficients which contains both the hydrodynamic and electromagnetic effects, Γ_H and Γ_{EM} respectively as $\Gamma = \Gamma_H + \Gamma_{EM}$.

2.4 Wave inversion methods

The applications of HF radar to estimate ocean wave parameters is not as straightforward as for ocean surface current. Wave inversion requires a high signal to noise ratio in contrast with current measurements; the wave information is embedded in the signal of the second-order Doppler spectra which has energy that is much lower than that of first-order peaks used for current. In addition, the second-order spectra can be contaminated with energy leaking from the first-order peaks due to the wave heights that exceed the perturbation limit used for deriving the wave inversion theory (Barrick's limit $k_o H_{rms} < 2.82$); in this case, the second-order spectra are not easily separated from the first-order signal. Finally, second-order signals are produced from non-linear wave interactions which make their inversion method more complicated. Also, it is known that Doppler spectra from beams at high azimuthal angles from the radar boresight (> 45°) are more likely to be of lower quality due to sidelobe effects. When swell is present, the inverted wave measurements from radar show a discrepancy with in situ measurements. This discrepancy is caused by the hydrodynamic interaction wave-wave effect imposed by long wavelength of the swell and the directional dependency of radar data on the angle between the swell direction and the radar beam angle (Lopez et al., 2016; Wyatt, 2002;

Essen et al., 1999; Gurgel et al., 2006; Gomez et al., 2015; Wyatt, 1986, 1999; Heron and Prytz, 2002; Bathgate et al., 2006).

2.4.1 Fundamentals of wave inversion

Extraction of the wave parameters from Doppler spectra has been the subject of numerous theoretical studies dating back to the late 70s (Lipa, 1977, 1978; Wyatt, 1990; Howell and Walsh, 1993; Hisaki, 1996; Lipa and Barrick, 1982). The proposed theoretical inversion methods are time consuming and numerically expensive for daily routine operations. Therefore, numerous attempts have been made to convert them into simpler empirical inversion methods (Barrick, 1977). Barrick's model (1977) states that ocean wave height is proportional to second-order spectra normalized by the first-order Bragg energy and weighted by weighting function. The normalization is necessary to account for signal attenuation with range. Barrick's (1977a, b) and the second-order spectrum can be expressed in terms of ocean wave spectrum using:

$$S(f_D - f_B) = \frac{4\,\sigma_2(f_D)/W(f_D/f_B)}{k_o^2 \int_0^\infty \sigma_1(f_D) df_D} \tag{2.7}$$

where W is a weighting function (see section 3.5.1 for more details), σ_1, σ_2 are first and second cross section spectra, and k_o is radar wave number. Then, RMS ocean wave heights can be estimated as:

$$H_{rms}^2 = \frac{2 \int_0^\infty \sigma_2(f_D) \Big/ W(f_D/f_B)\, df_D}{{k_o}^2 \int_0^\infty \sigma_1(f_D)\, df_D} \tag{2.8}$$

Variations of equation 2.8 have been presented in a number of publications (Heron and Prytz, 2002; Huang et al., 2002; Graber and Heron, 1997; Essen et al., 1999;

Gurgel et al., 2006; Maresca and George, 1980; Heron et al., 1985; Savidge et al., 2011; Ramos, 2006; Toro et al., 2014; Lopez et al., 2016) where the empirical model was evaluated against in situ data.

These empirical inversion methods relied on the determination of regression coefficients suggesting the need for in situ calibration and did not account for variability or dependence on ocean conditions such as swell present, or radar parameters such as angle between beam angle and wave direction. Heron and Heron (1998) compared the original and two variations of Barrick's model (Maresca and Georges (1980) and Heron et al. (1985)) and concluded that Barrick's (1977b) original method provided the best performance when using a constant regression coefficient ($\alpha = 0.3$):

$$H_{rms}{}^2 = \alpha \frac{2R_W}{k_o{}^2} \tag{2.9}$$

where R_W is:

$$R_W = \frac{\int_{-\infty}^{+\infty} \sigma_2(f) \Big/ W(f/f_B)\, df}{\int_{-\infty}^{+\infty} \sigma_1(f)\, df} \tag{2.10}$$

where $f = f_D \pm f_B$. However, they noted that the empirical method is inapplicable when the angle between radar beam and wave direction is within the range of $90^o \pm 15^o$. Gurgel et al. (2006) followed Barrick's inversion method using data from a 27MHz radar and expanded the method to estimate wave energy at different ocean wave frequencies. They derived empirical regression coefficients as a function of wave frequency and suggested that these can be adjusted for use with radars of different operational frequency (f_{radar}) using:

$$\alpha(f) = \left(27.65 \times \frac{10^6}{f_{radar}}\right)^2 \alpha_{27.65} \tag{2.11}$$

Other empirical wave inversions found a constant regression coefficient ($\alpha = 0.34$) (Ramos et al., 2009). Although an empirical inversion ocean wave spectrum has been reported by several literatures, variations and differences of estimated wave height are still obscure and are not well explained.

2.4.2 Swell inversion approach

Swells are characterized by long wave periods and small angular spreading (almost unidirectional propagation). In a one-dimensional wave spectrum, a single swell usually appears as a sharp spectral peak in the lower band of wave frequency while wind waves appear in higher frequency bands and are characterized by broader spectral peaks.

Lipa and Barrick (1980, 1986) showed that the interaction of swells with the EM waves is different than that of wind waves (see Figure 2.4) and the signal is dominated by the swell wavenumber. They developed a swell specific wave inversion algorithm where the second-order cross section and coupling coefficient are solved by considering the interaction of swell and wind wave that produces a backscatter signal that is dominated by the swell. The scenario of swell inversion requires looking for long waves that are not under the influence of the wind and there is no contribution of wind waves. The total ocean wave spectrum S can be partitioned and written as the sum of swell and wind wave spectra, S_s and S_w respectively:

$$S(\vec{k}) = S_w(\vec{k}) + S_s(\vec{k}) \tag{2.12}$$

Based on the theoretical second-order cross section expression Eq. (2.5) which contains the product of two wave spectra (see the double integral in Eq. (2.5)), $S(\vec{k})$ in Eq. (2.12) can be re-written as:

$$S(\vec{k}) = S_w(\overrightarrow{k_1})S_w(\overrightarrow{k_1}) + S_w(m_1\overrightarrow{k_1})S_s(m_2\overrightarrow{k_2}) + S_w(m_2\overrightarrow{k_2})S_s(m_1\overrightarrow{k_1}) + S_s(\overrightarrow{k_2})S_s(\overrightarrow{k_2}) \tag{2.13}$$

The first term ($S_w.S_w$) on the RHS of the equation represents the contribution of wind waves alone which corresponds to the same expression that Barrick (1972) derived for short wave second-order cross section [see Eq. (2.5)]. The last term ($S_s.S_s$) is assumed to be zero as the swell wave number is so small and does not satisfy the required Bragg scattering condition (Forget et al., 1981). The two terms in the middle are equal to each other and can be expressed as $2.S_s(m_2\overrightarrow{k_2})S_w(m_1\overrightarrow{k_1})$; assuming $\overrightarrow{k_2} = \overrightarrow{k_s}$, $\overrightarrow{k_1} = \overrightarrow{k_w}$ and $f_1 = f_w, f_2 = f_s$, the second-order cross section Eq.(2.5) in terms of swell and wind wave interaction can be written as:

$$\sigma_2(f_D) = 2^7\pi k_o^4 \sum_{m_1,m_2=\mp 1} \int_{-\infty}^{\infty} \int_{-\pi}^{\pi} |\Gamma_{m_1m_2}|^2 S(m_1\overrightarrow{k_w})S(m_2\overrightarrow{k_s})\delta(f_D - m_1f_w - m_2f_s)k_2dk_2d\theta \tag{2.14}$$

Where, $\overrightarrow{k_s}$ and $\overrightarrow{k_w}$ are swell and wind wave vector wave numbers respectively, f_s and f_w are swell and wind wave frequencies respectively. The interaction of swell and wind waves should satisfy the scattering condition, such that:

$$\overrightarrow{k_w} + \overrightarrow{k_s} = \overrightarrow{k_B} \tag{2.15}$$

and substituting Eq. (2.15) in Eq. (2.14), the second-order cross section for swell waves can be written as:

$$\sigma_2(f_D) = 2^7 \pi k_o^4 \sum_{m_1,m_2=\mp 1} \int_{-\infty}^{\infty} \int_{-\pi}^{\pi} \left|\Gamma_{m_1,m_2}\right|^2 S\big(m_1(\overrightarrow{k_B} - m_2\overrightarrow{k_s})\big) S\big(m_2\overrightarrow{k_s}\big) \delta(f_D - m_1 f_w - m_2 f_s) k_s dk_s d\theta \tag{2.16}$$

The effect of wind waves, $S\big(m_1(\overrightarrow{k_B} - m_2\overrightarrow{k_s})\big)$ term in Eq. (2.16), can be eliminated by normalizing $\sigma_2(f_D)$ by the integral of first-order cross section $\sigma_1(f_D)$, which represents the power of Bragg peak region, and then Eq. (2.16) becomes:

$$\mathcal{R}_{m_1,m_2}(f_D) = 2 \sum_{m_1,m_2=\mp 1} \int_{-\infty}^{\infty} \int_{-\pi}^{\pi} \left|\Gamma_{m_1,m_2}\right|^2 S\big(m_2\,\overrightarrow{k_s}\big)\, C_{m_1,m_2} \delta(f_D - m_1 f_w - m_2 f_s) k_s dk_s d\theta \tag{2.17}$$

where, $\mathcal{R}_{m_1,m_2}$ is the theoretical normalized energy of second-order swell peaks, and C_{m_1,m_2} is a residual term that accounts for the background wave signal which is mainly due to wind waves and is given by:

$$C_{m_1,m_2} = \frac{S\big(m_1(\overrightarrow{k_B} - m_2\overrightarrow{k_s})\big)}{S\big(m_1\overrightarrow{k_B}\big)} \tag{2.18}$$

Since $k_s \ll k_w$ (see Figure 2.4), the condition $\overrightarrow{k_w} + \overrightarrow{k_s} = \overrightarrow{k_B}$, reduces to $\overrightarrow{k_w} \cong \overrightarrow{k_B}$. Thus, the term $S\big(m_1(\overrightarrow{k_B} - m_2\overrightarrow{k_s})\big)$ in Eq 2.18 becomes approximately equal to $S\big(m_1\overrightarrow{k_B}\big)$ (see Figure 1.3), so that $C_{m_1,m_2} \sim 1$ (Lipa et al., 1981).

More details of swell inversion wave heigh can be found in Chapter 4.2 of this dissertation. Based on the theory of swell scattering and inversion proposed by Lipa and Barrick (1980), several swell inversion models were developed (Lipa et al., 1981; Lipa and Barrick, 1982; Wyatt, 1986; Bathgate et al., 2006; Shen et al., 2012, 2013; Wang et al., 2014, 2016; Forgot et al., 1981; Alattabi et al., 2019).

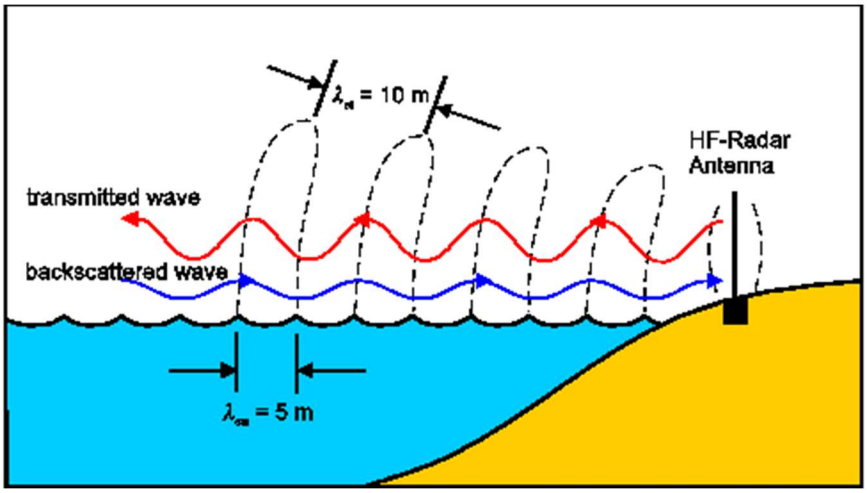

Figure 2.1: Schematic diagram showing the principle of operation HF radars assuming a transmitted HF wave with wavelength 10 m and backscattered wave by ocean waves with wavelength 5m (Gurgel et al., 1998).

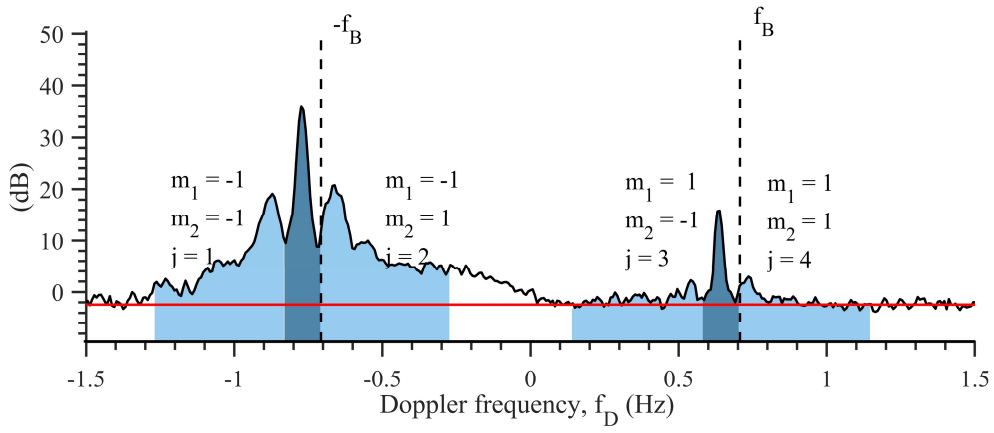

Figure 2.2: Doppler spectrum estimated from a 48 MHz Very High Frequency (VHF) radar. The dark and light blue regions denote the first (σ_1) and second (σ_2) order spectra respectively, the solid horizontal red line represents the noise level, and the vertical dashed lines denote the theoretical Bragg frequency.

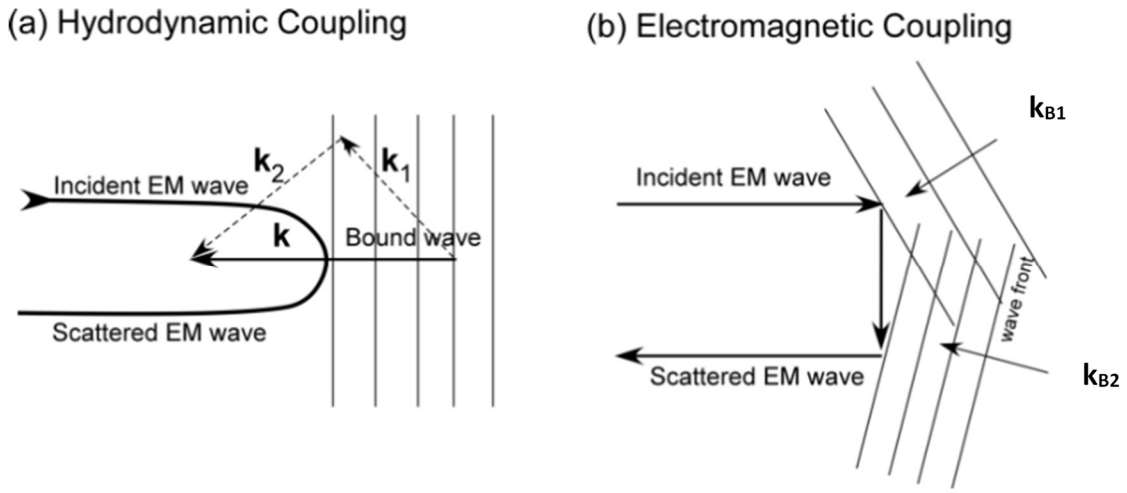

Figure 2.3: Schematic representation showing the mechanisms of second-order scattering caused by (a) nonlinear hydrodynamic effects and (b) electromagnetic (double scattering by a pair of ocean waves), (from Kumar, unpublished).

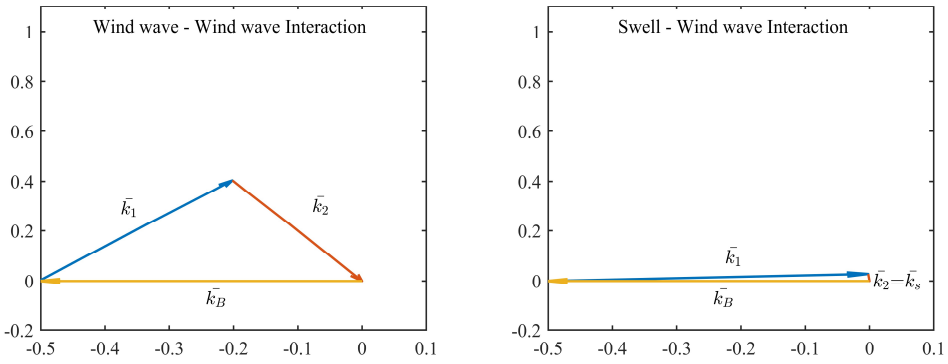

Figure 2.4 Schematic showing the first-order interaction of two waves (nonlinear hydrodynamic effect) that satisfy the criterion $\overrightarrow{k_1} + \overrightarrow{k_2} = \overrightarrow{k_B}$. The left panel shows the wave-wave nonlinear interaction for two wind waves, and the right panel shows the interaction of a swell ($k_2 = k_s$) and a wind wave with $k_s << k_1$.

CHAPTER 3

SWELL AND WIND WAVE INVERSION USING A SINGLE VERY HIGH FREQUENCY (VHF) RADAR[1]

[1] This chapter has been published as Alattabi, Z.R., Cahl, D. and Voulgaris, G., 2019. Swell and Wind Wave Inversion Using a Single Very High Frequency (VHF) Radar. *Journal of Atmospheric and Oceanic Technology*, *36*(6), 987-1013. Copyright permission has been obtained for reprint. See Appendix A for more details.

Abstract

A hybrid, empirical radar wave inversion technique that treats swell and wind waves separately is presented and evaluated using a single 48-MHz radar unit and in situ wave measurements. This hybrid approach greatly reduces errors in radar wave inversion during swell seas. Our analysis suggests that, prior to the inversion, the second-order spectrum should be normalized using Barrick's weighting function because this process removes harmonic and corner reflection peaks from the inversion and improves the results. In addition, the resulting calibration constants for the wind wave component are not wave-frequency dependent and are similar in magnitude to those found in previous studies using different operating-frequency radars. This result suggests radar frequency independence, although additional experimental verification is required. The swell component of the model presented here ignores the effect of swell's propagation direction on the radar signal. Although this has several limitations and may only be useful near the coast (where swell propagates close to perpendicular to the coastline), the resulting wave inversion is accurate even when swell is propagating close to perpendicular to the radar beam direction. RMS differences relative to in situ wave height measurements range from 0.16 to 0.25 m as the radar beam angle increases from 22^{o} to 56^{o}.

3.1 Introduction

Sea state information is usually collected using in situ sensors that record local wave conditions. Determination of spatial variability requires the deployment of several sensors making it a difficult and costly activity. Satellite technologies (i.e., Jackson, 1981; Guymer, 1990) have been used for wave height estimations over large scales, their application is challenging because of temporal resolution (based on satellite orbit and repetition coverage rate). Although recent advances in satellite technology and signal analysis (i.e., Collard et al., 2005) have made applications in the coastal ocean feasible, their application is still constrained by their spatial resolution (~2.5 km) that makes them comparable to those of low-frequency radars. This part of the coastal ocean, extending from the coastline to a range of tens to hundreds of kilometers offshore, is the area that mid- to high-frequency (HF) radars can provide both surface current and wave data, at high spatial and temporal resolution allowing identification of spatial gradients. The HF radar-derived parameters can facilitate operational activities that can utilize the data as either stand-alone information or integrated with numerical models through data assimilation (e.g., Paduan and Shulman, 2004; Waters et al., 2013).

The HF radar signal backscattered from the ocean surface is used to calculate the radar's Doppler energy spectrum (Crombie, 1955; see Figure 3.1) at a number of locations over the radar coverage area. The two largest and narrowest (first-order) peaks in the Doppler spectrum are the result of backscatter by ocean waves with a wavelength half the radar's wavelength. The shift from the theoretical Bragg frequency, defined by the operating frequency of the HF radar, is used to estimate the ocean surface current along the direction of the radial beam (radial currents; e.g., Paduan and Rosenfeld, 1996).

The spectral continuum (second-order scattering), present on either side of each first-order Bragg peak, contains information on ocean waves at frequencies other than that of the Bragg frequency. These areas are the result of nonlinear interactions between the electromagnetic (EM) waves and ocean surface waves that satisfy the requirement that the sum of the wavenumber vectors equals that of the Bragg wave (i.e., Stewart, 1971; Hasselmann, 1971; Weber and Barrick, 1977).

Barrick (1971) and Barrick and Weber (1977) used nonlinear integral equations to develop the theoretical approach that describes the relationship between ocean waves and HF radar Doppler spectra. Subsequently, a number of theoretical inversion methods were developed for the inversion of the nonlinear integral equations and the extraction of ocean wave spectra from HF radar Doppler spectra. Barrick (1977b) presented the first inversion method; this was improved by Lipa (1977) who linearized Barrick's equations and used a theoretical wave spectrum and a stabilization technique to carry out the inversion. Gill (1990) and Howell and Walsh (1993) developed a method for the inverse analysis that uses singular value decomposition techniques to solve the linearized equations. This method was later extended by Zhang and Gill (2006) for bistatic radar systems. Wyatt (1990) applied the Chahine-Twomey relaxation method to invert the nonlinear integral equation of radar cross section. Although this solution is limited to wave frequencies of less than 0.2 Hz, it was argued that it is capable of providing a good estimation of the directional wave spectrum. A nonlinear optimization algorithm that does not require any linearization or approximation was presented by Hisaki (1996) to solve the nonlinear integral equations.

In addition to the complex and computationally intensive methods described above, other simpler, mostly empirical methods have been developed. Barrick (1977a) was the first to derive an approximation for calculating nondirectional wave spectra and bulk parameters as wave height and period. Barrick (1977b) tested his empirical method against wave buoy data and later on, Maresca and George (1980) and Heron et al. (1985) developed modified versions of Barrick's method. Heron and Heron (1998) compared these parameterized inversion methods against in situ data and concluded that Barrick's (1977b) original method performed the best.

Gurgel et al. (2006) extended the empirical algorithm to allow the estimation of wave directional characteristics using two phased-array HF radars that look on the same patch of the ocean from different directions. Although this method requires two radar systems, its accuracy depends on the performance of each individual unit and the accuracy of the coefficients (see section 3.2) used for the inversion of the signal from each unit. More recently, Lopez et al. (2016) evaluated the method of Gurgel et al. (2006) using data from a pair of 12-MHz phased-array HF radars deployed over a period of 5 months. Their calibration resulted in coefficients different than those suggested by Gurgel et al. (2006) even after accounting for the difference in operating frequency. The authors of that study suggested that discrepancies in the estimations could be due to antenna side-lobes, the presence of second-harmonic peaks in the Doppler spectrum, and the presence of swell waves. Although, Barrick (1977a) has suggested that weighting of the normalized second-order spectra by the appropriate coupling coefficient helps eliminating the harmonic peaks, this was not utilized in either Lopez et al. (2016) or Gurgel et al. (2006). Furthermore, the empirical method was applied across all wave

frequency bands, although Lipa and Barrick (1980) and Forget et al. (1981) had noted that the parameterized inversion technique does not apply to swell.

Most of the work reported in the literature is based on the use of common radar systems operating at high frequencies ranging from 4 to 30 MHz. These systems provide spatial resolutions ranging between 0.3 and 5 km, and their range varies from 20 – 200 km (Paduan and Washburn, 2013). On the other hand, very high frequency (VHF) systems (30-50 MHz) can achieve higher spatial resolutions of 150-300 m but with a lower range of 10- 15 km (Broche et al., 1987; Shay et al., 2002; Molcard et al., 2009; Shrira et al., 2001; Voulgaris et al., 2011). Although the accuracy of those systems in measuring surface currents is similar to that of lower-frequency systems (Voulgaris et al., 2011), their ability to measure waves has not been examined before.

In this study, we examine the applicability of the empirical inversion method for the estimation of ocean wave spectra and bulk wave parameters (i.e., root-mean-square (RMS) wave height, peak wave period, mean wave period, wind and wave direction) using a single VHF (48 MHz) system. Single site performance controls the accuracy of estimations, when two or more overlapping radars are used, and they can increase the coverage area for wave extraction, in areas of no station coverage overlap (Wyatt, 2002). Contrary to previous studies using empirical methods, in here, we attempt to increase the accuracy of the method by accounting for the presence of swell waves through the development of a hybrid technique. The new technique is applied on VHF radar Doppler spectra and the results are compared against ocean wave spectra obtained using in situ instrumentation deployed over a variety of ranges and beam angles in relation to the VHF radar unit. In the following, section 3.2 outlines the hybrid empirical inversion method

used for the extraction of wave spectra from the VHF radar signal. Subsequently, in section 3.3, the experimental setup and data collection are presented. The results of both the calibration and inversion using the model are presented in section 3.4. In section 3.5, the findings from the application of the model are discussed while the conclusions of this study are presented in section 3.6.

3.2 Wave Inversion Model

Locally generated wind waves exhibit large directional spreading and individual waves of different wavelengths and directions interact with each other and the radar signal, contributing to the backscattered radar signal (Barrick and Weber 1977; Lipa, 1978). The accuracy of radar wave inversion has found to be related to the magnitude between the radial beam direction and wave propagation direction (Barrick, 1977b). It has been shown that when wave direction is near perpendicular to the beam direction, the accuracy of wave estimates is reduced. On the other hand, swell waves have very narrow (singular) directional characteristics that violate the assumptions made regarding the contribution of waves in the Doppler spectrum. This has led to the development of specialized methods for inversion for swell waves (Lipa and Barrick, 1980; Lipa et al., 1981). The presence of swell was used to explain the discrepancies found between observations and estimates using the wind wave inversion method (Lopez et al., 2016). In their study, Lopez et al (2016) found different regression coefficients for different cross angles (the angle between wave direction and radar beam direction) and this can be attributed to the presence of sharply peaked (in both frequency and direction) swell waves. Recognizing these differences, we present a model that combines the methods presented by Heron and Heron (1998) and Lipa et al. (1981) into single hybrid empirical

model. Its application requires defining the frequency (f_c) that separates wind from swell waves. This could be achieved using the wave age criterion (Hanson and Phillips, 2001) but it requires information on wind speed and direction. In practical applications, if no wind information is available, the value of this frequency can be determined using historic records or wave climate analysis. Along the coast of the southeastern United States, 0.1 Hz can be used as the separation frequency while a lower value will be applicable for the west coast where swells are more prominent (Kumar et al., 2013).

3.2.1 Module for wind driven seas

Barrick's (1977b) model has been the basis for the development of most empirical methods to date for the extraction of wave characteristics from second-order Doppler spectra. It is based on a simple relationship between ocean wave height and the weighted second-order sidebands, normalized by the total first-order energy of the Doppler spectrum, denoted as R_W. Following Heron and Heron (1998), the bulk RMS wave height, defined as $H_{rms} = \sqrt{8m_0}$, (WMO, 1998) where m_0 is the 0th moment of sea surface variance, can be estimated as:

$$H_{rms} = \xi \left(\frac{4}{k_o}\right) \sqrt{R_w} \tag{3.1}$$

where k_o is the radar wavenumber, and ξ is an empirical constant. Note that in Barrick (1977b) and other HF radar studies (i.e., Heron and Heron, 1998; Ramos et al., 2009) RMS wave height was defined as simply the standard deviation of the sea surface variability. In this manuscript we have adopted the WMO (1998) definition, as to be consistent with common practices of wave measurements.

Following Heron and Heron (1998), the noise level for each individual Doppler spectrum is first identified, using the method described in Hildebrand and Sekhon (1974), and removed from the recorded spectrum. Then $R_W(f)$ is estimated from each side (i.e., negative and positive frequency ranges) of the Doppler spectrum. Most studies exclude the side with the lower signal-to-noise ratio (SNR); however, if SNR is similar, including both sides (i.e., averaging) can improve the wave inversion. Since H_{rms} is derived from the integral of the wave energy spectrum, Eq. (3.1) can be expanded to its equivalent spectral form so that the wind wave energy spectrum $S_w(f)$ is given by:

$$S_w(f) = \alpha(f)\frac{2\,R_W(f)}{{k_o}^2} \tag{3.2}$$

where $\alpha(f)$ is a calibration coefficient that depends on wave frequency (f), as in Gurgel et al. (2006). Contrary to Gurgel et al. (2006) and Lopez et al. (2016), R_W here is the "weighted" second-order continuum normalized by the integrated first-order spectra; it was defined by Barrick (1977a, b) as a function of the radar-derived Doppler frequency (f_D) as:

$$R_W(f_D) = \frac{\sigma_2(f_D)/W(f_D/f_B)}{\int_{f_B-\Delta f}^{f_B+\Delta f}\sigma_1(f_D)\,df_D} \tag{3.3}$$

where σ_1 and σ_2 are the first and second-order spectra, Δf is the small frequency band around the first-order Bragg peak (f_B) corresponding to the peak half-width, and W is the weighting function defined in Barrick (1977b, see Figure 3 therein) for deep water conditions. Ocean wave (f) and radar Doppler (f_D) frequencies are related through the radar Bragg frequency (f_B); the latter corresponds to zero ocean wave frequency, so that $f = |f_D - f_B|$.

3.2.2 Module for Swell

Swell consists of gravity waves propagating outside their area of generation and are not in equilibrium with the local wind conditions (Hanson and Phillips, 2001); they are sharply peaked in both frequency and direction, and as shown in Maresca and Georges (1980), Lipa and Barrick (1980), and Bathgate et al. (2006) require a separate radar inversion method. In these narrow beam radar models, swell waves appear as peaks in the second-order sidebands of the radar Doppler spectrum and they are located close to the first-order peak. Their amplitude is proportional to $\cos^2 \theta_s$, where θ_s is the angle between the radar beam and the swell propagation direction (for details, see Lipa and Barrick, 1980 and Bathgate et al., 2006). When swell waves cross the radar beam within $\pm 30^o$ from perpendicular large inaccuracies in the swell inversion are reported (Bathgate et al., 2006; Wang et al., 2016). However, in nearshore applications refraction due to the shallow water depths causes swell waves to approach the coastline at very small angles, almost perpendicular to the coastline (but not necessarily perpendicular to the radar beam direction). The roughly constant propagation direction of swell waves near the coastline allows us to assume limited directional effects in the nearshore and propose a simpler model.

Equation (3.3) with $W(f_D/f_B) = 1$ is used to estimate the radar swell cross section ratio in the swell band; its peak value (R_s) is used to estimate the RMS wave height of swell (H_s) as:

$$H_s^2 = \alpha_s \frac{2\,R_s}{k_0^2} \tag{3.4}$$

where α_s is an empirical factor that accounts for directional characteristics and other system dependent variabilities similarly to the empirical factor in Eq. (3.2) for wind waves. In addition, this factor includes the effect of the coupling coefficient, which for swell is different than it is for wind waves (Lipa et al., 1981). The RMS swell wave height (H_s) can be converted to an energy spectrum using a Gaussian function that distributes the swell energy over the swell frequency band with the peak energy centered at the swell peak frequency (f_s):

$$S_s(f) = \left(H_s^2/8\sqrt{2\pi\sigma^2}\right) e^{-\frac{(f-f_s)^2}{2\sigma^2}} \tag{3.5}$$

where σ represents the width of the spectra which can be determined from existing in situ wave spectra from the study area or using validated model hindcasting results (e.g., Kumar et al., 2017).

Following Lipa et al. (1981), the swell peak frequency (f_s) is determined from the four swell peaks in the Doppler spectrum (defined from lowest to highest in Doppler frequency as f_1^-, f_2^-, f_3^+, and f_4^+ with the superscripts defining the sign of the side of the Doppler spectrum). There are used to estimate swell frequency as $f_s = (\Delta f^+ + \Delta f^-)/4$, or $f_s = \Delta f^{+or-}/2$, depending on whether one or both sides of the Doppler spectrum is used, where $\Delta f^- = f_1^- - f_2^-$ and $\Delta f^+ = f_4^+ - f_3^+$.

The swell and the wind wave spectra can be combined to a single wave energy density spectrum $\left(S(f) = S_w(f) + S_s(f)\right)$.

3.2.3 Wind and Wave Direction

Given the high frequency of the ocean Bragg waves, it is assumed that they are aligned with the local, wave-generating wind. Thus, wind direction can be estimated using (Long and Trizna, 1973; Fernandez et al., 1997):

$$\zeta = \frac{\sigma_1(f_D^+)}{\sigma_1(f_D^-)} \tag{3.6}$$

where $(\sigma_1(f_D^+))$ and $\left(\sigma_1(f_D^-)\right)$ represent the first-order Bragg peak energies (i.e., the integral of the first-order region of the spectra) corresponding to approaching and receding ocean Bragg waves, respectively. A directional distribution function $G(\theta)$ of the Bragg ocean waves is used to relate the ratio ζ to the direction of ocean waves (Longuet-Higgins, 1963):

$$G(\theta) = A\cos^s\left(\frac{\theta}{2}\right) \tag{3.7}$$

where *s* is the spreading factor, A is a constant that satisfies $\int_{-\pi}^{+\pi} G(\theta)d\theta = 1$, and $\theta = \theta_r - \theta_w$, with θ_w representing Bragg wave (wind) direction and θ_r representing the radar beam direction. Substituting Eq. (3.6) in Eq. (3.7) and after some manipulation, the Bragg wave (wind) direction is estimated as:

$$\theta_w = \theta_r \pm 2\,arctan\left(\zeta^{\frac{1}{s}}\right) \tag{3.8}$$

The sign plus/minus refers to directional ambiguity for a single radar system. Parameters *s* = 2 is commonly used as it allows simplicity in the calculation when two systems are used (Gurgel et al., 2006; Fernandez et al., 1997). The ambiguity issue can be resolved using two or more radar systems that look at the same ocean area from different

angles, or when the directional characteristics of the Bragg wave/wind are well constrained by the environmental setting (i.e., coastline morphology) or through other means.

Gurgel et al. (2006) expanded the method described above for the calculation of Bragg wave/wind direction to the second-order Doppler sideband energies. They utilized the ocean wave frequency (*f*) dependent ratio of the second-order side band corresponding to receding waves ($\sigma_2^-(f)$) over the side corresponding to approaching waves ($\sigma_2^+(f)$) to define the direction of ocean waves with frequency f as:

$$\theta(f)_{inv} = \theta_r \pm 2\, arctan\left(\left(\frac{\sigma_2^+(f)}{\sigma_2^-(f)}\right)^{\frac{1}{s}}\right) \tag{3.9}$$

where θ_r is radial beam direction, and s is the wave directional spreading factor as in Eq. (3.8). As for the case of wind direction, the ambiguity in the solution of Eq. (3.9) can be resolved using multiple radar stations or utilizing additional information.

3.3 In situ and VHF Radar Data Availability and Analysis

The data used in this study were collected as part of an experiment carried out in the vicinity of Diamond Shoals, a sand shoal complex that extends up to 40 km offshore from Cape Hatteras Point, North Carolina. The experiment was carried out under the auspices of the Carolinas Coastal Change project, led by the U.S. Geological Survey, and details can be found in Armstrong et al. (2013). A number of in situ acoustic current profilers were deployed in the surf-zone and inner shelf regions of the study area (Figure 3.2). In addition, a single VHF radar station with a coverage area that included the in situ data collection sites was operated during the experimental period.

3.3.1 In Situ Data

Wave and current data were collected at 13 locations dispersed throughout the study area (see Kumar et al., 2013 and List et al., 2011). Only seven of these sites (O2, N1, N2, N3, N4, N5, and N6) were within the footprint of the radar coverage area (see Table 3.1 and Figure 3.2). Site O2 was located at a water depth of 10.7 m and provided hourly measurements. Four of the sites (N1, N2, N3, and N4) were located to the east of the cape and its associated shoal, while the remaining two (N5 and N6) were deployed over the shoal itself. The instrumentation consisted of Nortek AS Aquadopp (AQD) and Teledyne RD Instruments acoustic Doppler current profilers (ADCP) measuring three-dimensional flow velocities (bin size 40 cm) and pressure fluctuations with a sampling frequency of 1 Hz. The AQD sensors (sites N1, N2, N3, and N6) were set up to collect data continuously while the ADCPs (sites O2, N4, and N5) were collecting data in burst mode (1024 data points, every hour, centered on the hour). The continuous AQD records were divided into 1024-s-long segments, centered on the hour, to match the ADCP and VHF data collection. The types of instrumentation deployed at each site, their period of data collection and depths are listed in Table 3.1. Pressure (p) and horizontal (u, v) velocity records corresponding to the bin closer to the bed (0.40 meters above bed (mab) for the ADP sites, 0.64 mab for the O2 and N5 ADCPs, and 1.60 mab for N4 ADCP) were used to calculate power spectral and cross-spectral densities using Welch's (1967) method (15 ensembles of 128 data points each, with 50% overlap). The sea surface power spectral density was estimated from the pressure spectra after correcting for pressure attenuation with depth (Bishop and Donelan 1987). To reduce amplification of noise, the analysis was performed to a maximum frequency of 0.25 Hz (except for site O2, where

the maximum frequency was set to 0.195 Hz because of the larger water depth). The surface spectra and corresponding cross-spectral densities were used to calculate wave height, period, direction, and directional spreading using the moments method (Herbers et al., 1999). Partitioning of the wave field (energy and direction) into swell and wind waves was carried out by integrating the wave spectra over the frequency bands below and above 0.1 Hz, respectively.

Meteorological data and offshore wave conditions for the deployment period were obtained from the NOAA/National Data Buoy Center (NDBC) Diamond shoals buoy (41025, Figure 3.2) which is located some 29 km from the VHF radar station and at a mean water depth of 48 m.

3.3.2 VHF Radar Data

A single, 12-antenna, phased-array, VHF Wellen Radar (WERA) system (Gurgel et al., 1999), manufactured by Helzel Messtechnick, GmbH, was deployed at the study site (Figure 3.2). Its operational frequency was 48 MHz, and the use of 1 MHz bandwidth during transmission resulted in 150 m range resolution. Radar data were obtained 2 times per hour for the period 3-26 February 2010 with continuous radio transmission for a period of 14.8 min centered on 0 and 30 min past the hour. A total of 967 transmissions were made over the 22-day data collection period, with limited interruptions due to mains power issues (95% data recovery rate). For this analysis Doppler spectra were estimated by steering the beam of the VHF Radar system at the instrument locations at the appropriate range cell. The Doppler spectra have a frequency resolution of 0.009 Hz and cover the range from -2.29 Hz to 2.29 Hz (the Nyquist frequency of a 4.48 Hz chirp rate). The energy is expressed in decibels defined using an

arbitrary reference level, as recorded internally by the WERA system. Radial surface velocity estimates from the Doppler spectra were compared with the point measurements obtained using the in situ instrumentation and they found to agree with an error ranging between 4 and 12 cm s^{-1} (Voulgaris et al., 2011), although these findings are not presented here.

For this analysis, only Doppler spectra that coincide with the times of wave data collection using the in situ sensors (hourly for O2, N4, and N5, and half-hourly for N1, N2, N3, and N6) are used. The range to the in situ sensor locations from the radar receive (Rx) antenna array, as well as the angle between the beam-forming direction and the radar boresight, are listed in Table 3.1. Site N1 was the closest to the radar (0.7 km), and the largest range (4.2 km) corresponds to sites N5 and N6. The site with a radial beam direction closest to the radar boresight was O2 (22.3°), and site N6 was the one with the largest beam angle (53.6°).

We use sites N4 and O2 (Figure 3.2) to calibrate the model presented in section 3.2 and to estimate the empirical coefficients for the wind wave and swell components of the model. The second-order sidebands are limited to a low frequency of 0.058 Hz (lower frequencies are often contaminated by first-order noise) and an upper limit of 0.5 Hz (values above this were often close to the noise of the HF radar signal), which covers wave periods from 2 to 17 s.

The inversion is carried out using only the dominant side of the Doppler spectrum unless the two Bragg peaks differ by less than 3 dB. In the latter case an average of both

sides is used. The swell peak frequencies (f_1^-, f_2^-, f_3^+ and f_4^+) are estimated using the weighted mean method of Young (1995) with n =5 (Young and Verhagen, 1996):

$$f_m = \frac{\sum \sigma_{2m}(f_i)^n f_i}{\sum \sigma_{2m}(f_i)^n} \quad where \;\; f_i < f_c, \tag{3.10}$$

here $m = 1, \ldots, 4$ denotes the four sidebands from lowest to higher frequency and *i* is the index of the discrete frequency at which a Doppler estimate is available.

3.4 Results

3.4.1 Wind and Wave conditions

Time series of wind conditions recorded offshore, at the NDBC buoy location, and wave conditions recorded both offshore at the buoy location and in the nearshore, within the HF radar coverage domain are shown in Figure 3.3. A number of wind events are identified, with the largest one commencing on 6 and February lasting until 10 February. During this event, only sites O2, N5, and N6 were operational (see Table 3.1) and waves reached offshore wave height of approximately 4 m (see Figure 3.3b, day 6). In the nearshore, during the initial period (days 6 – 6.4), wave energy in the wind wave band was dominant; after day 6.4, swell waves became dominant. Times representing these two conditions are marked on Figure 3.3 as A (day 6.21) and B (day 7.96), respectively. On 10 February, a second frontal system moved in the area that produced elevated sea state (up to 3 m RMS wave height on 11 February) for a period of a few days. During this event, all sites, except for N2, were operational (see Table 3.1). In Figure 3.3, D denotes the time when high wind waves are present offshore (day 11.54), while E identifies the time when swell waves were recorded both offshore and in the

nearshore (day 12.54). We highlight a few more wind events on days 10.08, 13.66, 16.54, and 23.1 when H_{rms} values varied between 0.5 and 1 m (see C, F, G and H in Figure 3.3). These represent wave conditions with different directions and peak frequencies (see Table 3.2). Although no directional wave information exists offshore, the wind data from the NDBC buoy indicate an alongshore wind-generated wave propagation predominantly from North. In the nearshore, mean wave directions, for both wind and swell waves, are within 20 degrees from perpendicular to the coastline (see Figure 3.3g).

3.4.2 In Situ Wave Spectra

The full wave spectra $S(f)$, from sites O2 and N4, used to estimate the wave parameters are shown in Figure 3.4. The same spectra were used to estimate the coefficients for the wave inversion model presented in section 3.2 [see Eqs. (3.2) and (3.5)]. Spectra covering the whole VHF radar deployment period are available for site O2 (see Figure 3.4), while N4 was deployed on 9 February and after the occurrence of the first significant wind event. The individual events/conditions (A-H) identified in Figure 3.3 are also shown in Figure 3.4.

3.4.3 VHF Radar Doppler Spectra

The radar-derived Doppler spectra for sites N4 and O2, for the full deployment period, are shown in Figure 3.5 in the form of a time-stack. The highest values at each time step present in the positive and negative Doppler frequency ranges correspond to the first-order peaks, while the energy around these local maxima represents the second-order continuum. This is best shown in the individual Doppler spectra plots from the identified events (see Figure 3.6, left panels). The deviation of the first-order peak from the Bragg

frequency (±0.701 Hz) is time varying as it depends on surface current speed which is modulated by the prevailing wind and tidal conditions (see Figure 3.3). Doppler spectra from events A and B (see Figures 3.5 and 3.6, left panel) are typical examples of highly energetic conditions. They demonstrate the merging of first and second-order parts of the spectrum that makes defining the first-order peak difficult.

For each of the Doppler spectra a Gaussian curve was fitted on the Bragg peaks identified using two frequency bins around each peak. The fitted first-order peak was then subtracted from the Doppler spectrum to reduce its potential influence on the second-order sidebands. As in Heron and Herron (1998), the second-order sidebands surrounding the Bragg peaks were first weighted, using Barrick's (1977b) weighting function; then, they were folded around the Bragg peak frequency and added together for each side separately. Last, they were normalized by the integral of first-order peak energy for each corresponding side according to Eq. (3.3). The Bragg peak half-width (Δf) in Eq. (3.3) was determined by the half-width of the Gaussian fit to the Bragg peak. The weighted and normalized second-order spectra from each side were averaged to generate the final $R_W(f)$ spectra for sites O2 and N4. These are shown in Figure 3.7 as time stacks, while individual $R_W(f)$ for the specific events A-H are shown in Figure 3.6 (center panels).

3.4.4 Wave Inversion Model Calibration

Prior to estimating the frequency dependent coefficient for wind seas (Eq. (3.2)) and swell (Eq. (3.4)), the spectral energy data for each frequency band were quality assured using several criteria. First, an analysis was carried out to ensure that both in situ

and radar Doppler spectral estimates were above their corresponding spectral noise floor. For the in situ wave spectra the value of 0.15 m^2 Hz^{-1} was assumed to be the noise floor, as determined from the spectra. For the selection of the normalized Doppler spectral data ($R_W(f)$), we followed the approach of Wyatt et al. (2005) and Lopez et al. (2016) and only Doppler spectra with energy (SNR) greater than 25 and 10 dB for the first- and second-order energy peaks, respectively, were selected. The Bragg peak was required to be at least 5 dB above the second-order sidebands, so that it can be clearly identified.

The calibration coefficients corresponding to Eq. (3.2) estimated using the data that passed these criteria are denoted as $\alpha(f)_{SNR}$. In addition, a subgroup of the data was created that included only records of wind seas ($f_p > 0.10$ Hz), without swell being present. The coefficients derived using these data are denoted as $\alpha(f)^{+}_{SNR}$.

Because our data are from the nearshore region, we explored the effect that the shallow water depth might have in the calibration by creating three different estimates of $R_W(f)$: (i) using the deep-water weighting function of Barrick (1977b); (ii) not applying any weighting at all as in Lopez et al. (2016); and (iii) using a shallow water weighting function as suggested in Lipa et al. (2008). The shallow water weighting function was calculated using the forward model of Gill and Walsh (2001). The estimated $R_W(f)$ values for each case correspond to discreet ocean wave frequency bands that span the range 0.058-0.500 Hz. These were interpolated to match the frequency bands corresponding to the in situ wave spectra $S(f)$ estimates, which were limited to 0.19 and 0.25 Hz, for O2 and N4, respectively. The corresponding calibration coefficients $\alpha(f)$ were estimated for each wave frequency (f), as in Lopez et al. (2016), using a least

square fit between all $S(f_i)$ and the corresponding $R_W(f_i)$ values, from all qualified Doppler spectra and for each frequency band *i*. Although Eq. (3.2) is to be used for the wind waves only, the fitting was carried out for all frequencies, including swell, as in Lopez et al. (2016), and the results are shown in Figure 3.8.

The coefficients estimated using the deep-water weighting function (see Figure 3.8a, c) for each site are similar to each other, independent of the data used ($\alpha(f)_{SNR}$ or $\alpha(f)^{+}_{SNR}$). In the wind wave frequency range (0.10 to 0.25 Hz) the coefficients are of similar magnitude across the whole wind wave frequency range, for both cases. However, at lower (swell) frequencies (<0.10 Hz), $\alpha(f)_{SNR}$ values are 3 – 4 times larger than the $\alpha(f)^{+}_{SNR}$ ones (see Figures 3.8a, c). This discrepancy at the swell band is mainly because the SNR^{+} data do not include conditions with significant swell energy. The correlation coefficient (*r*) of $R_W(f)$ and $S(f)$ values used to estimate $\alpha(f)_{SNR}$ range from 0.2 to 0.9 at frequency range 0.058 – 0.10 Hz and these values are reduced to 0.4 – 0.6 at higher frequencies (f>0.10 Hz) (see Figure 3.8b). These correlations are similar to those reported by Lopez et al. (2016). Relative to $\alpha(f)_{SNR}$, the correlations for $\alpha(f)^{+}_{SNR}$ exhibited greater variability (0.2 – 0.8) and overall lower values for frequencies < 0.1 Hz (swell band), and somewhat more consistent values (0.4 – 0.6) for frequencies > 0.1 Hz.

The $\alpha(f)^{+}_{SNR}$ vales determined without applying the weighting function for R_W are shown in Figure 3.8e. The values shown are 2.7 times smaller than those estimated using the deep-water weighting function and exhibit an identical distribution over the frequency range. This is mainly because the weighting function for our radar frequency is almost flat over the wave frequency range used in this study (for more details see section

3.5.1). Use of the shallow water weighting function (Figure 3.8g) makes the regression coefficients more frequency dependent with their values increasing toward lower wave frequencies. This also introduces a variability between sites which is due to the different water depths.

For the swell wave module, the spreading parameter (σ) (see Eq. (3.5)) was estimated by fitting a Gaussian curve to the swell peaks found in the in situ wave spectra. Histograms of the distribution of the estimated σ values, for each site, are shown in Figure 3.9a and 3.9b. A skewed distribution is revealed, with 0.010 and 0.009 Hz^2 being the peak values for sites O2 and N4, and their mean value ($\sigma = 0.0095\ \mathrm{Hz}^2$) was used. The swell calibration coefficient α_s was estimated using a least square regression fit to Eq. (3.4); values of 0.05±0.013 and 0.07±0.009 were derived for O2 and N4, respectively (see Figure 3.9c, d).

3.4.5 Application of the Wave Inversion Model

3.4.5.1 Calibration sites: O2 and N4

In this section, the coefficients estimated during calibration (see section above) using the deep-water weighting function are used to invert the radar derived Doppler spectra from sites O2 and N4 into surface wave spectra.

Prior to the inversion, the ratio of swell over wind wave energy in the normalized second-order Doppler spectrum, defined as:

$$L = \frac{\sum_i R_W(f_i < f_c)}{\sum_i R_W(f_i \geq f_c)} \tag{3.11}$$

is used to identify Doppler spectra with significant energy in the swell band. If $L > 1$, the swell module (Eq. (3.5)) is used to estimate the wave energy at frequencies $f < f_c$ using the site-specific α_s value (0.05 and 0.07 for O2 and N4, respectively). The wind wave spectrum (Eq. (3.2)) is calculated for $f \geq f_c$, if $L > 1$, and for all frequencies (including swell) if $L \leq 1$. Because of the relatively small variability of $\alpha(f)^{+}_{SNR}$, using the deep-water weighting function along the wind wave frequency range (see Figure 3.8c), and the similarity of the frequency-averaged values between sites (0.26 ± 0.01 and 0.25 ± 0.02 for O2 and N4, respectively), the frequency- and site-averaged value of 0.255 is used. The inversion is carried out to frequencies up to 0.5 Hz which is higher than the maximum frequency of the energy spectra estimated using the acoustic instruments (0.19 and 0.25 Hz, for O2 and N4, respectively); the inverted wave spectra corresponding to the individual events A to H are shown in Figure 3.10. Note that the same analysis for the wind waves was carried out using the no-weighted normalized spectra, and the results were almost identical and not shown here. Similar results (not shown here) were obtained using the shallow water weighting function; however, this required the use of coefficients that are different for each frequency but also vary between sites.

Events A and B (in situ RMS wave heights of 2.3 and 2.5 m, respectively) are examples of spectra with Bragg peaks that are less than 5 dB above the second-order sidebands. Although these spectra are within Barrick's (1977a, b) wave height limits ($0.42 < H_{rms} < 2.82$ m, for a 48 MHz system), they do not meet the signal quality criteria. They are shown here as a demonstration of the effectiveness of this criterion to identify Doppler spectra not suitable for wave inversion. The wave inversion fails to identify the peak of the wave spectrum and the in situ wind sea spectra match the inverted

one only at high frequencies. During event E, although the total wave height is 1.75 m, the partitioned wind wave height is 1 m and the spectrum is reconstructed accurately. Similar agreements between the inverted and in situ spectra can be seen in events C and D which are characterized by wind sea spectra only (no swell) but with a smaller wave height (1 m). For the remaining events (F, G, and H), the reconstructed spectra bear a resemblance to the ones estimated from the in situ data (see corresponding panels in Figure 3.10).

In Figure 3.11, bulk wave parameter estimates (i.e., RMS wave height, mean, and peak wave frequency) from the inverted wave spectra are compared against estimates from the in situ spectra. Wave height RMS errors are 0.21 and 0.17 m for sites O2 and N4, respectively. The linear correlation coefficients are high (0.92 and 0.93, respectively) while the linear regression slope is 0.86 and 0.89, respectively (see Table 3.3). Note that the in situ wave spectra are also estimates and do not constitute absolute measurements of the true sea state; as such the error estimates presented above represent an assessment of the agreement between the two methods. However, independent evaluation of ADCPs for wave measurements with wave buoys (e.g., Work, 2008) have revealed RMSEs of 0.08 m, 2.6 s, and 0.7 s for wave height, peak and mean wave period, respectively, and 11^{o} for mean wave direction. These values provide a basis for the evaluation of the agreement found between the wave parameter estimates from the inversion method and in situ instrumentation.

3.4.5.2 Verification Sites

The inversion method is verified using Doppler spectra from sites N1, N2, N3, N5, and N6, that were not used in the calibration process, utilizing the coefficients

derived from sites O2 and N4. For the wind wave module, the frequency and site averaged value for $\alpha(f)^{+}_{SNR}$, as estimated using the deep-water weighting function, is used ($= 0.255$), and for the swell module the mean of the corresponding values for the two calibration sites ($= 0.06$) is adopted. For brevity, only the results for sites N1 and N5 are presented in detail (see Figure 3.12). The results of the statistical analysis for all sites are listed in Tables 3.3 and 3.4. As shown earlier, the Bragg peaks at events A and B are poorly defined, as they are less than 5 dB above the second-order sidebands (Figure 3.6). The peak of the wave spectrum is significantly underestimated in A and entirely missed in B, but the inverted spectra (see Figure 3.12) agree relatively well with the in situ ones at higher (wind wave) frequencies. Agreement in the wind wave band is found also for event C, although in this case the inverted spectrum contains more energy in the swell band than what is present in situ; at the same time the inverted spectra underestimate the peak wave energy. Events E and F show the best agreement between inverted and in situ data with event E being the best overall, even though the total wave height is 1.5 m, higher than those for other events (C, D, F, G, and H). For event D, there is good agreement between the two spectra for site N1, but for site N5 the inverted spectrum overestimates the energy present in higher frequencies.

The inverted and in situ estimated bulk wave parameters (RMS wave height, mean, and peak wave frequency) are compared in Figure 3.13 while the corresponding RMS errors and correlation coefficients of both total and partitioned wave heights and mean and peak periods are listed in Tables 3.3 and 3.4. Overall, they are of similar value as those estimated for the sites used in the calibration but the wave height errors are higher for swell than that for wind waves. The latter errors are smaller than the ones for

the total wave height. Data from periods of common data availability are used to estimate the wave height differences (in terms of RMS error) between stations for both the in situ and the inverted wave height estimates (see Table 3.5). The spatial differences between in situ wave heights range from 0.03 m (sites N6 - N2) to 0.19 m (sites N2-O2). The corresponding differences between inverted values range from 0.1 m (sites N4 – N3) to 0.39 m (sites N6 – N3). Overall differences of in situ measurements between different sites are slightly greater (25%-30%) when using the inverted wave heights. The exception is station N6 where the inverted heights from this site show a much higher error when compared with those from the other sites.

3.4.6 Directional Characteristics

The ambiguity in the wind and wave direction results (due to the use of a single station) was resolved using the in situ wind and wave measurements from the NOAA buoy and the in situ sites, respectively. Although this is not possible when no in situ data are available, we use this approach to evaluate the accuracy of a single VHF radar system in obtaining these angles. A complex correlation analysis (see Kundu, 1976) was carried out to examine the agreement between the in situ and inverted directional estimates. Prior to analysis the directional data were converted into vectors with magnitude equal to the wave height and direction the corresponding wave (or wind) direction. This allows the suppression of erroneous errors in direction occurring during periods of low wave energy.

A comparison of the wind direction results derived from the first-order peaks, from all sites, against the wind direction observations from the offshore NOAA buoy 41025 is shown in Figure 3.14 (left panels). The wind direction estimates are in general agreement with the measurements despite the fact that winds offshore might not be

identical to those in the nearshore (e.g., Wu et al. 2017). The complex correlation coefficients were found to vary between 0.68 and 0.75 with their corresponding angle varying from 9º to 16º (see Table 3.6).

In a similar manner, the wave direction for each frequency component (up to 0.5 Hz) for events A-H are estimated using Eq. (3.9) and are shown in Figure 15. Overall, the in situ and radar-derived wave directions for both calibration (O2 and N4) and verification (N1 and N5) locations show good agreement. The corresponding estimates for mean and peak wave directions are compared against the in situ estimates in Figure 3.14 (panels in middle and left column, for mean and peak energy wave direction, respectively) while the results of the complex correlation analysis for all sites available are listed in Table 3.6. For mean wave direction, the magnitude of the complex correlation coefficients ranges from 0.65 to 0.80 while their angles range from -33º to 9º. The smallest and larger magnitude of the correlation correspond to sites O2 and N4, respectively. The comparison of peak wave direction shows lower magnitude in complex correlation ranges 0.48-0.70 with angle in correlations -34º to 10º.

3.5 Discussion

3.5.1 The wave inversion model

The calibration of the hybrid empirical wave inversion model presented in section 3.2 produced calibration coefficients that were very similar between the two calibration sites (O2 and N4), despite their difference in range (3.3 and 2.0 km. respectively) and beam angle (22.3° and 38.2°, respectively). This was particular the case for the wind wave module (f > 0.10 Hz) when we excluded spectra with significant energy in the swell

band (see Figure 3.8c). These findings were similar to those obtained with or without (not shown here) applying the deep-water weighting function. Also, our coefficients show little variability with frequency which contrasts the findings of Lopez et al. (2016), who noted a greater variability of the coefficients with frequency even within the wind frequency range. In their case, as in Gurgel et al. (2006), the second-order spectra were not weighted using Barrick's weighting function, prior to normalization by the integral of the first order (σ_1).

Despite the satisfactory performance of the inversion method when not weighting the second-order spectrum, application of the weighting function allows compensation for the second harmonic and corner reflector peaks ($\sqrt{2}f_B$ and $2^{3/4}f_B$, respectively) which can be found only in the outer Doppler sidebands, as shown in Figure 3.16. This asymmetry cannot be captured by the calibration coefficients alone as these are applied on the two-side averaged normalized second-order Doppler spectrum. This is demonstrated in Figure 3.17, where a few examples of normalized second-order spectra are shown with and without applying the weighting function. The harmonic peaks at $\sqrt{2}f_B$ are clearly visible in the wave spectra with no weighting; these peaks are suppressed when weighting is applied. Wave spectra from the offshore buoy, located some 29 km offshore, do not show any wave energy being present in these frequencies confirming that these peaks are harmonics. Our in situ data do not extend to those frequencies, so these effects do not affect the inversion method. Lopez et al. (2016) reported that the harmonics and corner reflection peaks might be influencing the accuracy of their inversion and this was used to explain some of the discrepancies they encountered. Failing to apply the weighting function to suppress these peaks may result

in minima in the calibrations coefficients, as Lopez noted occurred in their calibration at $\sqrt{2}f_B$. Note that these peaks correspond to different ocean wave frequencies depending on the radar frequency (see Figure 3.17). Furthermore, application of the weighting function may be used to eliminate the dependency of the calibration factor to HF radar operational frequency and wind wave frequency; this has the implication that potentially a single, empirical coefficient may be applicable to all radar and wind wave frequencies, something that we are currently investigating.

The use of Barrick's (1977b) deep-water weighting function in our calibration leads to deriving a coefficient value which is consistent with those from other theoretical studies for deep water conditions. Although the shallow waters of our experimental site suggest that a shallow water coupling coefficient should be used, its use here did not produce any improvements in the inversion. Its effect was to modify the values of the calibration coefficient making it as frequency dependent parameter (see Figure 3.8g). Furthermore, a close examination of the VHF derived Doppler spectra from three stations, corresponding to three different water depths (see Figure 3.18), does not reveal any significant shallow water effects on the evolution of the Doppler spectra, as no frequency shift of the swell peaks due to depth variation between sites is observed. This is in agreement with Lipa et al (2008) who noted that shallow water effects are more relevant to lower frequency HF radars, at extremely shallow waters. However, in most cases lower frequency HF radars operate at coarser range resolutions and as such rarely produce data in the inner shelf region, except in very gently sloped continental shelves.

As we showed earlier (see Figures 3.8c, e) the calibration coefficients estimated with and without using the weighting function do not vary significantly, except for a

scaling factor of ~2.7. This is because for our operating frequency (48 MHz), the harmonic and corner reflection peaks appear at ocean wave frequencies 0.29 and 0.48 Hz, respectively (see Figure 3.16), which are beyond the frequency range of our calibration (0 – 0.25 Hz). For lower radar frequencies, the peaks appear within the wave frequencies of interest (see Figure 3.16) making the use of the weighting function a necessity. This argument is also supported by the disagreement between the Lopez et al. (2016) calibration coefficients with those suggested by Gurgel et al. (2006) even after applying the suggested scaling for radar frequency. It is notable that our frequency averaged calibration coefficient values are very similar to those reported by other studies that used different radar frequencies but implemented the weighting function. Heron and Heron (1998) and Ramos et al. (2009) using Eq. (3.1) found calibration constant $\zeta = 0.55$ and 0.58, respectively. Since $\alpha = \zeta^2$ (see Eq. (3.1) and Eq. (3.2)) our wind sea calibration constant ($\alpha = 0.255$) is equivalent to $\zeta = 0.504$, which closely agrees with these previous studies, suggesting a constant value across different HF radar systems and frequencies.

When swells are present, the calibration coefficients (Figure 3.8a) of the wind module in the lower-frequency bands ($f < 0.10$ Hz) resemble those of Gurgel et al. (2006) and Lopez et al. (2016). At these frequencies the variability does not depend on the use of the weighting function as it is almost flat over this frequency range (see Figure 3.16) for both sides around the Bragg peak. In Lopez et al. (2016), calibrations against different sites revealed a tendency for larger values when swell crosses the radar beam at angles close to perpendicular and smaller values when swell is aligned with the radar beam direction. Because of swell's singular directional characteristics, the wind wave

model underestimates the swell spectral energy when swell crosses the radar beam perpendicularly and overestimates it when swell propagates parallel to the radar beam. In the conditions encountered in this study, swell always propagated close to perpendicular to the radar beam, resulting in the larger calibration coefficient values as shown in Fig 3.8a when swell was included in the calibration. This justifies the use of a hybrid model, like the one presented in this study, that treats swell and wind waves differently.

Previous swell models (Lipa and Barrick, 1980; Bathgate, 2006) define R_s as being proportional to $H_s^2 \cos^2 \theta_s$ (where H_s and θ_s are the RMS swell wave height and direction of swell, respectively). This definition leads to singularities when swell propagates perpendicular to radar beam direction ($< 30°$ from perpendicular) and leads to inaccurate swell height estimates. Although our model [see Eq. (3.5)] does not consider swell propagation direction, its swell estimates (Figure 3.9c, d) are better correlated to in situ data than those from the $\cos^2 \theta_s$ model (Figure 3.19). This better performance is present despite the variation in θ_s found at each calibration site (see Table 3.2). The swell mean cross angle, θ_s, at sites O2 and N4 is $68.2°$ and $73.3°$, respectively. According to the $\cos^2 \theta_s$ model these cross angles should create a 65% ($= \cos^2(68.2)/\cos^2(73.3)$) increase in α_s. In our model, any directional effects are included in the calibration factor (α_s), and only a 40% increase is found (0.05 to 0.07, see Figure 3.9c, d). Likely, the wide radar beamwidth ($15^o - 35°$) at these large radar beam angles ($22° - 55°$), combined with a finite spreading parameter of the swell waves, result in significant deviation from the $\cos^2 \theta_s$ model. Our findings indicate that in the nearshore the swell models of Lipa and Barrick (1980) and Bathgate et al. (2006) overestimate the effect of direction at these swell cross angles, close ($< 30°$) to perpendicular. If this is

related to the VHF frequencies of our HF radar or to other parameters is not clear at present and merits further investigation.

3.5.2 Inverted bulk wave parameters

The RMS error between in situ and radar inverted wave height ranges from 0.16 to 0.25 m with correlation coefficients r ranging from 0.86 to 0.94. In Table 3.7, we compare our results with those from other studies that have used HF radars of different operating frequency (7 to 24.5 MHz) and different (theoretical and empirical) inversion methods. The lowest wave height RMS error in our study is similar to the lower values reported by those studies while our maximum value is the smallest reported. At the same time our correlation coefficients between inverted wave heights and in situ estimates range from 0.86 to 0.94. In addition, the errors in wave period estimates for both mean and peak period seem to have the smallest maximum value amongst those reported previously (see Table 3.7).

In Figure 3.20, RMS errors in wave height from each site are plotted against the following parameters: (i) range from the radar site, (ii) beam angle, (iii) difference in peak energy level between first and second- order peaks, and (iv) first-order peak broadening parameter (i.e., half power width). Qualitatively we see that the error tends to increase with range and beam angle. The largest errors in wave heights are found for sites N5 and N6, which correspond to those with the highest range. Although they also correspond to high beam angles, these are not higher than that for site N2. Sites N5 and N6 are located over Diamond Shoal, an area characterized by shoaling and breaking wave conditions (Kumar et al., 2013) which can cause a broader backscatter signal in the radar (Graber and Heron, 1997). The wave height error shows a linear correlation with the

broadening parameter (see Figure 3.20c) where again sites N5 and N6 indicate a high broadening of the spectrum. It has been shown that the second-order spectra at large radar beam directions (>45^o) from the boresight, can be inaccurate due to signal contamination by sidelobe interference (Haus et al., 2010). The calibration sites N4 and O2 have the lowest radial beam angles (<40^o), while all other sites are expected to be more susceptible to sidelobe interference. Despite this issue, radar-derived wave spectra performed well at locations with high beam angles (see N1, N2 and N3 in Figure 3.20b). Wave height RMS error seems to be reduced with increasing values of first to second-order peak energy ratio (see Figure 3.20c). This ratio is inversely correlated with total wave height (not shown here), something not unexpected given that bigger the waves the higher the second-order peak energy. This is in support of the theoretical limitation $0.15 < k_0 m_o < 1$ (or $0.42 < k_0 H_{rms} < 2.82$) for the application inversion as presented by Barrick (1977b). However, as our data reveal this hard limit is not always applicable as there are cases where the inversion produces good results even under conditions exceeding these limits. We suggest that for practical applications, this ratio could be used as an indicator, perhaps combined with the broadening parameter, of the accuracy of wave height estimates from HF radars.

The peak and mean frequencies (compare Figure 3.11 and 3.13) and the corresponding peak and mean wave periods are as accurate as those from other wave inversion models (see Table 3.7). RMS error of mean wave period is 0.79-0.84 s with correlation coefficient r of 0.8-0.95. RMS error for peak wave period is 1.38 to 2.16 s and r is 0.51-0.84. These results compare favorably to other studies (Gomez et al., 2015; Wyatt et al., 2006) in which the RMS error of mean wave period is 0.81-2.81 s with r

0.52-0.81, and those for peak wave period RMS error is 1.46-4.23 s with r is 0.33-0.76 (Gomez et al. 2015).

3.5.3 Full spectra inversions

In individual spectra comparisons (A-H in Figure 3.10 and A-G in Figure 3.12), during times when wind wave RMS wave height is below 1m, the spectra are accurately reconstructed (C-H in Figure 3.10 and C-G in Figure 3.12). Furthermore, using a constant value for $\alpha(f)$ allows for the reconstruction of spectrum at frequencies beyond those used in the calibration. However, this is valid only when the weighting function of Barrick (1977b) is applied [see Eq. (3.3)], which suppresses the harmonic and corner reflections peaks that might exist in the spectrum. Doppler spectra at events A and B are flagged as poor quality due to the Bragg peak not being 5dB above the second-order sidebands. Although the higher frequency range (wind seas) of the spectrum is inverted well, the lower frequency part of it is less accurate (see Figures 3.10 and 3.12). This is attributed to the saturation of the Doppler spectrum due to the larger swell wave heights (>1 m) at these events that contribute to merging of the first and second-order parts of the spectrum. Although this affects the inversion of the wave spectrum at low wave frequencies (<0.15 Hz) the effect is less severe at higher wave frequencies (>0.15Hz); despite this, the total wave height is still accurately reconstructed (Figures 3.11 and 3.13). The inverted spectra estimates extend up to 0.5 Hz, but no in situ spectral estimates are available for these high frequencies; however, the energy roll-off observed in Figure 3.12 agrees with the expected theoretical high-frequency wave energy roll-off asymptotes (Hasselmann et al., 1973).

3.5.4 Wind and Wave Directions

Wave direction estimates from the radar seem to be more accurate than those for wind direction (compare Figure 3.14 left and middle panels). However, the wind measurements were from some 29 km offshore (see Figure 3.1) and do not capture the influence of the coastline (see Wu et al., 2017). The wave energy weighted wind direction vectors were well correlated (complex correlation coefficient (r) values of 0.68-0.77) with a mean angle of 12°. In terms of RMS errors, our error of 32°-39° is similar to those of Wyatt et al. (2006) who used a more complicated theoretical inversion and obtained RMS errors of 23°-48° with linear r values 0.66-0.89. For mean wave direction, the hybrid model results in RMS errors of 15°-38° with complex r magnitudes of 0.65-0.8 and an angle of -33° to 9° (mean of absolute values of 13°). This compares well to the study of Wyatt et al. 2009 where an RMS error of 21° was found. For peak wave direction, we find an RMS error of 20°-46° with complex r (0.48 to 0.7) and mean complex *r* direction of 11° which is smaller than those for mean wave direction.

3.6 Conclusions

We have introduced an empirical hybrid model for VHF radar wave spectra estimates that treats swell and wind waves separately. Using Barrick's (1977b) deep-water weighting function results in wind wave coefficients $(a(f)^{+}_{SNR})$ that can be assumed to be constant (= 0.255) across all ocean wave frequencies. We believe this may be applicable universally but experimental confirmation using radar systems of different frequencies is required. Differences with coefficients found by other studies are attributed to whether Barrick's (1977b) weighting function is utilized, which is something that we

strongly recommend to suppress interference by harmonics generated by the EM wave and ocean wave interactions.

A separate coefficient Eq. (3.5) for swell is needed that does not correlate well to $\cos^2\theta_s$ at $\pm 30^\circ$ from perpendicular. After calibration, this hybrid model has the ability to accurately reconstruct wave spectra even when swell is propagating close to perpendicular to the radar. Application of the swell module requires that swell propagation direction is constrained by site location, and therefore can be assumed roughly constant. Although this model requires calibration for locations that have different cross angles ($\theta_s, i.e.$ the angle between the radar beam direction and swell propagation direction), it shows a significant improvement from theoretical $\cos^2\theta_s$ models (Lipa and Barrick, 1980; Bathgate et al., 2006) of swell (compare Figure 3.19 to Figure 3.9 lower panels) beam direction.

Both swell and wind wave spectra are reconstructed at similar levels of accuracy to previous studies (e.g., Wyatt et al., 2009; Gomez et al., 2015; Lopez et al., 2016), and the radar estimated wave spectra show similar trends at high frequencies ($f > 0.2$ Hz) which closely align to f^{-4} and f^{-5} wave energy roll-off (see Figures 3.10, and 3.12). Note that in this study (48 MHz), accurate wave spectra reconstruction is limited to high frequencies when high energy of swell (>1 m) is present, although total RMS wave height is still accurately estimated.

This hybrid method presented here is characterized by its simplicity, requiring a single calibration coefficient for wind wave spectrum and calibration and frequency width coefficient for swell. However, there is some effect of direction, resulting in the

different swell calibration constants between calibration sites O2 and N4. The lack of a radar inversion swell method for swell propagating at large cross angles results in the requirement of this model to be calibrated separately at locations where the cross angle of swell changes significantly. A more detailed analysis, from both a theoretical and experimental basis, of swell's effect on the radar signal when its propagation direction is close to perpendicular is needed for reconstructing swell wave spectra from radar Doppler spectra at uncalibrated locations.

The MATLAB software scripts for implementation of the inversion model presented in this paper [the Wave Radar Inversion Code (WaveRIC)] are available online (Cahl et al., 2019).

Table 3.1: Details of instrument, water depth, data availability, range of the site from the VHF radar, angle of the radar beam to each site from the radar boresight, and mean SNR for the first- and second-order peaks extracted from the radar Doppler spectra.

Site	**Instrument Type**	**Depth (m)**	**Deployment Period (2010)**	**Range (km)**	**Beam Angle (°)**	**First-order mean SNR (dB)**	**Second-order mean SNR (dB)**
N1	AQD	4.7	Feb, 9 - 22	0.7	51.9	41.2	27.4
N2	AQD	7.0	Feb, 11 - 21	1.8	55.8	39.6	24.0
N3	AQD	6.0	Feb, 9 - 22	1.9	45.8	41.3	24.9
N4	ADCP	8.8	Feb, 9 - 22	2.0	38.2	41.6	25.2
N5	ADCP	6.1	Feb, 2 - 21	4.2	46.1	28.1	17.5
N6	AQD	4.7	Feb, 2 - 21	4.2	53.5	26.0	17.7
O2	ADCP	10.7	Feb, 4 – Mar, 20	3.3	22.3	39.8	26.5

Table 3.2: Summary of bulk total and partitioned (swell/wind wave) wave conditions (i.e., RMS wave height, frequency, and direction) at sites O2 and N4 for each of the events (A-H) shown in Figure 3.3. The corresponding VHF radar Doppler spectra characteristics are also listed.

Site		**Event**							
		A	B	C	D	E	F	G	H
O2	Time (day)	6.20	8.00	10.10	11.54	12.54	13.7	16.54	23.16
	Total H_{rms} (m)	2.30	2.00	1.10	1.20	1.70	1.30	0.70	0.80
	Swell H_{rms} (m)	1.10	2.00	0.20	0.50	1.40	0.60	0.20	0.20
	Wind H_{rms} (m)	2.00	1.30	1.10	1.00	0.90	1.20	0.70	0.80
	Peak freq. f_P (Hz)	0.10	0.07	0.15	0.10	0.08	0.14	0.12	0.13
	Mean freq. f_m (Hz)	0.10	0.09	0.15	0.12	0.09	0.13	0.13	0.14
	Mean swell direction (°)	99.0	74.6	102.6	46.0	87.0	76.0	152.5	120.0
	Swell cross direction (°)	50.6	75.5	-	76.0	63.0	-	-	-
	Mean wind-wave direction (°)	109.0	76.8	109.7	54.0	74.0	54.0	140.0	130.0
	Wind-wave cross-direction (°)	40.0	73.0	40.00	84.0	75.0	84.0	10.0	19.0
	Noise (dB)	-1.00	-0.50	-6.20	-1.04	1.22	-0.60	1.74	-1.08
	$(\sigma_1/\sigma_2)_{peak}$ (dB)	1.30	1.60	6.00	8.00	2.90	6.30	9.60	75.00

Site		Event							
		A	B	C	D	E	F	G	H
N4	Time (day)	6.21	7.96	10.08	11.54	12.54	13.67	16.54	23.16
	Total H_{rms} (m)	-	-	1.10	0.96	1.70	1.20	0.70	-
	Swell H_{rms} (m)	-	-	0.20	0.4	1.00	0.60	0.20	-
	Wind H_{rms} (m)	-	-	1.00	0.85	0.98	1.00	0.70	-
	Peak freq. f_P (Hz)	-	-	0.14	0.1	0.07	0.14	0.12	-
	Mean freq. f_m (Hz)	-	-	0.16	0.12	0.10	0.13	0.14	-
	Mean swell direction (°)	-	-	100	73	85	86	138	-
	Swell cross direction (°)	-	-	-	87	79	-	-	-
	Mean wind-wave direction (°)	-	-	114.0	70.0	78.0	71.0	151.0	-
	Wind-wave cross direction (°)	-	-	51.0	84.0	87.0	85.0	14.0	-
	Noise (dB)	-	-	-2.25	5.50	3.90	3.70	8.00	-
	$(\sigma_1/\sigma_2)_{peak}$ (dB)	-	-	12.20	9.20	4.00	13.80	6.10	-

Table 3.3: RMS error, linear correlation coefficient (r), and regression slope derived from the comparison of wave bulk parameters and partitioned RMS wave height estimate from the inverted and in situ spectra for all sites. Note: sites O2 and N4 were used for the calibration of the model.

	N	H_{rms} *(Total)*			H_{rms} *(Swell)*			H_{rms} *(Wind waves)*		
		Error (m)	r	Slope	Error (m)	r	Slope	Error (m)	R	Slope
O2	413	0.21	0.92	0.86	0.23	0.83	0.78	0.17	0.89	0.89
N1	407	0.16	0.92	0.91	0.18	0.82	0.86	0.13	0.90	0.91
N2	306	0.19	0.94	0.80	0.22	0.88	0.72	0.13	0.89	0.84
N3	450	0.20	0.93	0.79	0.16	0.89	0.80	0.17	0.90	0.75
N4	214	0.17	0.93	0.89	0.15	0.91	0.89	0.14	0.90	0.86
N5	334	0.17	0.92	0.94	0.21	0.79	0.85	0.14	0.92	0.95
N6	627	0.25	0.86	1.04	0.23	0.73	0.87	0.21	0.85	1.09

Table 3.4: As in Table 3.3, but for mean and peak frequency and mean and peak wave period.

	N	*Peak frequency* (f_P)			*Mean frequency* (f_m)			*Peak period* (T_P)			*Mean period* (T_m)		
		Error (Hz)	*r*	Slope	Error (Hz)	*r*	Slope	Error (s)	*r*	Slope	Error (s)	*r*	Slope
O2	413	0.03	0.60	0.93	0.01	0.80	0.90	1.93	0.68	0.90	0.84	0.80	0.99
N1	407	0.02	0.69	0.95	0.01	0.90	0.98	1.63	0.71	0.90	0.82	0.94	1.02
N2	306	0.02	0.76	0.97	0.01	0.90	1.01	1.68	0.79	1.01	0.81	0.95	0.99
N3	450	0.02	0.77	0.97	0.01	0.90	0.98	1.38	0.84	0.99	0.79	0.95	1.02
N4	214	0.02	0.75	0.95	0.01	0.90	0.98	1.61	0.76	0.99	0.82	0.94	1.01
N5	334	0.03	0.58	0.94	0.01	0.80	1.01	2.03	0.64	1.02	0.79	0.83	0.99
N6	627	0.03	0.51	0.94	0.01	0.80	1.02	2.16	0.51	0.99	0.81	0.90	0.98

Table 3.5: RMS errors (bottom left) and linear correlation coefficients estimates (top right) between sites, for both in situ and HF radar inverted estimates. Values shown were obtained using data (N=155) when all sites were operational. The values shown in each table cell are listed as in situ/inverted values.

	Linear correlation coefficient (*r*) – (*r in situ*) / (*r inverted*)								
	O2	**N1**	**N2**	**N3**	**N4**	**N5**	**N6**	**HF**	
	1	0.97 /0.89	0.97 /0.9	0.97 /0.9	0.97 /0.91	0.96 /0.87	0.95 / 0.78	*0.92*	**O2**
		1	0.98 /0.84	0.98 /0.9	0.98 /0.92	0.96 /0.8	0.97 /0.71	*0.87*	**N1**
			1	0.99 / 0.92	0.99 /0.88	0.95 /0.84	0.96 /0.74	*09*	**N2**
O2	1			1	0.99 / 0.96	0.96 /0.85	0.97 /0.75	*0.9*	**N3**
N1	0.17 / 0.16	1			1	0.97 / 0.83	0.98 /0.74	*0.9*	**N4**
N2	0.19 / 0.16	0.09 / 0.17	1			1	0.96 / 0.86	*0.99*	**N5**
N3	0.15 / 0.17	0.09 /0.14	0.09 / 0.11	1			1	*0.76*	**N6**
N4	0.15 / 0.15	0.09 / 0.13	0.08 / 0.15	0.08 /0.1	1			*1*	**HF**
N5	0.12 / 0.22	0.14 / 0.23	0.17 / 0.25	0.13 / 0.26	0.13 / 0.25	1			
N6	0.17 / 0.35	0.11 / 0.35	0.03 / 0.38	0.11 / 0.39	0.1 / 0.38	0.12 / 0.22	1		
HF	*0.17*	*0.19*	*0.18*	*0.21*	*0.17*	*0.19*	*0.34*	*1*	
	RMS Errors (in m) – (*RMSE in situ*) / (*RMSE inverted*)								

Table 3.6: Statistical comparison of in situ and inverted estimates of wind direction (θ_{wind}), mean wave direction (θ_{wm}), and peak wave direction (θ_{wp}) for all sites. Values of RMS error (°), complex correlation coefficient (r) and angle of r (°) are listed. N is the number of data points used in the estimations.

	N	θ_{wind}			θ_{wm}			θ_{wp}		
		RMS Error (°)	Complex (r)		RMS Error (°)	Complex (r)		RMS Error (°)	Complex (r)	
			Magnitude	Angle (°)		Magnitude	Angle (°)		Magnitude	Angle (°)
O2	413	37	0.75	16	30	0.70	19	40	0.53	20
N1	407	36	0.70	6	15	0.78	6	20	0.70	10
N2	306	35	0.70	4	21	0.73	1	27	0.61	4
N3	450	39	0.68	12	18	0.80	9	26	0.70	16
N4	214	38	0.68	14	23	0.75	13	30	0.66	19
N5	334	35	0.77	12	22	0.73	-11	33	0.51	-4
N6	627	32	0.75	7	38	0.65	-33	46	0.48	4

Table 3.7: Comparison of the performance of the model presented in this study with other theoretical and empirical wave inversion methods reported in the literature and for different radar frequencies. RMS errors and correlation coefficients (r) against in situ measurements are presented.

Inversion Type	**Study**	f_{radar} **(MHz)**	H_{rms} **(m)**		T_P **(s)**		T_m **(s)**	
			RMS error (m)	r	**RMS error (s)**	r	**RMS error (s)**	r
Theoretical	Hisaki (2016)	24.5	0.15-0.86	0.63-0.76	-	-	0.26-0.95	0.69-0.82
	Wyatt et al. (2006)	7-10	0.19-0.46	0.55-0.94	-	-	1.27-4.56	0.13-0.81
	Wyatt et al. (2009)	16	0.28-0.32	0.96-0.97	-	-	-	-
Empirical	Chen et al. (2013)	7.5-25	0.19-1.29	0.45-0.82	-	-	-	-
	Gomez et al. (2015)	12	0.25-0.48	0.78-0.93	1.46-4.23	0.33-0.76	0.81-2.81	0.52-0.81
	Middleditch (2013)	8.34	0.36-0.70	0.35-0.51	0.89-2.44	0.3-0.57	0.72-1.26	0.28-0.50
	Ramos et al. (2009)	25.4	0.14-0.50	0.68-0.95	-	-	-	-
	Lopez et al. (2016)	12	0.18-0.36	0.88-0.96	-	-	-	-
	This Study	48	0.16-0.25	0.86-0.94	1.38-2.16	0.51-0.84	0.79-0.84	0.80-0.95

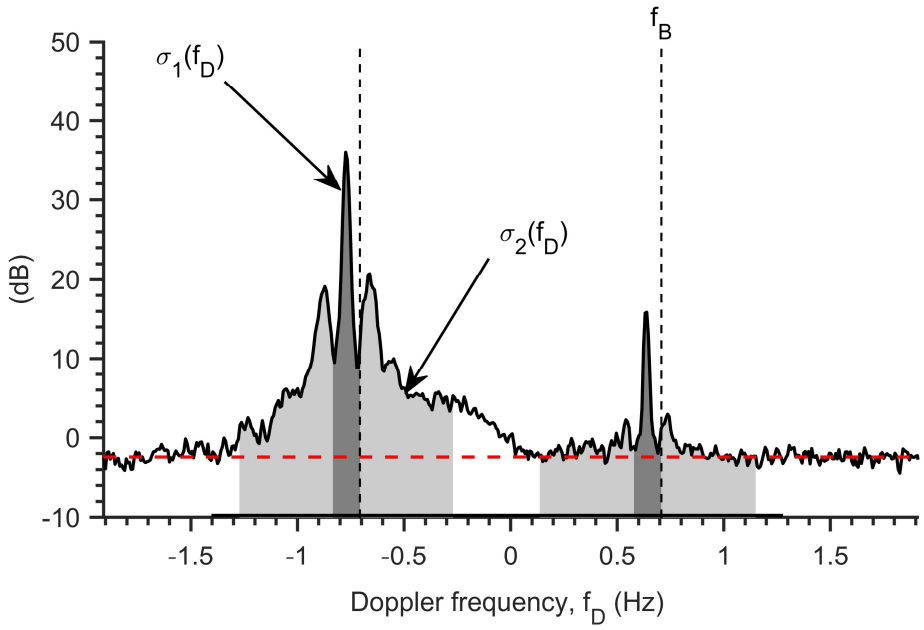

Figure 3.1: Example of HF Radar Doppler backscatter spectrum showing the first-($\sigma_1(f_D)$, dark gray) and second-order continuum ($\sigma_2(f_D)$, light gray) regions of the spectrum. The vertical dashed lines indicate the theoretical Bragg frequency and correspond to the frequency the first-order peaks should be appearing in the absence of surface currents. The horizontal dashed red line refers to the noise level. Data shown are from the 48-MHz, 12-antenna beam-forming radar system, used in this study.

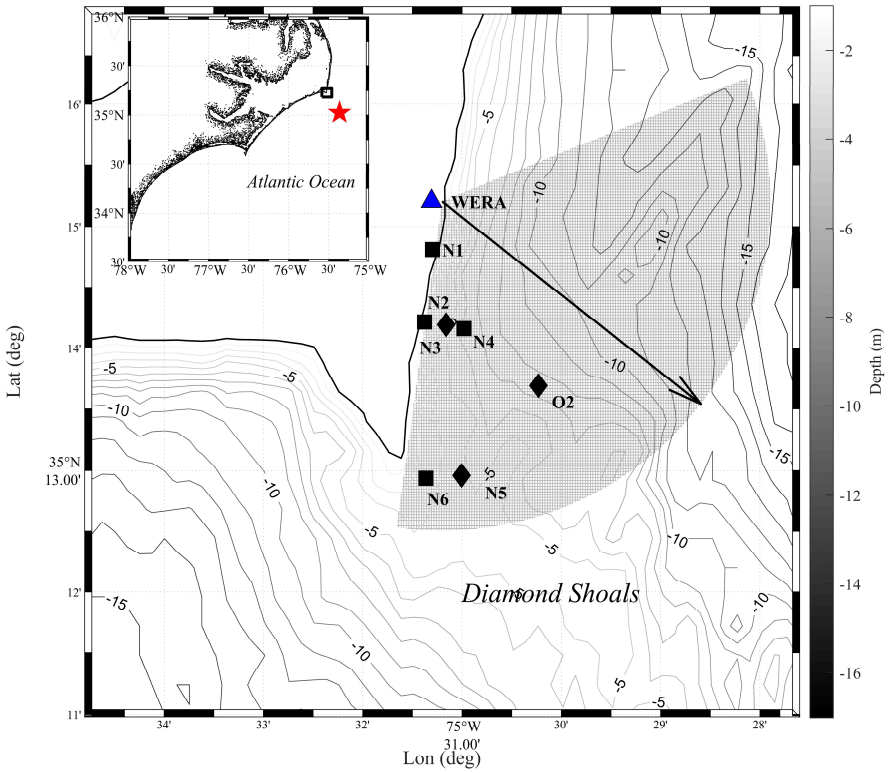

Figure 3.2: Experimental site location map showing the bathymetry around Cape Hatteras, (bathymetry data from https://www.ngdc.noaa.gov/mgg/bathymetry/relief.html), radar coverage area, and the locations of in situ measurements and Diamond Shoals buoy 41025 (red star in insert). The radar boresight direction (0º beam angle) is indicated by the dashed vector.

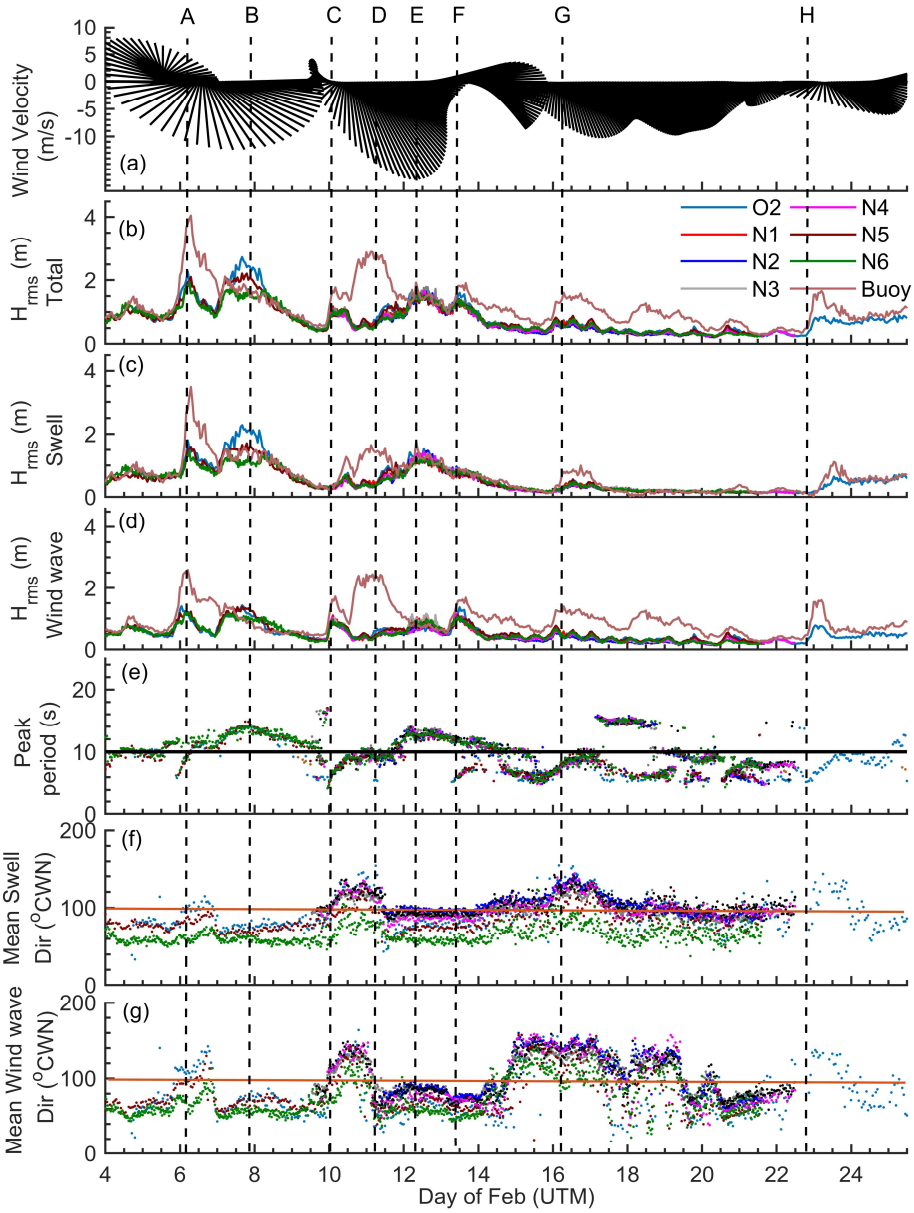

Figure 3.3: Time series of offshore winds (NOAA Buoy station 41025) and bulk wave parameters measured offshore at the buoy and instrumented sites (see Figure 3.2). (a) Wind vector diagram; (b) total RMS wave height for all sites, partitioned (c) swell and (d) gravity wave heights, (e) peak wave period (horizontal line at 10 s shows the separation between swell and wind waves), (f) and (g) mean wave direction (from true north) for (f) swell and (g) wind waves. Horizontal lines in (f) and (g) denote the direction perpendicular to the local coastline direction. Vertical lines marked A-H identify specific wind waves/swell events (see text for details).

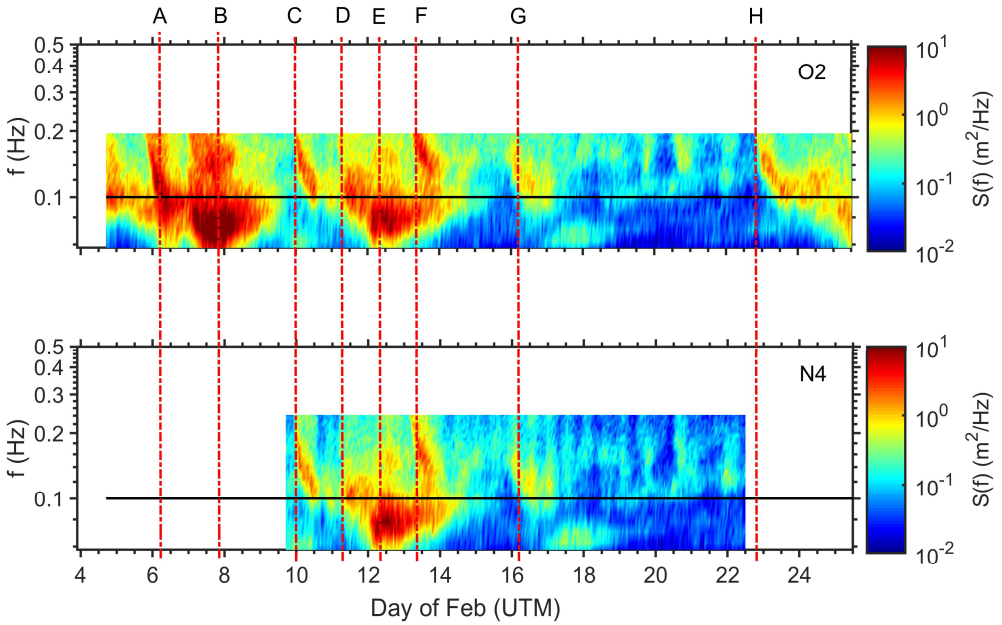

Figure 3.4: Time stack of estimated wave spectra $S(f)$ from sites (top) O2 and (bottom) N4. For instrument locations see Figure 3.1. The horizontal black line at 0.1 Hz denotes the separation of swell and wind wave bands. Vertical dashed lines refer to the time events shown in Figure 3.3 (see text for details).

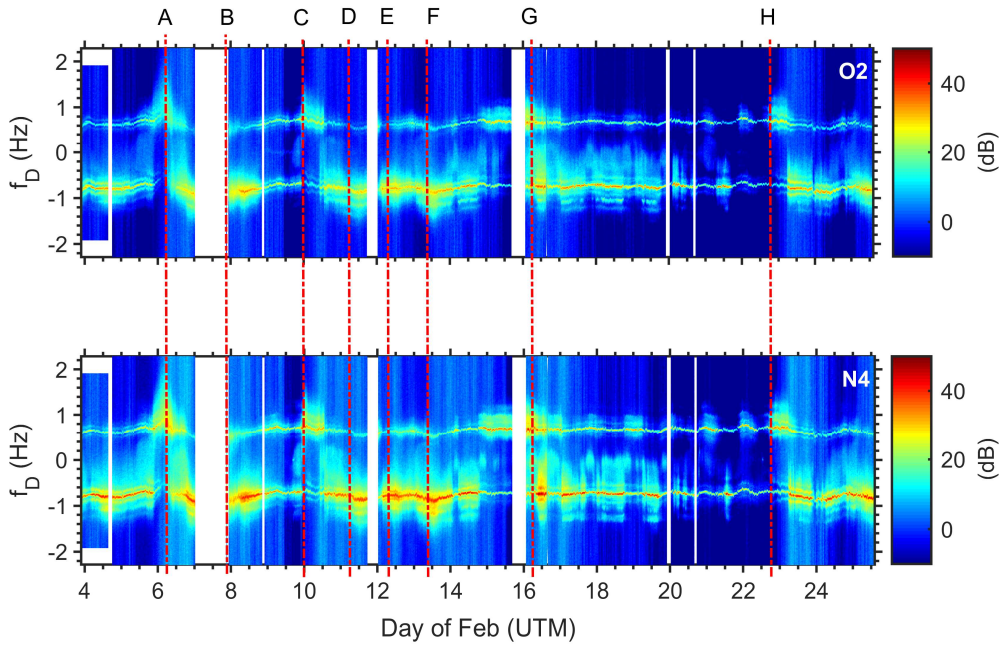

Figure 3.5: Time stacks of Doppler backscatter spectra estimated using the 48-MHz VHF radar. Each time stack represents Doppler spectra from the radar beam formed at locations corresponding to the locations of sites (top) O2, and (bottom) N4. Vertical dashed lines refer to the time events shown in Figures 3.3 and 3.4 (see text for details).

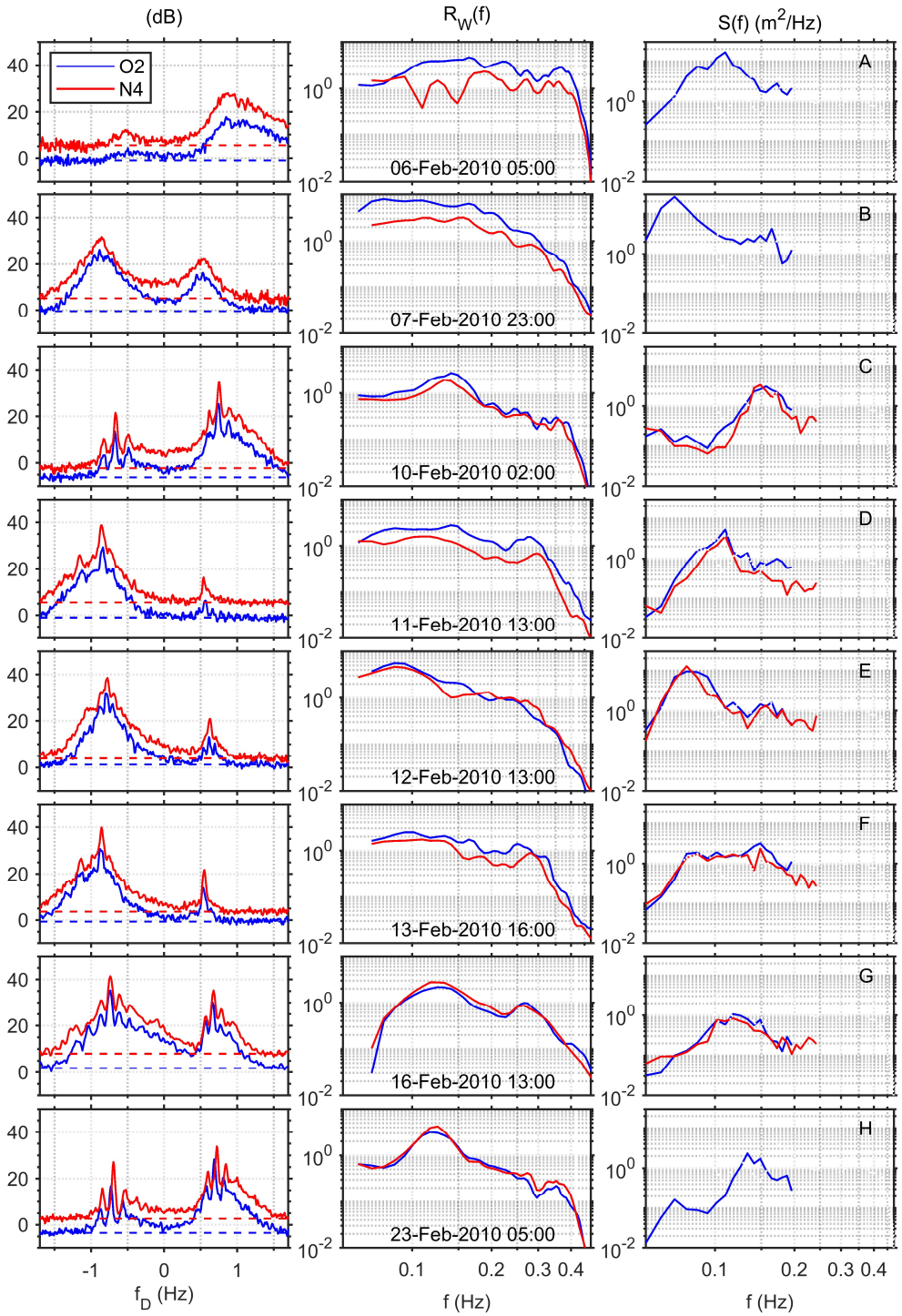

Figure 3.6: VHF radar data for events A-H (see Figures 3.3-3.5): (left) individual VHF radar Doppler spectra (the dashed lines denote the noise level for each spectrum), (center) second-order, weighted and normalized spectra $R_W(f)$ estimated from the Doppler spectra shown in the left column. (right) in situ estimates of wave spectra from the acoustic instruments. The blue and red curves correspond to sites O2 and N4, respectively.

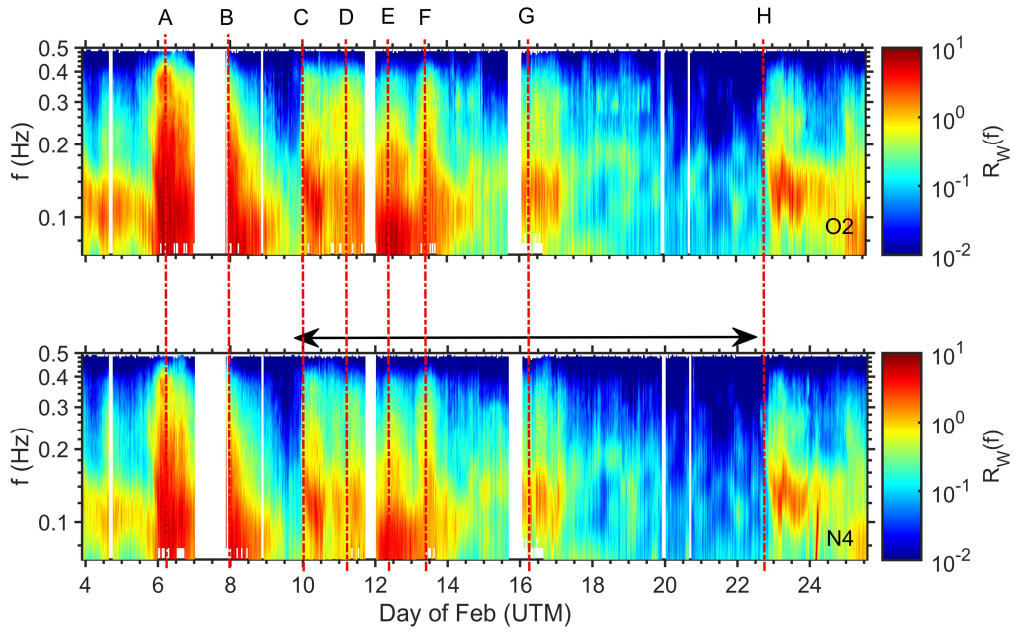

Figure 3.7: Time stack of weighted, normalized second-order radar spectra $R_W(f)$ at sites (top) O2 and (bottom) N4. The double arrow on the bottom panel defines the period of in situ data availability at site N4 used for calibration.

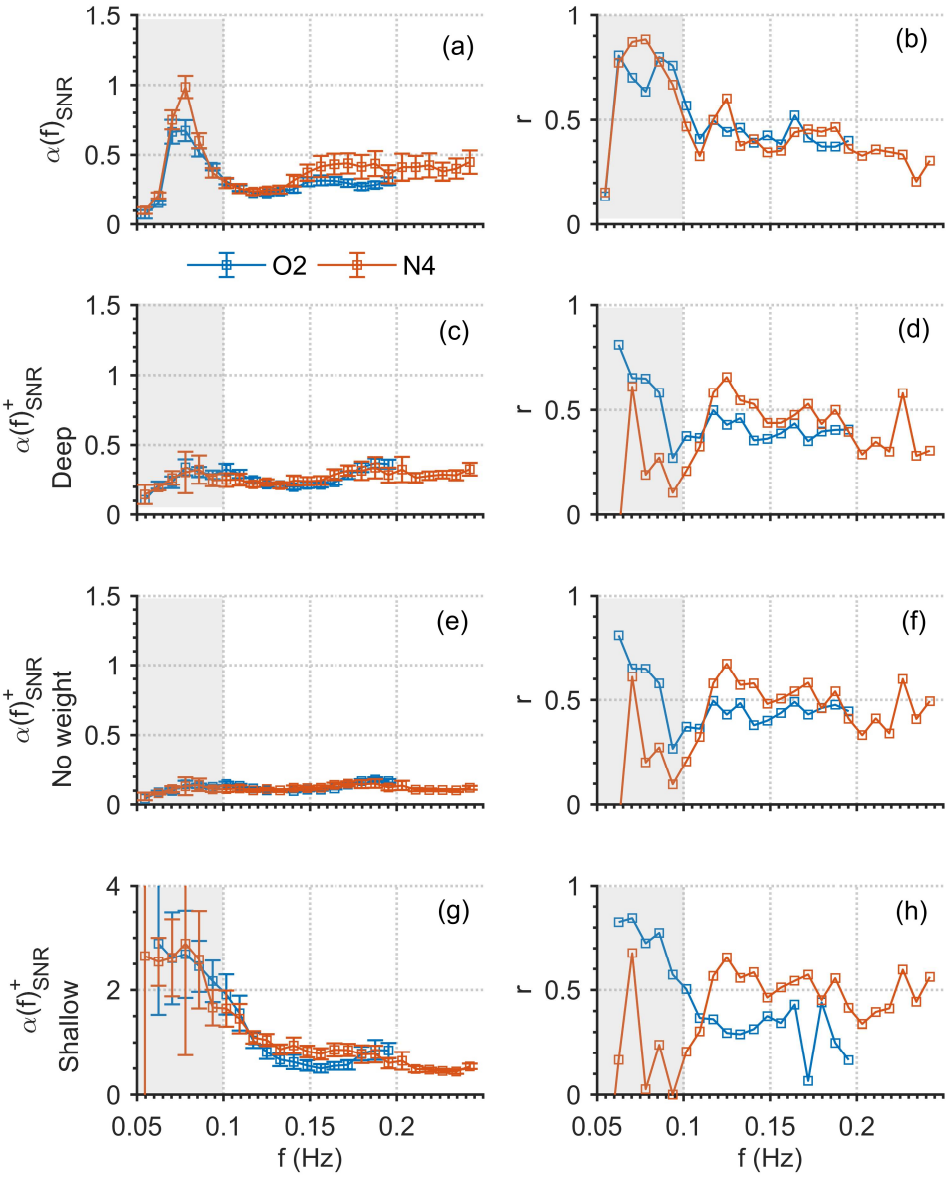

Figure 3.8: Estimates of frequency-dependent empirical calibration coefficients (Eq. (3.2)) using Doppler spectra that satisfied the (a) SNR and (c), (e), (g) SNR+ criteria (see text for details) at all sites. The α^{+}_{SNR} values were determined from normalized second-order spectra weighted using a deep-water weighting function ((c)), with no weighting applied ((e)), and weighted using a shallow water weighting function ((g)). (b), (d), (f), (h) The corresponding linear correlation coefficients. The shaded area in the diagrams delineates the swell frequency range.

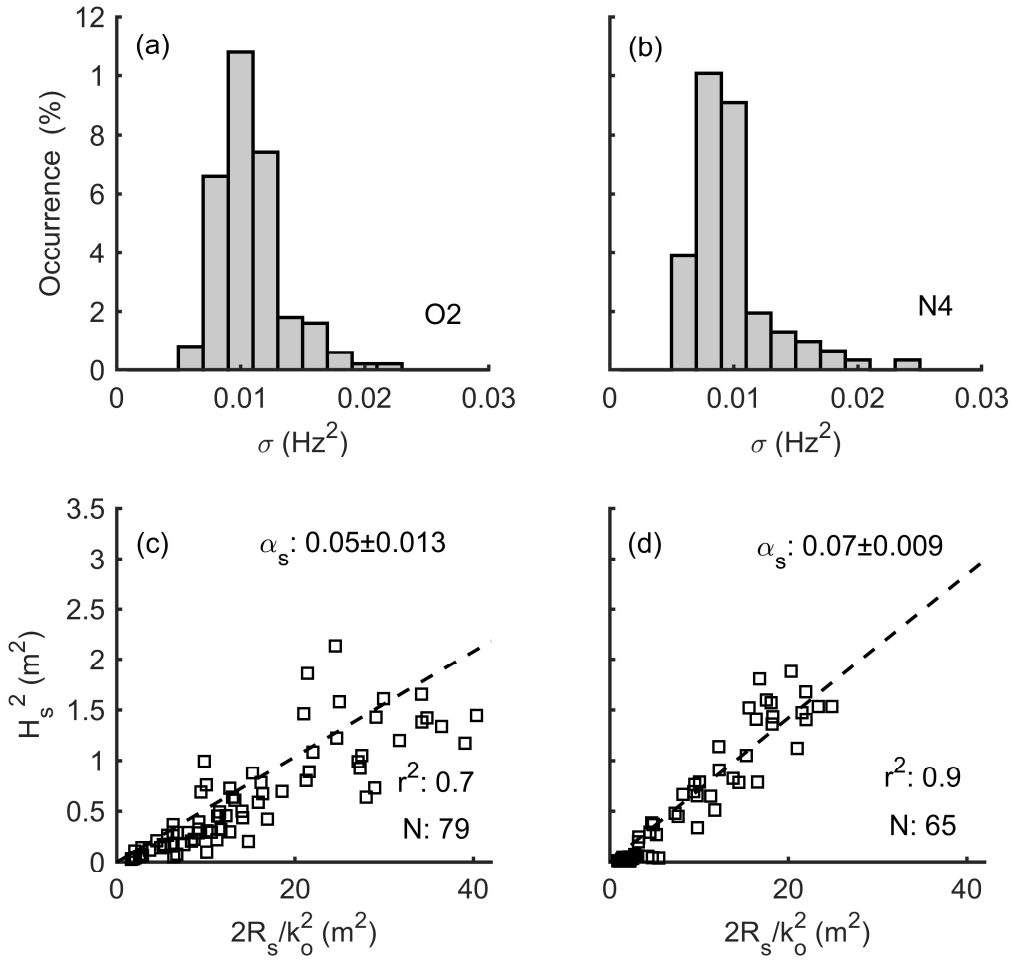

Figure 3.9: (a), (b) Histograms showing the distribution of the spreading coefficient σ for swell, estimated from the in situ wave spectra, and (c), (d)plots of regression analysis used to estimate the calibration coefficient α_s in the swell module for sites (left) O2 and (right) N4.

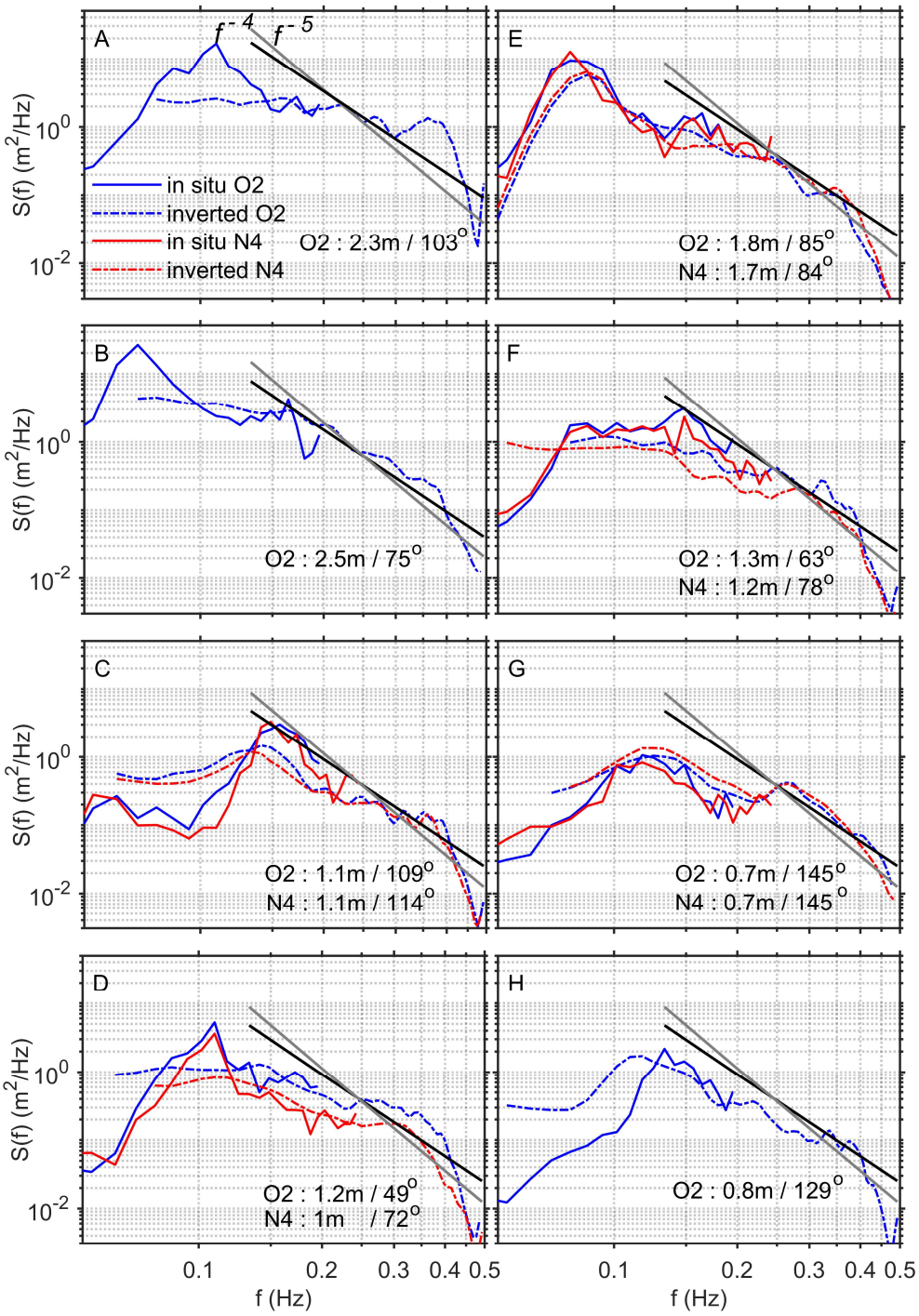

Figure 3.10: Examples of in situ (solid curves) and inverted (dashed curves) wave spectra for events A-H (see Figures 3.3 and 3.4) and for sites O2 (blue) and N4 (red). The f^{-4} and f^{-5} asymptotes are shown as black and grey lines, respectively. The corresponding in situ wave height/mean wave direction are shown in each panel.

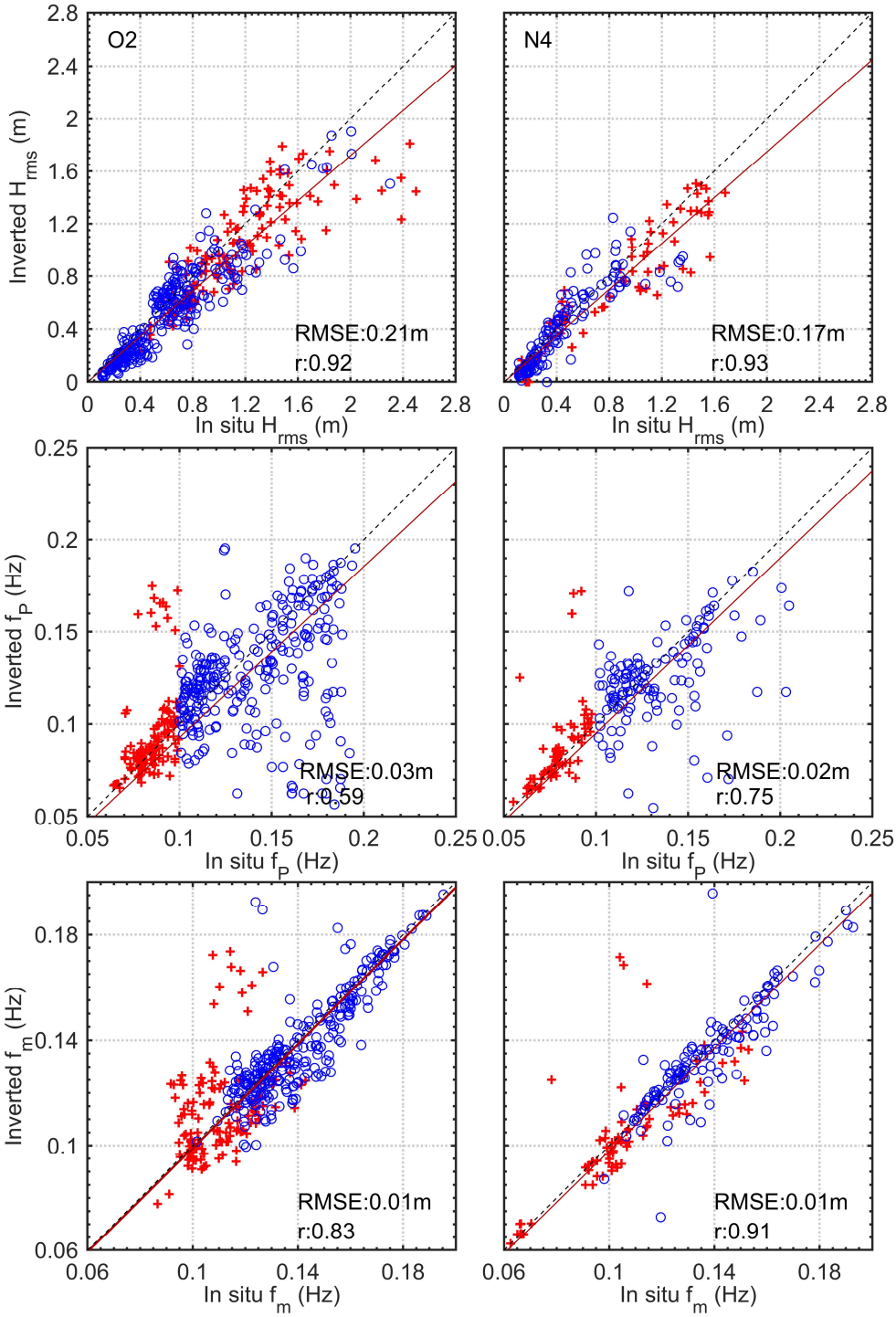

Figure 3.11: Comparison of wave bulk parameters (H_{rms}, peak (f_P) and mean (f_m) wave frequency) for sites O2 (left) and N4 (right). The 1:1 line (dashed) and the best regression line (red) are also shown. Red plus and blue open circles denote conditions that dominated swell and wind wave, respectively.

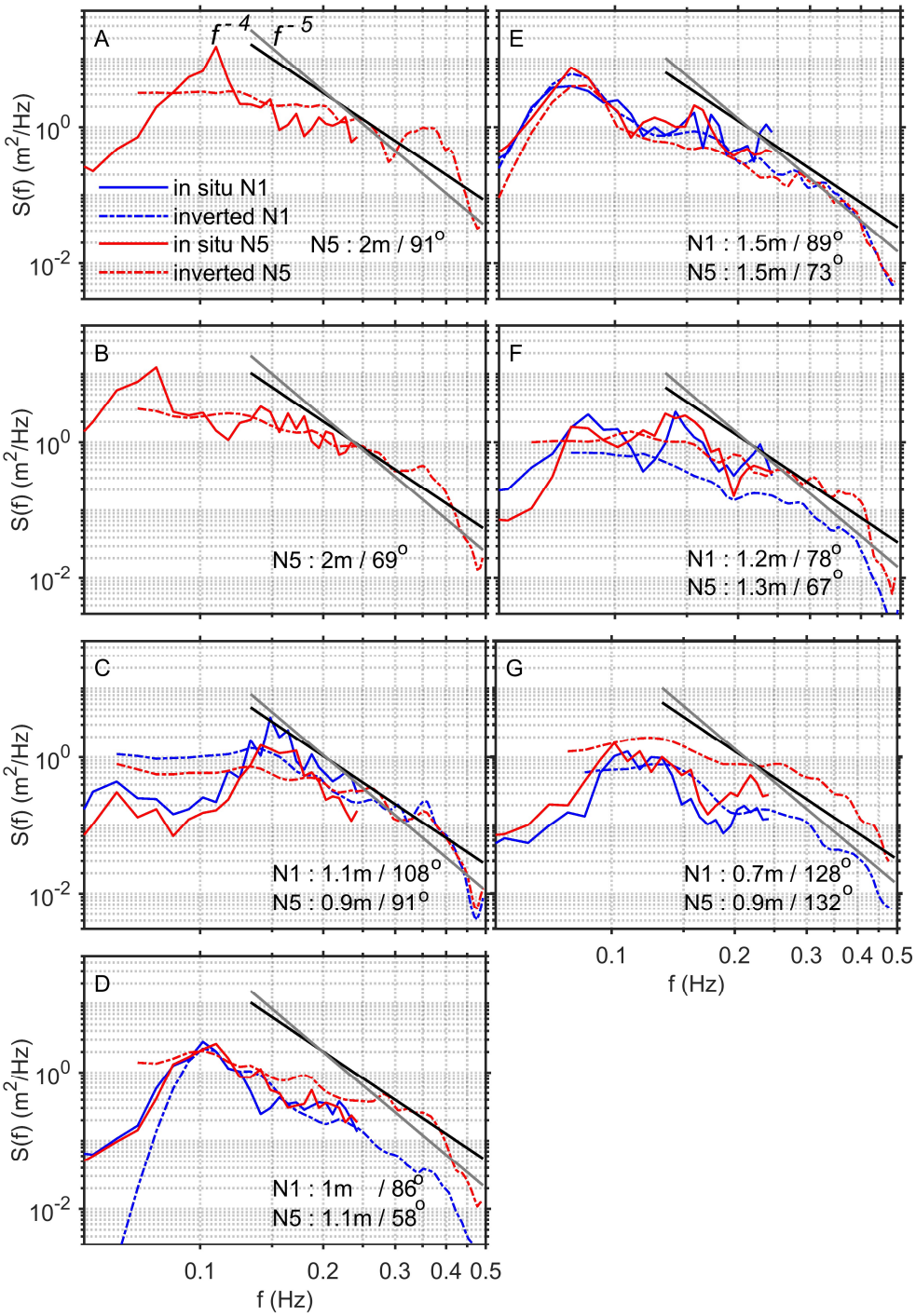

Figure 3.12: Examples of inverted (dashed curves) and in situ (solid curves) wave spectra for events, A-G (see Figures 3.3 and 3.4) and for sites N1 (blue) and N5 (red). The f^{-4} and f^{-5} asymptotes are shown as black and grey lines, respectively. The corresponding in situ wave height/mean wave direction are shown in each panel.

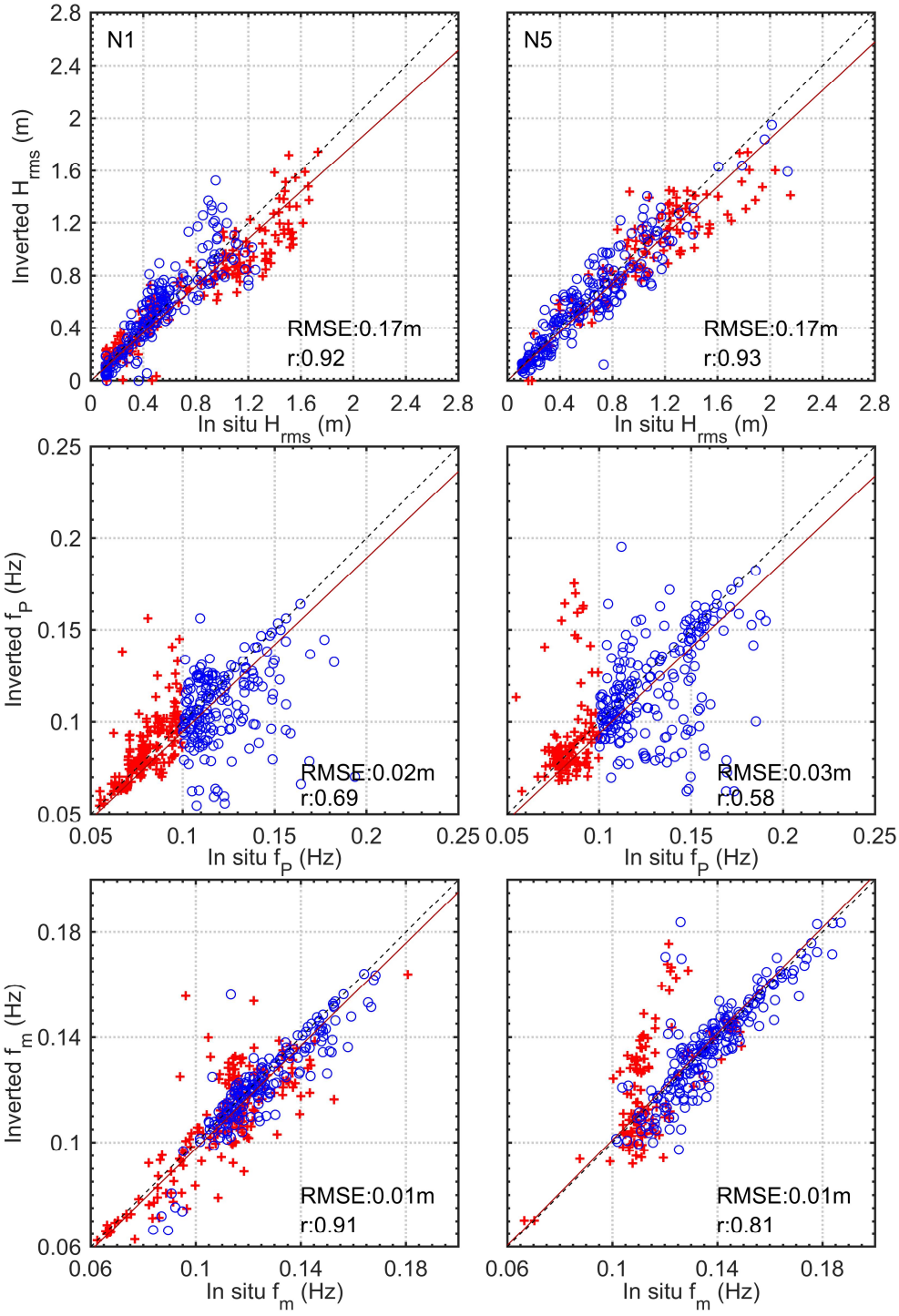

Figure 3.13: As in Figure 3.11, but for sites (left) N1 and (right) N5.

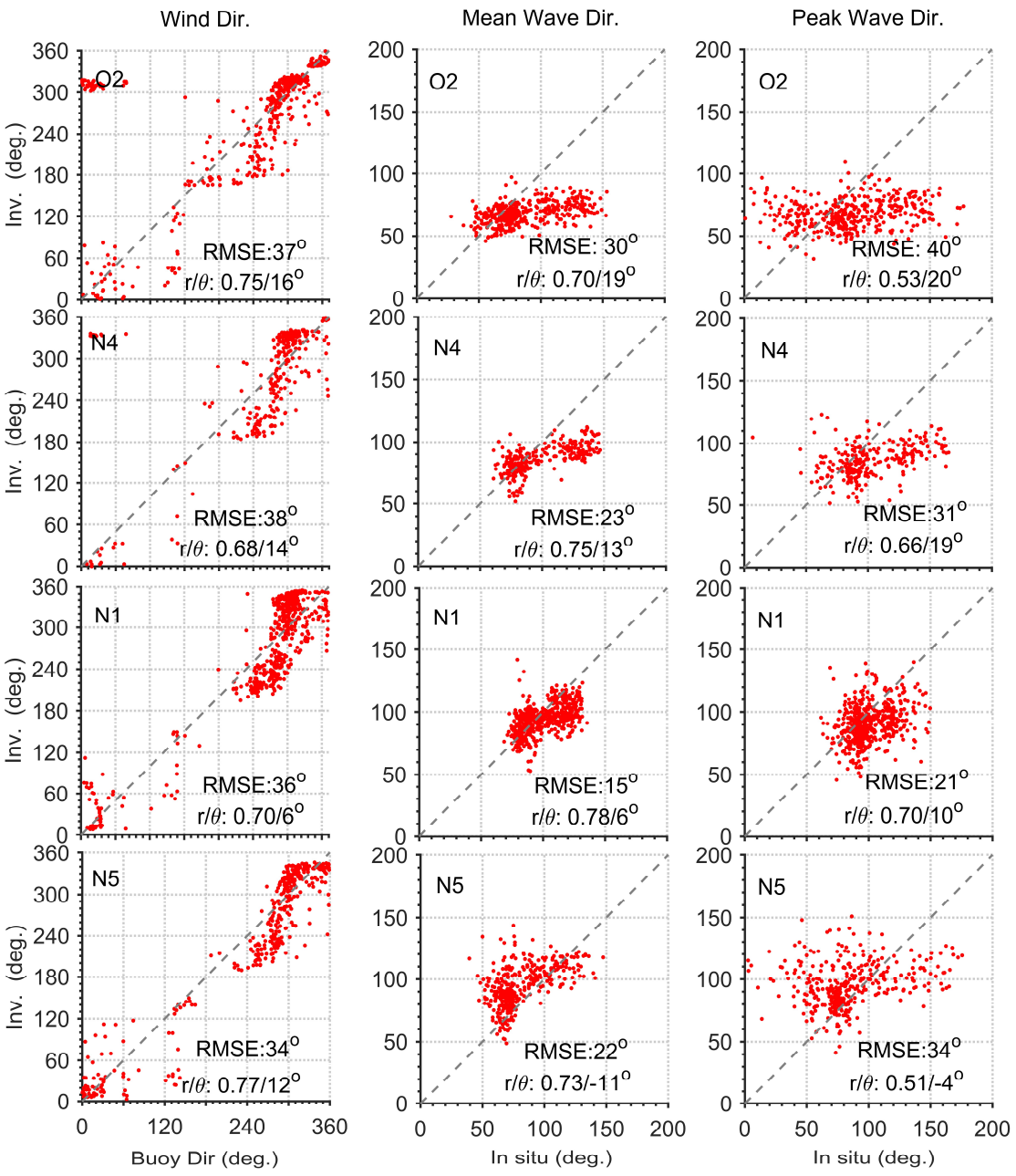

Figure 3.14: Scatter plots of inverted vs. in situ (left) wind direction, (center) mean wave direction, and (right) peak wave direction at sampling sites O2, N4, N1, and N5. The inverted radar wind direction was determined from the ratio of Bragg peak energies. In situ wind direction was collected from buoy 41025. Also shown in panels are complex correlation coefficients (r)/their corresponding angles (θ).

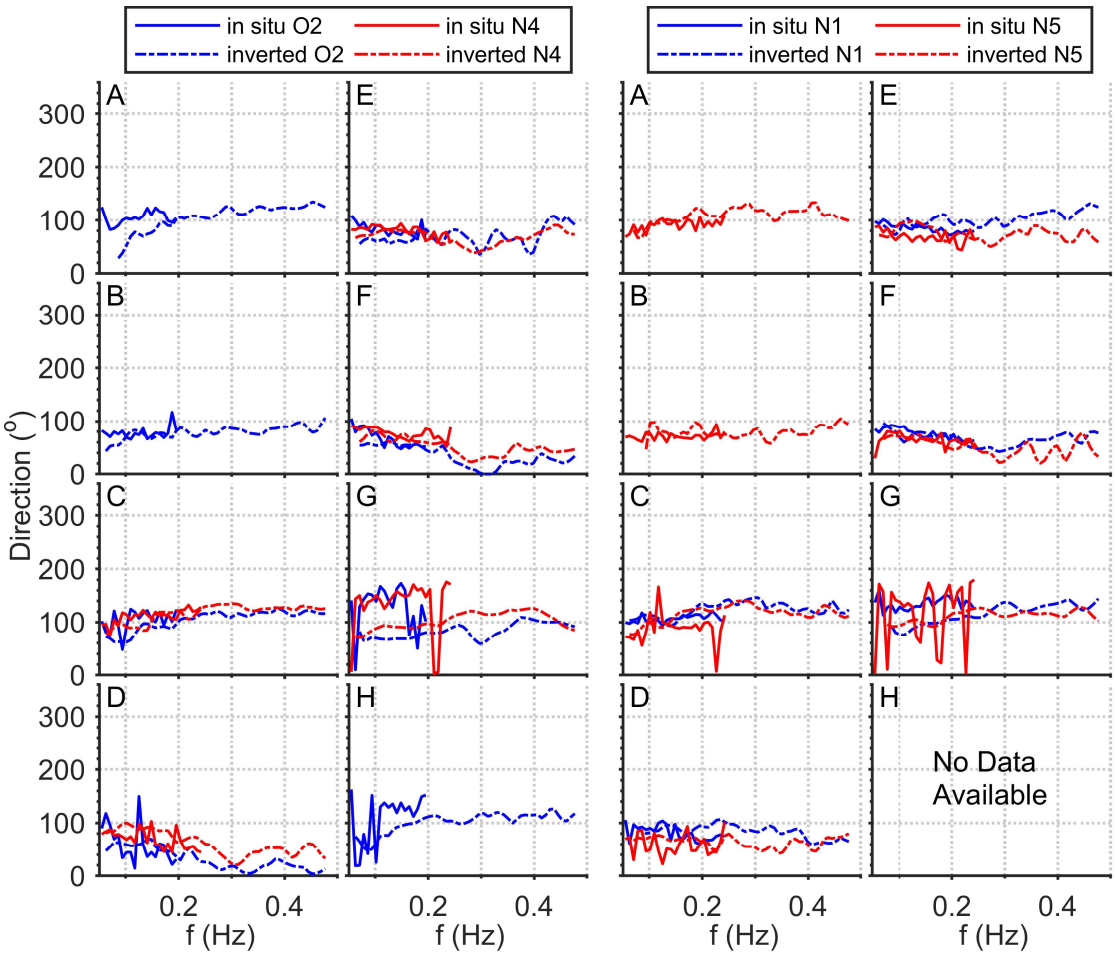

Figure 3.15: Examples of inverted ($\theta(f)_{inv}$) and in situ ($\theta(f)$) wave direction as a function of frequency for the events (A-H) identified in Figures 3.3-3.5.

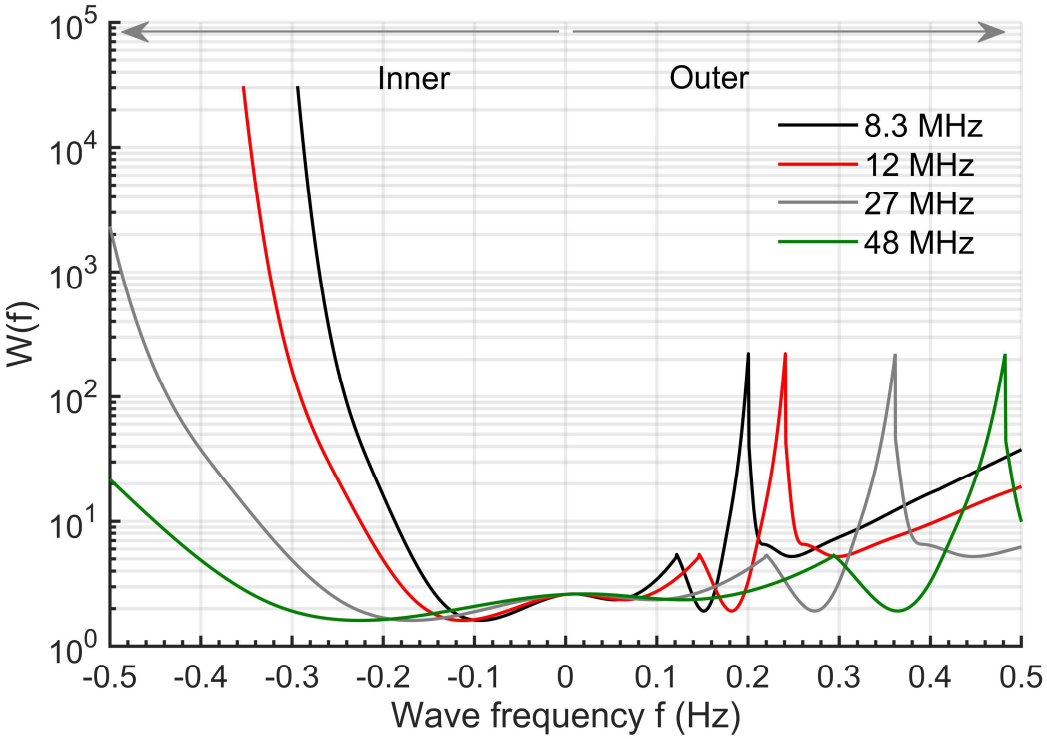

Figure 3.16: Diagram of Barrick's deep-water weighting function for selected radar frequencies. The weighting function is plotted in terms of ocean wave frequency, $f = f_D \pm f_B$. "Inner" denotes second-order sidebands toward the zero Doppler frequency (i.e., left/right of the Bragg peak for positive/negative Doppler frequencies). "Outer" denotes toward $\pm\infty$ Doppler frequency (i.e., right/left of the Bragg peak for positive/negative Doppler frequencies).

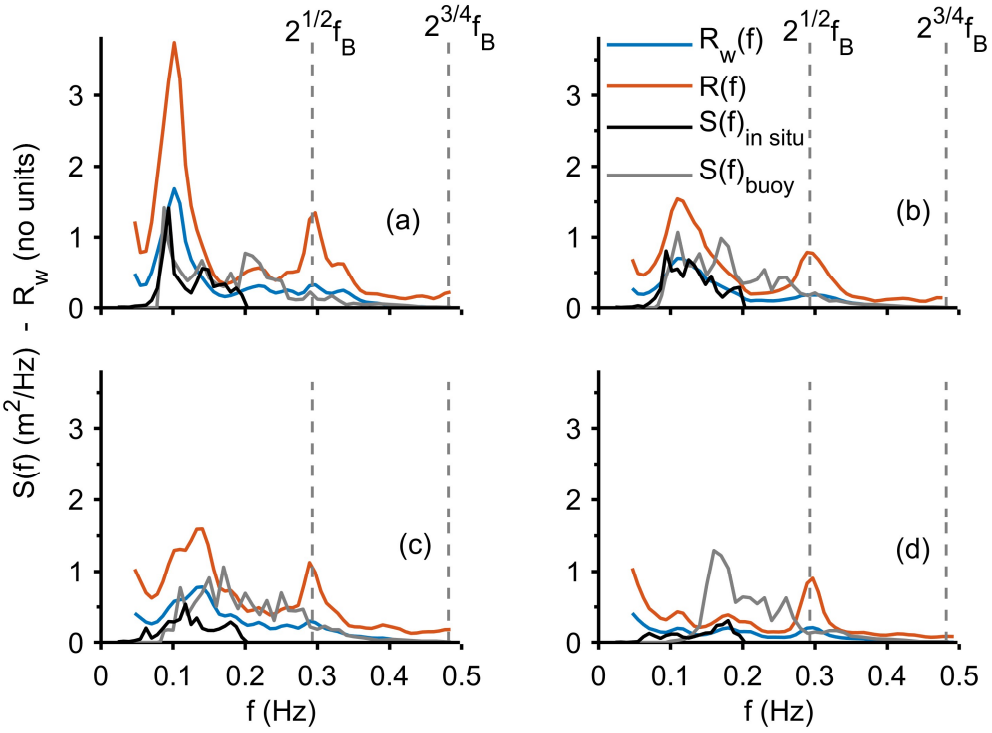

Figure 3.17: Examples showing how utilization of the weighting function contributes to reducing the effect of the singular peaks (located at $2^{1/2}f_B$ and $2^{3/4}f_B$, where f_B is the Bragg frequency) in the normalized second-order Doppler spectra from site O2. Here: R_W and R denote weighted and no-weighted normalized spectra, respectively; $S(f)$ denotes in situ wave spectra (in m^2/Hz).

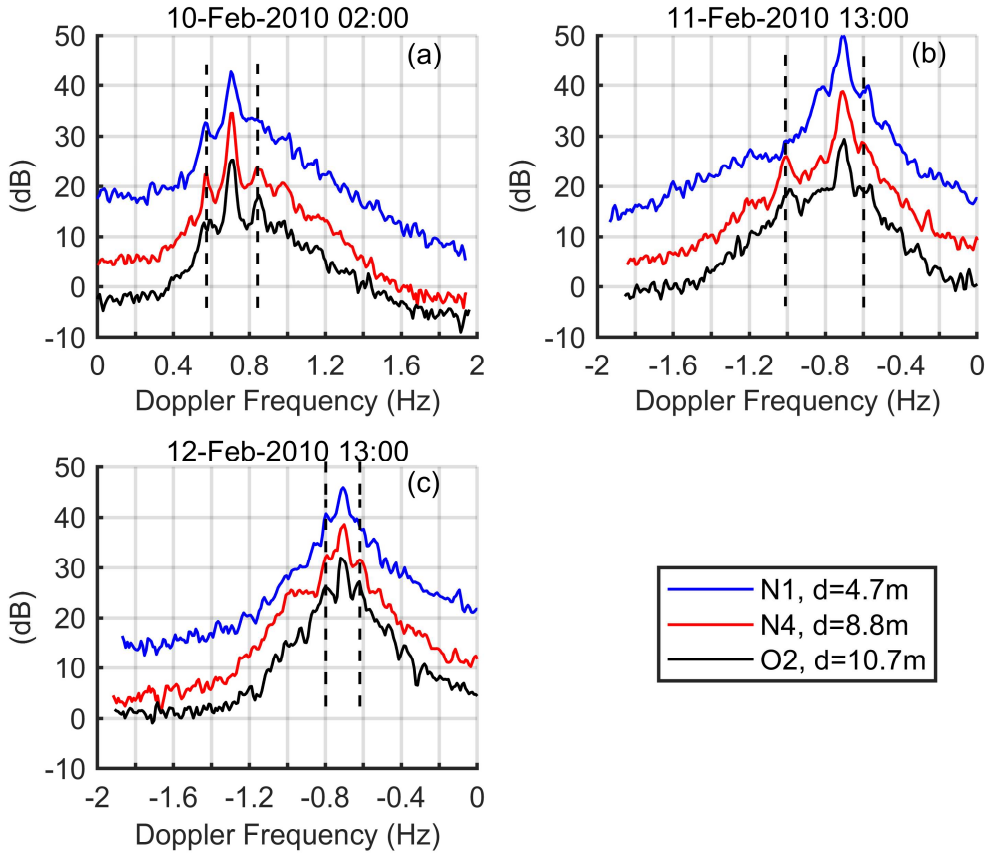

Figure 3.18: Doppler spectra from three stations (N1, N4, and O2) corresponding to different mean water depths (4.7, 8.8, and 10.7 m, respectively) for examples from three different times.

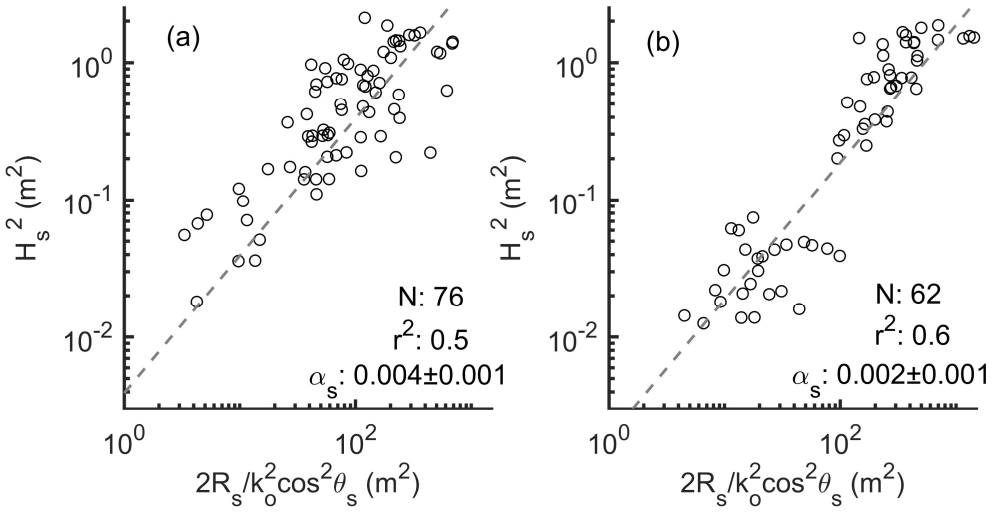

Figure 3.19: Regression analysis for the estimation of the swell calibration coefficient using the $\cos^2\theta_s$ model, where θ_s is the angle between swell propagation direction and radar beam direction for (a) site O2, and (b) site N4

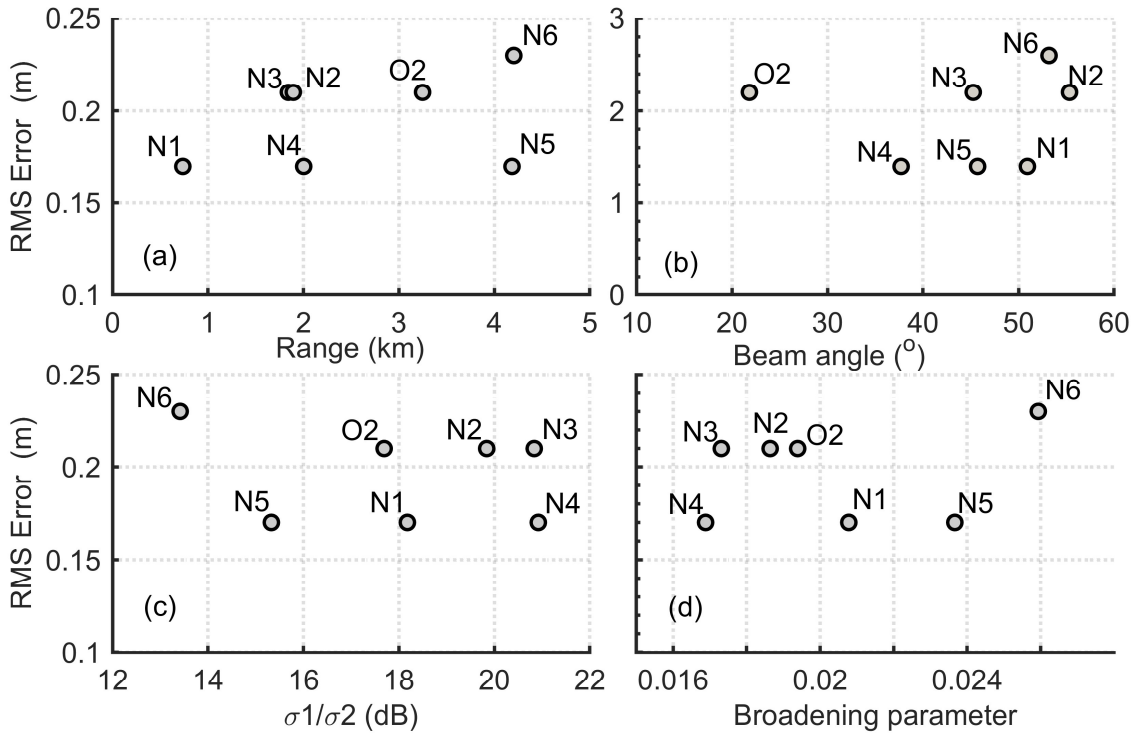

Figure 3.20: Scatter plots HF radar parameters and wave height RMS error at all sampling sites vs (a) range (km), (b) beam angle (degrees from boresight), (c) ratio of first- to second-order peak energies (dB), and (d) broadening parameter.

CHAPTER 4

EVALUATION AND VALIDATION OF HF RADAR SWELL AND WIND WAVE INVERSION METHOD[2]

[2] This chapter has been submitted as Alattabi, Zaid R., Voulgaris, G., and Conley, D., 2020. Evaluation and Validation of HF Radar Swell and Wind wave Inversion Method. *Journal of Atmospheric and Oceanic Technology*, JTECH-D-20-0186, submitted 11/16/2020.

Abstract

An examination of the applicability and accuracy of the empirical wave inversion method in the presence of swell waves is presented. The ability of the method to invert Doppler spectra to wave directional spectra and bulk wave parameters is investigated using one-month data from a 12 MHz WERA HF radar system and in situ data from wave buoy. Three different swell inversion models are evaluated: LPM (Lipa et al., 1981), WFG (Wang et al., 2016) and EMP, an empirical approach introduced in this study. The swell inversions were carried out using two different scenarios: (1) a single beam from a single radar site and two beams from a single radar site, and (2) two beams from two sites (a single beam per site) intersecting each other at the buoy location. The LPM method applied using two beams from two different sites, has been found to provide the best estimations of swell parameters (swell height RMS error 0.24m) and showed a good correlation with the partitioned swell in situ values. For the wind wave inversion, the empirical method presented here is used with an empirical coefficient of 0.3 which seems to be suitable for universal application for all radar operating frequencies. The inverted swell parameters are used to create a swell spectrum which is combined with the inverted wind wave spectrum inverted to create a full directional wave spectrum. The wave inversion method presented in this study although empirical does not require calibration with in situ data and can be applied to any beam forming system and operating frequency.

4.1 Introduction

Doppler energy spectra estimated from electromagnetic (EM) waves backscattered from the ocean surface (Crombie, 1955) contain information on both surface currents and ocean waves. The first order spectral peaks are due to backscatter by ocean waves with a wavelength half the EM wave wavelength; the shift from the theoretical Bragg frequency is used to estimate the ocean surface current along the direction of the beam (radial currents; e.g., Paduan and Rosenfeld, 1996). The spectral continuum present on either side of each first-order Bragg peak (second-order scattering), is the result of nonlinear interactions between the EM waves and a combination of ocean surface waves that satisfy the requirement that the sum of their wavenumber vectors equals that of the Bragg wave (i.e., Stewart, 1971; Hasselmann, 1971; Weber and Barrick, 1977). This continuum is referred to as the second-order sideband spectrum and it contains the signature of the ocean waves present at the surface of the ocean.

The relationship between ocean waves and HF radar Doppler spectra has been described theoretically in Barrick (1971) and Barrick and Weber (1977) and it has been utilized (Barrick, 1977b) to develop an inversion technique for estimating ocean waves from the Doppler spectrum. Lipa (1977) linearized Barrick's equations and used a stabilization technique to carry out the inversion of a theoretical wave spectrum. Subsequently, several other inversion methods were developed that included the application of singular value decomposition (SVD) techniques (i.e., Gill, 1990; Howell and Walsh, 1993; Zhang and Gill, 2006) for bistatic radar systems, the Chahine-Twomey relaxation method (Wyatt, 1990), or provided direct solutions of the nonlinear integral equations (Hisaki, 1996). However, the simpler empirical method of Barrick (1977a, b)

has been the basis for a number of wave inversions of HF radar Doppler spectra including those described in Maresca and George (1980) and Heron et al. (1985). Gurgel et al. (2006) extended the empirical algorithm to allow for the estimation of wave directional characteristics using the Doppler spectra from two phased array HF radars located at different locations along the coast. Lopez et al. (2016) evaluated the method of Gurgel et al. (2006) and noted that the empirical coefficients required by that method were different than those suggested by Gurgel et al. (2006) even after adjusting for differences in operating frequency.

Although these studies focused on wind wave inversion, discrepancies were found when swell waves were present (e.g., Lopez et al., 2016; Essen et al., 1999; Gurgel et al., 2006; Gomez et al., 2015; Wyatt, 1986, 2002, 1999; Heron and Prytz, 2002). Lipa and Barrick (1980) showed that the extraction of swell information from Doppler spectra is different from that developed for wind waves. Lopez et al. (2016) noted that the amplitude of the empirical calibration coefficients varied significantly at low wave frequencies (f<0.12 Hz) and this variability was dependent on the angle between the direction of swell propagation and radar beam (swell cross-angle). Higher values were estimated for cases when the swell cross-angle was close to 90^{o}, while the values were reduced for smaller swell cross-angles. Similar directional dependence was also reported earlier in Lipa and Barrick (1980) and wave inversions using both theoretical (Wyatt, 1999) and empirical (Gurgel et al., 2006) methods.

More recently, Alattabi et al. (2019) used a hybrid empirical inversion technique that combines Barrick's (1977) original wind-wave inversion method and a simplified swell inversion method to reconstruct the wave spectrum from a Very High Frequency

(VHF, 48MHz) radar system. In their study, it was shown that the regression coefficient for wind wave inversion was not wave frequency dependent as suggested by Gurgel et al. (2006) and Lopez et al. (2016); an almost constant value was proposed that was similar to that found in the studies of Ramos et al. (2009) and Heron and Heron (1998) who used different frequency radar systems. These findings suggested a universal application of the empirical inversion method that if true, makes in situ calibration redundant. However, in Alattabi et al. (2019) the swell inversion assumed of no directional dependence, mainly due to the short ranges and shallow water depths the data corresponded to. At such shallow depths, the swell crests are almost parallel to the coastline due to wave refraction and directional variability is minimal; these conditions allowed for the adoption of an empirically defined, non-directionally dependent coefficient for the estimation of swell wave height.

This study extends the hybrid empirical method of Alattabi et al. (2019) for swell conditions of variable directionality and tests its universality using a radar system of different frequency (12 MHz) than that used in the original study (48 MHz). The hypothesis is that if the empirical coefficient for the wind-wave inversion module is similar to that obtained using the 48 MHz system then the module is universally applicable. The extension of the model for variable swell conditions is carried out by evaluating the performance of the swell inversion methods of Lipa et al. (1981), Wang et al. (2016), and comparing it against an expanded form of the simplified parameterization used in Alattabi et al. (2019) that allows for swell directionality.

In this manuscript, section 4.2 describes briefly the theoretical swell inversion models presented elsewhere and presents the development of the expanded empirical

method of Alattabi et al. (2019) for swell and wind -wave (empirical) inversions. Section 4.3 presents the data used to evaluate the inversion models described in section 4.2, while the methodology used is described in section 4.4. Section 4.5 presents the swell inversion results, and in section 4.6 the findings are discussed in detail. Finally, the conclusions of the study are presented in section 4.7.

4.2 Inversion Models

4.2.1 Theoretical swell inversion model

Lipa and Barrick (1980) described in detail methods for extracting long (swell) wave information from second-order Doppler spectra derived from HF radars. Later, Lipa et al. (1981) evaluated these methods using sea-echo data from a narrow beam HF radar system on the Pacific Ocean. In their study, they used swell conditions of varying complexity including monochromatic, unidirectional, with a directional spread, and combination of two monochromatic swell systems. If a monochromatic swell (i.e., single direction and frequency (f_s)) is present, then four peaks appear on the Doppler spectrum at frequencies (f_{D_j}) given by:

$$f_{D_j} = m_1 \left(f_B^4 + f_s^4 + 2m_2 f_s^2 f_B^2 \cos\theta_s \right)^{\frac{1}{4}} + m_2 f_s \qquad (4.1)$$

where θ_s is the swell propagation direction with respect to the radar beam direction (i.e., swell cross angle). The index j (=1 to 4) defines the position of the peak within the region of the Doppler spectrum (from left to right), which in turn is defined by the parameters m_1 and m_2 (i.e., j=1, 2, 3 and 4 when (m_1, m_2) = (-1,-1), (-1,1), (1,-1), and (1,1), respectively, see Figure 4.1 for details).

Eq. (4.1) allows for the estimation of the swell cross-angle using:

$$\theta_s = \cos^{-1}[\frac{8f_B(\Delta f^+ - \Delta f^-)}{(\Delta f^+ + \Delta f^-)^2}] \tag{4.2}$$

where Δf is the frequency separation (distance) between the swell-induced Doppler peaks around the positive ($\Delta f^+ = f_{D4} - f_{D3}$) and negative ($\Delta f^- = f_{D2} - f_{D1}$) Bragg peaks (see Figure 4.1). Swell direction (θ_{sw}) is then estimated as $\theta_{sw} = \theta_r - \theta_s$, where θ_r is the radar beam direction. Similarly, the swell frequency is estimated as:

$$f_s = \frac{\Delta f^+ + \Delta f^-}{4} \tag{4.3}$$

and assuming deep water conditions the wavenumber is given by:

$$k_{so} = (2\pi)^2(\Delta f^+ + \Delta f^-)^2/16g \tag{4.4}$$

For any arbitrary depth h the swell wave number k_s is related to the deep-water wave number through (Phillips 1966):

$$k_s = k_{so}\, tanh(k_{so}h) \tag{4.5}$$

Based on Lipa and Barrick (1980) the root-mean-square (RMS) swell wave height can be obtained from each side of the Doppler spectrum using the ratio $\boldsymbol{\mathcal{R}}_j = \sigma_2(f_{Dj})/\sigma_1(f_{Bm_1})$, where $\sigma_2(f_{Dj})$ is the second-order Doppler spectral energy level corresponding to the swell peak and $\sigma_1(f_{Bm_1})$ is the adjacent first-order Bragg peak (i.e., m_1= -1 for j =1 or 2 and m_1= 1, for j =3 or 4, see Figure 4.1) so that:

$$H_{sw}^2 = \frac{\boldsymbol{\mathcal{R}}_j}{2\left|\Gamma_j(k_s, \theta_s)\right|^2 C_j} \tag{4.6}$$

$\Gamma_j(k_s, \theta_s)$ in Eq. (4.6) is the coupling coefficient that represents the hydrodynamic and electromagnetic interaction of the electromagnetic wave with the ocean waves at each region (defined by j) of the Doppler spectrum. C_j is a residual term related to the background wind wave field. Lipa et al. (1981) and Lipa and Barrick (1980) assumed $C_j = 1$ while Wang et al. (2016) using a Pierson-Moskowitz wave spectrum to describe the background wind waves suggested that C_j is approximated as:

$$C_j \approx (1 + (k_s/k_o)^2/4 + m_1 k_s cos\theta_s/k_o)^{-2} \tag{4.7}$$

where θ_s is the swell cross-angle, k_s is the swell wave number, and k_o is radar wave number. The value of $m_1 = \pm 1$ depends on the region of the Doppler spectrum the swell peak is located (i.e., m_1= -1 for j=1,2 and m_1=1 for j=3,4, see Figure 4.1).

The coupling coefficient $\Gamma_j(k_s, \theta_s)$ in Eq. (4.6) can be estimated (see Appendix A in Wang et al., 2016) for each region j of the Doppler spectrum and an arbitrary depth h as the sum of the electromagnetic

$$\Gamma_{EM} = \frac{1}{2}\left[\frac{(\overrightarrow{k_1}.\overrightarrow{k_o})(\overrightarrow{k_s}.\overrightarrow{k_o})/k_o^2 - 2\overrightarrow{k_1}.\overrightarrow{k_s}}{\sqrt{\overrightarrow{k_1}.\overrightarrow{k_s} - k_o\Delta}}\right] \tag{4.8}$$

and hydrodynamic

$$\begin{aligned}\Gamma_{H\,j} &= -\frac{i}{2}\left[k_1 + k_s - \frac{(k_1 k_s - \overrightarrow{k_1}.\overrightarrow{k_s})}{m_1 m_2\sqrt{k_1 k_s}}\left(\frac{f_{Dj}^2 + f_{Bj}^2}{{f_{Dj}}^2 - f_{Bj}^2}\right)\right. \\ &\left. + \frac{f_D\{(m_1\sqrt{gk_1})^3\, csch^2(k_1 d) + (m_2\sqrt{gk_s})^3\, csch^2(k_s h)\}}{g(f_{Dj}^2 - f_{Bj}^2)}\right]\end{aligned} \tag{4.9}$$

coefficients, where

$$\overrightarrow{k_1} + \overrightarrow{k_s} = -2\overrightarrow{k_o}$$

and $k_1, \overrightarrow{k_1}$ and $k_s, \overrightarrow{k_s}$ are the magnitude and vector of wind and swell waves, respectively. Δ denotes the normalized surface impedance of sea water (=0.011-0.012i) (Barrick, 1971).

Application of the model described by Eqs. (4.2) and (4.3) (hereafter referred to as LPM1) requires identification of all four swell peaks from both sides of a single Doppler spectrum. When only two swell peaks, from one side of the spectrum, are identifiable then two beams from two different radar sites (i.e., different cross-angles) can be used. Following Lipa et al. (1981), if the angle between the two beams is ϕ, then the Doppler frequencies corresponding to the swell peaks are given by:

$$f_D^{b_1}{}_j = m_1 \left(f_{Bj}^4 + f_s^4 + 2m_2 f_s^2 f_B^2 cos\theta_s \right)^{\frac{1}{4}} + m_2 f_s \qquad (4.10)$$

and

$$f_D^{b_2}{}_j = m_1 \left(f_{Bj}^4 + f_s^4 + 2m_2 f_s^2 f_B^2 \cos(\theta_s + \phi) \right)^{\frac{1}{4}} + m_2 f_s \qquad (4.11)$$

for beams b_1 and b_2, respectively. In this case the swell cross angle (θ_s) in Eqs. (4.10) and (4.11) is defined with reference to beam b_1.The normalized second-order energy at the corresponding swell peak and beam are:

$$R_j^{b_1} = 2 H_{sw}^2 \left| \Gamma_j^{b1}(k_s, \theta_s) \right|^2 \qquad (4.12)$$

$$R_j^{b_2} = 2\,H_{sw}^2\left|\Gamma_j^{b2}(k_s,\theta_s+\phi)\right|^2 \tag{4.13}$$

In this case, as Lipa et al. (1981) suggested, estimates of swell frequency (f_s) and cross-angle (θ_s) are obtained using Eqs. (4.10) and (4.11) through a least-square minimization method, while swell height (H_{sw}) and cross-angle (θ_s) are obtained using Eqs. (4.12) and (4.13).

The same approach [i.e., Eqs. (4.10-4.13)] could be implemented using two beams from a single radar site, as in Lipa et al. (1981). However, in the latter case the angle between the two beams should be at least two times greater than the beam width to ensure that the corresponding Doppler spectra are independent of each other and represent different patches of the ocean surface (Voulgaris et al., 2011). Hereafter, this method (i.e., use of 2 beams) is referred to as the LPM2$_i$ method, with the subscript *i* denoting the number of sites used (i.e., LPM2$_1$ denotes application using two beams from a single site while LPM2$_2$ indicates use of two beams from two different sites, for more details see section 4.4).

More recently Wang et al. (2016) presented a swell inversion method that also uses [Eqs. (4.2) and (4.3)] for estimating swell cross-angle and frequency, respectively. A least squares method is used to minimizes the difference (Q) between the theoretical $(\boldsymbol{\mathcal{R}}_j)$ and measured (R_j) swell peaks.

$$Q = \sum_{j=1:4}\left(\boldsymbol{\mathcal{R}}_j - R_j\right)^2 \tag{4.14}$$

and the RMS swell wave height is obtained by setting $\partial Q/\partial H_{sw} = 0$, so that:

$$H_{sw}^2 = \frac{4\sum_{j=1:4} R_j \left|\Gamma_j(k_s,\theta_s)\right|^2 C_j}{\sum_{j=1:4}\left|\Gamma_j(k_s,\theta_s)\right|^4 C_j^2} \tag{4.15}$$

The swell cross angle is estimated by substituting Eq. (4.15) into Eq. (4.6) for use in Eq. (4.14) which then becomes a function of the cross angle (θ_s) only. The latter is defined as the value for which $Q(\theta_s)$ is minimized.

The method of Wang et al. (2016) described above (hereafter referred to as the WFG1 method) requires information from both sides of the Doppler spectrum. In the case where only one side of the Doppler spectrum is available, the method can be modified for use with two beams (b_1 and b_2) obtained from two different radar systems or from two beams from a single site as described earlier. In this case:

$$H_{sw}^2 = \frac{4(\sum_j R_j^{b1}\left|\Gamma_j^{b1}(k_s,\theta_s)\right|^2 C_j^{b1} + \sum_j R_j^{b2}\left|\Gamma_j^{b2}(k_s,\theta_s+\phi)\right|^2 C_j^{b2}}{\sum_j\left|\Gamma_j^{b1}(k_s,\theta_s)\right|^4 C_j^{b1^2} + \sum_j\left|\Gamma_j^{b2}(k_s,\theta_s+\phi)\right|^4 C_j^{b2^2}} \tag{4.16}$$

where the superscripts b_1 and b_2 denote the two different beams (with b_1 being the reference beam) and ϕ is the angle between them. Swell direction and frequency are estimated using Eqs. (4.10) and (4.11) as in Lipa et al. (1981). The wave height is calculated using Eq. (4.16) and a second solution for swell direction is obtained as before by minimizing $Q(\theta_S)$. This method is referred to as the WFG2$_i$ method, with the subscript *i* denoting the source of the two beams (i.e., from a single or two different HF radar sites) as described earlier.

4.2.2 Empirical swell inversion model

The models described above (also see Lipa and Barrick, 1980 and Bathgate et al., 2006) indicate a strong relationship between swell height and the coupling coefficient;

the latter has a strong directional dependence which is shown to be related to $\cos^2$ of the swell cross-angle (θ_s) (see Appendix A in Lipa and Barrick, 1980). As an example, the magnitude of the coupling coefficient $|\Gamma|^2$ for a 0.083 Hz swell and a radar frequency of 12 MHz is shown in Figure 4.2. As Lipa and Barrick (1980) and Bathgate et al. (2006) have shown, this directional dependence leads to singularities at high swell cross-angles ($\approx 90°$) which makes swell inversion impossible (see Figure 4.2 at angles near $\pm 90°$).

In the empirical model of Alattabi et al. (2019) this directional dependence was not considered and an empirically defined coefficient α_s was used to estimate the swell wave height so that:

$$H_{sw}^2 = \alpha_s \frac{2\,R_s}{k_o^2} \tag{4.17}$$

where $R_s = \sum_j R_j;\ j$ denotes the number of swell peaks identified (2 or 4 depending on the quality of the Doppler spectra), and k_o is the radar wave number. This assumption of no directional dependence was justified by the very shallow water depths (~5-10 m) that ensured an almost constant swell angle of approach due to wave refraction (see Alattabi et al., 2019).

If we relax this assumption, then swell direction estimations can be obtained using Eqs. (4.10) and (4.11) presented earlier. Alternatively, the method of Gurgel et al. (2006) can be utilized. This empirical method assumes a direct relationship of the swell wave directional distribution function $F(\varphi)$ to the ratio of swell peaks around the dominant Bragg peak $\gamma_s = \sigma_2(f_3)/\sigma_2(f_1)$ or $\sigma_2(f_4)/\sigma_2(f_2)$ or $(\sigma_2(f_3) + \sigma_2(f_4))/(\sigma_2(f_1) + \sigma_2(f_2))$, for the positive and negative Doppler frequencies of the spectrum. The inverted

swell cross-angle direction is then estimated using the ratio from beam 1 (γ_s^{b1}) and beam 2 (γ_s^{b2}) by minimizing the following function:

$$Q = \left[\gamma_s^{b1} - \frac{F(\varphi - \theta_{r1})}{F(\varphi - \theta_{r1} + \pi)}\right]^2 + \left[\gamma_s^{b2} - \frac{F(\varphi - \theta_{r2})}{F(\varphi - \theta_{r2} + \pi)}\right]^2 \qquad (4.18)$$

where F $(= \cos^n(\cdot))$ is the directional distribution function used; θ_{r1} and θ_{r2} are the beam angles from beams (or sites) 1 and 2. The value of φ that minimizes the function Q is considered to correspond to the inverted swell direction θ_{sw}. Once swell direction is estimated using Eq. (4.18) the simple swell model of Alattabi et al. (2019) can be expanded to allow for changes in swell wave cross-angle. This modification makes the empirical coefficient shown in Eq. (4.17) to be swell cross-angle dependent. When averaging all coupling coefficients corresponding to the individual second-order swell peaks, the variation of the mean of $|\Gamma|^2$ (see Figure 4.2, right panel) can be empirically expressed as:

$$\overline{\Gamma}_j(k_s, \theta_s) = \overline{A}_j(k_s)\ \cos^n(\theta_s) \qquad (4.19)$$

where the overbar denotes averaged values and A_j is the maximum value for each coupling coefficient j. Based on Eq. (4.19) the empirical coefficient α_s in Eq. (4.17) can be substituted by $\alpha_s/\cos^n(\theta_s)$ so that:

$$H_{sw}^2 = \frac{2\alpha_s}{k_o^2 \cos^n \theta_s} \sum_j R_j \qquad (4.20)$$

where $\alpha_s = 1/\overline{A}_j(k_s)$, and the value of n (see Figure 4.2) depends on the Doppler spectrum side used (see Figure 4.2 right panel). A theoretical examination of A_j and n for a large range of radar frequencies (4-48 MHz) and swell wavelengths (see Figure 4.3)

showed limited variability/dependence on radar frequency or swell wavelength (for radar frequencies > 8MHz) independently of the sides of the spectrum considered (i.e., negative (A_{12}, n_{12}), positive (A_{34}, n_{34}) or both sides (A_{1234}, n_{1234})). At lower operating frequencies (<8MHz) significant variability is shown when swell waves with very short wavelengths (λ_{sw}<200m) are present something that might limit the applicability of this method at such conditions.

When both sides of the Doppler spectrum are used (i.e., j=1,2,3,4) then n=2.02, α_s= 1.18 and the method is denoted as EMP1 (see Figure 4.3a-b). When only one side is available (i.e., j=1,2 or j=3,4) two beams from two radars (EMP2$_2$) or a single site (EMP2$_1$) can be used. In this case equation (20) can be written as:

$$H_{sw}^2 = \frac{2\alpha_s}{k_o^2 cos^n(\theta_s)} \sum_{j=1,2/3,4} R_j^{b1} \tag{4.21}$$

$$H_{sw}^2 = \frac{2\alpha_s}{k_o^2 cos^n(\theta_s + \phi)} \sum_{j=1,2/3,4} R_j^{b2} \tag{4.22}$$

where $n = 2.25$ and α_s = 0.98 for $j = 1,2$ (see Figure 4.3c-d) and n =2.10 and α_s = 1.45 for $j = 3,4$ (see Figure 4.3e-f). As before, b_1 and b_2 denote the two beams and the swell cross angle (θ_s) is measured from beam b_1. The average value of H_{sw}^2 from Eqs. (4.21) and (4.22) is used to estimate swell wave height, while the swell frequency using EMP2$_2$ and EMP2$_1$ is estimated as:

$$f_s = \frac{(\Delta f_{b1}{}^-)_{j=1,2} + (\Delta f_{b2}{}^+)_{j=3,4}}{4} \quad or \quad \frac{(\Delta f_{b1}{}^+)_{j=3,4} + (\Delta f_{b2}{}^-)_{j=1,2}}{4} \tag{4.23}$$

4.2.3 Wind wave inversion model

The empirical wind wave inversion method used in Alattabi et al. (2019) is based on Barrick's (1977b) model and relies on the relationship between the ocean wind-wave spectra $S_{ww}(f)$ and the normalized, weighted second-order spectra referred to as $R_W(f)$:

$$S_{ww}(f) = \alpha_w \frac{2R_W(f)}{k_o^2} \tag{4.24}$$

where α_w is the wind wave coefficient, which was found to be relatively constant for all wave frequencies (Alattabi et al., 2019), k_o is the radar wave number, and $R_W(f)$ is defined by Barrick (1977a, b) as:

$$R_W(f_D) = \frac{\sigma_2(f_D)/W(f_D/f_B)}{\sigma_1(f_D)df_D} \tag{4.25}$$

where $\sigma_1$and σ_2 are the first- and second-order spectral energies, W is Barrick's weighting function, and f_D and f_B are Doppler and Bragg frequencies. The inverted ocean wave frequency f is determined by $f = |f_D - f_B|$.

4.2.4 Wind and wave direction

The swell direction estimation method using the empirical method [see section 4.2.2, Eq. (4.18)] is adopted for the estimation of wind direction using the ratio of Bragg peak energies (Long and Trizna, 1973; Stewart and Barnum, 1975; Heron and Rose, 1986; Fernandez et al., 1997):

$$\zeta = \frac{\sigma_1^+}{\sigma_1^-} \tag{4.26}$$

where $\sigma_1^+$and σ_1^- are the integral of first-order spectra (the Bragg peak energies) corresponding to the approaching (+) and receding (-) Bragg waves, respectively. Then, the inverted wind direction is estimated as:

$$\theta_r = \theta_r \pm 2\, arctan\left(\zeta^{\frac{1}{s}}\right) \tag{4.27}$$

where the $\pm$ sign denotes the ambiguity for direction for single radar, which can be resolved using Eq. (4.18) and two beams from two radar sites pointing at the same location in the ocean. s is the wave directional spreading factor ($s = 2,$ as in Gurgel et al. (2006) and Fernandez et al. (1997)).

The direction of wind-waves can be estimated from the second-order continuum as in Alattabi et al. (2019) using the ocean wave frequency dependent ratio $\gamma(f)$ of second-order Doppler spectrum energies corresponding to the approaching (positive Doppler frequencies) and receding (negative Doppler frequencies) sides of the second-order sidebands around the dominant Bragg peak ($\sigma_2^{+1,m_2}/\sigma_2^{-1,m_2}$), where $m_2 = \pm 1$ (see Figure 4.1). This ratio is defined as:

$$\gamma(f) = \frac{\sigma_2^{+1}(f)}{\sigma_2^{-1}(f)} \tag{4.28}$$

and the second-order sidebands around the positive and negative Bragg peaks are defined based on the data quality criteria (see section 4.4) as follows,

$$\sigma_2^i(f) =$$

$$\begin{cases} \sigma_2^{i,-1}(f) + \sigma_2^{i,+1}(f) & when\ both\ left\ and\ right\ continua\ are\ available \\ \sigma_2^{i,-1}(f) & when\ only\ the\ continuum\ to\ the\ left\ \ is\ available \\ \sigma_2^{i,+1}(f) & when\ only\ the\ continuum\ to\ the\ right\ \ is\ available \end{cases}$$

Where $i = +1$ and -1 correspond to second-order sidebands around the positive and negative Bragg peak, respectively. The inverted wave direction is estimated using:

$$\theta(f)_{inv} = \theta_r \pm 2\, arctan\left(\gamma(f)^{\frac{1}{s}}\right) \tag{4.29}$$

where $\theta(f)_{inv}$ is the direction of ocean waves with frequency f, θ_r denotes radial beam direction, and s is the wave directional spreading factor as in Eq. (4.27). In a similar manner for the case of wind direction, the ambiguity in the solution of Eq. (4.29) can be resolved using two radar sites with Eq. (4.18) or using additional information.

4.2.5 Directional frequency wind-wave spectrum model

The directional wave spectrum $S(f, \theta)$ can be expressed in terms of one-dimensional wave spectrum $S(f)$ and the directional spreading function $D(f, \theta)$ (Longuet-Higgins et al., 1963) as:

$$S(f, \theta) = S(f)D(f, \theta) \tag{4.30}$$

where f is wave frequency and θ is wave direction in radians. Longuet-Higgins et al. (1963), suggested a cos^{2s} based $D(f, \theta)$ with s being the spreading parameter which depends on the ratios f/f_p and U_{10}/c_p (Hasselmann et al., 1980). However, this dependence on wind speed makes the application of the model for HF radar inversion

more complicated. Donelan's et al. (1985) directional distribution model is more convenient as it does not depend on wind speed and utilizes a $sech^2$ function:

$$D(f,\theta) = 0.5\beta sech^2\,\beta(\theta - \theta(f)) \tag{4.31}$$

where β depends on the ratio of f/f_p only, so that:

$$\beta = \begin{cases} 2.61(f/f_p)^{1.3} & 0.56 < f/f_p < 0.95 \\ 2.28(f/f_p)^{-1.3} & 0.95 < f/f_p < 1.60 \\ 1.24 & f/f_p \geq 1.60 \text{ or } f/f_p \leq 0.56 \end{cases} \tag{4.32}$$

This distribution is adopted in this study to define the directional characteristics of the inverted wave frequency spectrum.

4.3 Data Availability

Data from two HF radar systems and a wave buoy deployed off the north coast of Cornwall (UK) are used in this study. Information on wind speed and direction were obtained from a meteorological station located on the coastline at Perranporth (see Figure 4.4) while the closest tide gauge (station ID 202, British Oceanographic Data Centre) was located on Newlyn. The dataset used in this study covers the period March 30th to April 27th, 2012 and includes simultaneously collected Doppler spectra from the two HF radars and in situ spectral wave data from the buoy.

4.3.1 HF Radar

The HF radar data were collected by two 16 element, beam-forming HF radar systems (WERA), deployed on the northern coast of Cornwall (UK) and operated by the University of Plymouth. The HF radar units were located at Pendeen (PEN) and Perranporth (PER), some 40 km away from each other (Figure 4.3) and their boresights

were 23ºN and 305ºN, respectively (see Figure 4.4). The radars operated at a central transmitting frequency of 12 MHz with a bandwidth of 150 KHz, resulting to a range resolution of 1 km. Data collection was once per hour with a transmission duration of approximately 18 min. A total of 694 transmissions were available for analysis covering the 29-day data collection period used in this study. The Doppler spectra have a frequency resolution of 0.0075 Hz and cover the range -1.915 to 1.922 Hz (defined by the chirp-rate of 3.85 Hz used during transmission). The Doppler spectral energy is expressed in decibels (dB) defined using a system internal reference level. Doppler spectra estimations are based on FFT analysis performed on 512 point-segments with 75% overlap. For this analysis, Doppler spectra for different beams and sites are utilized depending on the model used for the swell inversion. More details about the HF radar systems and their configurations can be found in Lopez et al. (2016) and Lopez and Conley (2019).

4.3.2 In situ wave data

In situ wave data were collected using a Seawatch Mini II directional wave buoy deployed at a mean water depth of 50m at ranges 20 and 30 km from the PEN and PER HF radar sites, respectively (see Figure 4.4). Directional wave spectra estimates were provided every 30 min and the frequency and azimuthal resolution of the spectra are 0.0078 Hz, and 4°, respectively. Although wave spectra cover the frequency range 0.046 - 0.50 Hz, the analysis was restricted to 0.35 Hz as this corresponds to the maximum ocean wave frequency resolved by the HF radar-derived Doppler spectra.

RMS wave height, peak and mean wave frequencies and directions were estimated from the directional spectra using the moments method (Herbers et al., 1999).

Swell and wind wave bulk wave parameters were estimated by partitioning the spectra using a watershed defining algorithm as implemented by Cahl and Voulgaris (2019).

4.4 Methodology

Prior to analysis, the noise level of the Doppler spectrum is estimated using the method described in Hildebrand and Sekhon (1974) and then subtracted from the spectra. The energy levels for the first and second-order regions of the de-noised Doppler spectra (σ_1 and σ_2, respectively) are used to check spectra suitability for inversion and to avoid cases where the first and second-order spectra are merged. The values of the above data quality control criteria suggested by Alattabi et al. (2019), although suitable for the 48 MHz VHF radar used in their study, were found to be very restrictive in this case (12 MHz) qualifying only a small percentage of the data (~20%) for inversion. After trial and error, it was concluded that the best quality criteria were: (i) first-order Bragg peaks and second-order sideband energy levels (σ_1 and σ_2) greater than 10 and 5 dB, respectively, and (ii) the energy of the Bragg peak should be at least 2 dB higher than the mean energy of the 1/3 highest second-order peaks present in the Doppler spectrum.

The inverted spectral frequencies are limited by the lower frequency limit of the second-order sidebands which for this data set corresponds to a lower wave frequency (f_{min}) of 0.046 Hz (Doppler frequency = ±Brag frequency ± 0.046 Hz); frequencies lower than that value are often contaminated by energy from the first-order signal. The full extent of the latter was delineated by identifying the maximum value of the Bragg peak and fitting a Gaussian curve around it using 2 points of either side of it. The upper limit of the Doppler spectra is limited to a maximum ocean wave frequency of 0.35 Hz which corresponds roughly to the distance (in Hz) of the first-order Bragg peak from the

zero Doppler frequency. Although some studies utilizing a 12 MHz system have used the range 0.05-0.25 Hz with a resolution of 0.01Hz (e.g., Wyatt, 2005, 2017; Lopez et al., 2016; Lopez and Conley, 2019), Gurgel et al. (2006) has argued that the upper limit can be safely extended up to 0.35 Hz as done in this study.

The swell region is defined as the area around the dominant Bragg peak that corresponds to ocean wave frequency range f_{min} to f_c, where f_c is the swell/wind separation frequency. The latter is determined using the wave age formulation (Hanson and Philips, 2001) that relates wind speed to peak wind wave frequency

$$f_c = \frac{g}{2\pi}\left(\frac{1}{TU_{10}}\right) \tag{4.33}$$

where T is an empirical factor and U_{10} is the wind speed at 10m above sea level. Although T has been found to range from 1.25 to 1.9 (Gilhousen and Hervey, 2001; Hanson and Philips, 2001; Chen et al., 2015; Hessner and Hanson, 2010; Bidlot, 2001; Tracy et al., 2007; De Farias et al., 2012; Churchill et al., 2006; Earl, 1984; Quentin, 2002), $T = 1.5$ is adopted here as it is the most commonly used value (Hanson and Philips, 2001; Chen et al., 2015; Hessner and Hanson, 2010). In addition, the maximum swell separation frequency obtained using Eq. (4.33) is not allowed to exceed 0.12 Hz.

Once the swell region has been defined, the peak swell Doppler frequency f_{Dj} is estimated using the weighted mean of the largest peak identified (f_{Dm}) within this region and 2 points on either side of it:

$$f_{Dj} = \frac{\sum_{i=-2:2} \sigma_2 (f_{D\,m+i})^5 f_{D\,m+i}}{\sum_{i=-2:2} \sigma_2 (f_{D\,m+i})^5} \qquad f_{min} < f_{D\,m+i} < f_{Dc} \tag{4.34}$$

where $f_{D\,m+i}$ is the discrete Doppler frequency where a Doppler estimate is available and f_{Dc} is the swell-wind separation frequency expressed as Doppler frequency (i.e., $f_c = |f_{Dc} - f_B|$). The measured swell peak ratio R_j is then defined as:

$$R_j = \frac{\int_{f_{Dm-2}}^{f_{Dm+2}} \sigma_2(f_D) df_D}{\int_{f_B-\Delta f}^{f_B+\Delta f} \sigma_1(f_D) df_D} \tag{4.35}$$

where df_D is the resolution of the Doppler spectrum. For Bragg peaks, Δf is defined as the half-power frequency width of Bragg peaks obtained after fitting a Gaussian curve around the Bragg peak. The range to the buoy site, as well as the angle between the beam-forming direction and the radar boresight used for the evaluation of the swell models (see Figure 4.4), are listed in Table 1. For one site / one beam analysis, the swell models LPM1, WFG1 and EMP1 are utilized using the radar beam data (b_{PENo} and b_{PERo}) pointing directly to the buoy location (see dashed black lines in Figure 4.4). The same beams (b_{PENo} and b_{PERo}) are used when the two sites / two beams methods (i.e., $LPM2_2$, $WFG2_2$ and $EMP2_2$) are utilized. For one site / two beams analysis (i.e., $LPM2_1$, $WFG2_1$ and $EMP2_1$) data from two beams from a single radar site (b_{PEN1} and b_{PEN2} for PEN site, and b_{PER1} and b_{PER2} for PER site), directed 15° on either side of the buoy location are used. These are schematically shown as red and blue dashed lines in Figure 4.4, for PEN and PER sites, respectively.

4.5 Results

4.5.1 Wave and wind conditions

The recorded in situ wind and wave conditions for the period March 30 to April 17, 2012 used in this study are shown as time series in Figure 4.5. The total RMS wave

height ranged from 0.23 to 5.0 m while peak wave frequency ranged from 0.034 to 0.30 Hz. The partitioned wind-wave and swell parameters are shown in Figure 4.5b-e. The swells present travel across the North Atlantic either from the west or south west and their RMS wave heights ranged from 0.1 to 2.1m (see Figure 4.5b, e).

During the experimental period, several wind wave and swell events are identified, but for model verification, only events for which swell was present and the radar-derived Doppler spectra passed the quality criteria (i.e., σ_1>10 dB and σ_2> 5 dB and σ_1/σ_2 > 2) are analyzed. Specific events (A-H) are identified that correspond to periods when swell (A, B, G and H) or wind waves (C, D, E and F) are the dominant sources of energy. Wave conditions for each event and their directional characteristics with regards to the radar beams from each station are listed in Table 4.2. During events A and B light swell waves with height ~0.5m propagating mostly from the west (mean swell direction ~95° N) were prominent. Events G and H represent strong swell activity (swell height up to 1.3m) with mean directions 53° and 81°N respectively. Overall swells events A and B cross the PEN radar beam at the buoy location at high (>80°), cross-angles while the cross-angles for events G and B are smaller (41° and 69°, respectively). The same swell trains cross the PER beam at very small angles of 2° and 5° for events A and B, respectively. A moderate cross angle (38°) was recorded for PER site at event G.

4.5.2 HF Radar Doppler and In situ Wave Spectra

Time-stacks of Doppler spectra corresponding to the buoy location and for the whole period of data availability are shown in Figure 4.6a-b for both radar sites. The Doppler Bragg (first-order) peaks are modulated by the tidally-induced surface currents while the energy of the second-order continua is visible around the first-order peaks. It is

worth noting that the second-order regions are significantly narrower for PER (Figure 4.6a) than for PEN (Figure 4.6b). Similarly, a time-stack of the in situ wave spectra is shown in Figure 4.6c. The specific swell and wind-wave events (A-H) are also identified in the figure while the detailed wave directional spectra for each individual event are shown against the corresponding Doppler spectra in Figure 4.7. In the same figure, the partitioned regions of the spectra derived using the method of Cahl and Voulgaris (2019) are shown using yellow and light blue shading for swell and wind waves, respectively.

4.5.3 Swell wave inversion

In this section, the results for the swell inversion are presented and include inversions using: 1) a single beam from a single radar site ($LPM1_1$, $WFG1_1$, $EMP1_1$), 2) two beams from a single radar site ($LPM2_1$, $WFG2_1$, $EMP2_1$), and 3) two beams from two sites (a single beam per site) intersecting each other at the buoy location ($LPM2_2$, $WFG2_2$, $EMP2_2$). Only Doppler spectra that passed the data quality control (see section 4.4) are used for the inversion. Data that passed the data quality control but no swell peaks were present were also excluded from the analysis. The lack of swell peaks can be attributed to no swell being present in the ocean or not being detected in the Doppler spectrum.

Analysis of the buoy data revealed that swell was present 95% of the time (658 data points), but swell with energy density above a minimum energy level defined as 0.15 m^2/Hz^{-1} represents 78% of the total (i.e., 544 data points). The times where the Doppler spectra passed the quality criteria and swell peaks were identified are shown in Figure 4.8 together with in situ swell percentage of data availability and in situ swell data with energy level above 0.15 m^2 Hz^{-1}. The labels on the y-axis scale denote the side of

Doppler spectrum that swell peaks are identified (i.e., (-) and (+) denote the negative and positive sides of the Doppler spectrum, respectively while (±) denotes both sides (i.e., 4 peaks)).

4.5.3.1 Inversion for swell frequency

A) Single site

One site – one beam

Inversion for swell frequency with this method requires four swell peaks are detected on a single Doppler spectrum and it is identical for all three swell inversion models ($LPM1_1$, $WFG1_1$, $EMP1_1$) [see Eq. (4.3) and Table 4.3]. Doppler spectra from beams b_{PERo} and b_{PENo} are used here and the inversion was carried out on Doppler spectra that passed the QA criteria and swell peaks were successfully identified. These represent 48% and 60% of the record with swell detected in the in situ data for PEN and PER, respectively.

Higher data availability (78%) is obtained when we count the times that spectra from one or both sites passed the criteria for successful inversion for swell frequency (see Table 4.3, "combined"). The inverted swell frequencies are compared to the in situ data in the scatter plot shown in Figure 4.9a1 and the statistics of the comparison are listed in Table 4.3. The correlation coefficients are 0.40 and 0.59 for PEN and PER, respectively while the RMS error is 0.01 Hz. Using the inversions from the periods when data from both stations ("common" in Table 3) were usable (30% of the data,) the correlation coefficient was similar to that for PER.

One site – two beams

When two beams from a single site (b_{PEN1} and b_{PEN2} from PEN and b_{PER1} and b_{PEN2} from PER, see Figure 4.4) are used, the two swell peaks identified on the dominant side of each beam's Doppler spectra are utilized [see Eqs. (4.10) and (4.11) for both $LPM2_1$ and $WFG2_1$, and Eq. (4.23) for $EPM2_1$]; these could be on either positive or negative sides of the spectra. The Doppler spectra that passed the QA criteria and swell peaks were successfully identified for this method to be applied were 74% and 69% of the record with swell present for PEN and PER, respectively. Combining the records from both sites increases the percentage to 93%. The times both stations had spectra suitable for inversion (common) represent only 50% of the swell record.

The results of this inversion are compared with the in situ derived swell frequencies in the scatter plot shown in Figure 4.9a_2, and 9b_2 for $LPM2_1$/$WFG2_1$ and $EPM2_1$, respectively. The statistics of the comparison (Table 4.3) indicate that although the RMS error for the $LPM2_1$/$WFG2_1$ method is the same (0.01Hz) the estimations using spectra from PER exhibit less variability (r=0.60) than those from PEN (r=0.31). $EPM2_1$ [see Eq. (4.23)] estimates show similar variability for both radar sites ($r \sim 0.62$). As expected, the variability of the common and combined inversions, as expressed though the value of the correlation coefficient varies as a function of the number of points used from each site and the r values of the individual sites (r = 0.31 and 0.60 for PEN and PER, respectively).

B) Two sites

When two sites are used, the same Eqs. (4.10), (4.11) and (4.23), as before, are utilized for $LPM2_2$ and $EMP2_2$, respectively. The only difference is that the beams b_{PERo} and b_{PENo} aiming directly at the in situ buoy are utilized (see Figure 4.4) in this case. The Doppler spectra available for this method represent 67% and 51% for the of the record with swell present for $LPM2_2$ and $EMP2_2$, respectively. The comparison of the inverted and in situ swell frequency values is shown in Figure $4.9a_3$ in the form of a scatter plot and in Table 4.3. The swell frequency inversions using these methods show a relatively higher correlation coefficient (>0.60) than those derived using the one site-one beam, and one site-two beam methods (see previous section). These findings are consistent for both $LPM2_2$ and $EPM2_2$ methods (see Figure $4.9a_3$, b_3). It should be noted that the WFG method uses the same equations as the LPM method to estimate the frequency of the swell, so the results are identical and not shown here.

4.5.3.2 inversion for swell direction

A) Single site

One site – one beam

When four swell peaks are detectable in an individual Doppler spectrum from a single beam, the direction of the swell is obtained using Eq. (4.2) (LMP1/ WFG1 methods) or Eq. (4.18) (EMP1 method). The direction values derived using these methods are plotted against the swell directions from the buoy data obtained after partitioning the directional spectra (see Figures $4.10a_1$, and $4.b_1$). The corresponding

statistics are listed in Table 4.4. It is worth noting that only a very limited fraction of the record with swell present (21% to 28%) allowed for the detection of four swell peaks. Even when the data from two sites are combined, the amount of inversions represents only 41% of the total record.

One site – two beams

When two beams from a single site are used (Eqs. (4.10-4.13) for $LPM2_1$/ $WFG2_1$ and Eq. (4.18) for $EMP2_1$) the inversion results show significant scatter (see Figure $4.10a_2$, b_2, and Table 4.4). The percentage of inverted data from $LPM2_1$ is 25% and 32% for the PER and PEN sites, respectively. A similar percentage is obtained when $EMP2_1$ is used on PER, but the rate of inverted data falls to 8% for the PEN site. When data from both sites are combined the amount of inverted data increases to 45%.

B) Two sites

The same equations used in the previous scenario are used in both $LPM2_2$/ $WFG2_2$ and $EMP2_2$ methods that utilize two beams from two different sites. The results are shown in Figure $4.10a_3$, b_3. It seems both methods provide fair estimates of swell direction in this case. $LPM2_2$ shows good agreement with the in situ data which is better than that identified when using $LPM2_1$ with a complex correlation coefficient with magnitude of ~0.53 and angle of 20º (see Table 4.4). $EMP2_2$ method shows a lower correlation (r = 0.37) than $LPM2_2$.

The WFG method for swell direction is the same as that for the LPM method and as such the same statistics are valid. The statistical results shown in Table 4 are obtained without considering the flagged data (shaded range in Figure 4.10) because the latter do

not have corresponding inverted swell wave heights. The latter is required to determine the complex correlation coefficient so only data with inverted swell cross angles <75° (see section 4.5.3.3 below) are used.

4.5.3.3 Inversion for swell wave height

As discussed in section 4.2 and described in Lipa et al. (1981), singularities at high swell cross-angles (~90°, see Figure 4.2) do not allow the inversion for swell. A synthetic data analysis (not shown here) using different radar frequencies (4, 12, and 48 MHz), and swell periods varying from 8s to 25s, revealed that the range of swell cross angles that leads to singularities in the coupling coefficient depends on radar operating frequency. For radar frequencies of 4, 12, and 48 MHz singularities occur for swell cross angles $|\theta_s| > 60^o, 75^o$ and 85^o, respectively. A crude, empirical fitting suggests that singularities would occur when $|\theta_s| > 23\log_{10}(f_{radar}) + 48$, where f_{radar} is the radar operating frequency in MHz. In this manuscript, inverted swell cross-angle $|\theta_s|$ above the value of 75 degrees are flagged (see previous section, shaded areas in Figure 4.10) and not used for swell wave height inversion.

Inverted RMS swell wave heights estimates using all three methods (LPM, WFG, and EMP) and for the different combinations of sites and beams, as described in sections 4.2.1 and 4.2.2 are examined in this section. The cross-angle limitation leads to swell height inversions from a smaller number of records than those reported for swell direction inversion.

A) One site

One site – one beam

Inverted swell wave height using the LPM1 [Eq. (4.6)], WFG1 [Eq. (4.15)], and EMP1 [Eq. (4.20)] methods are shown in Figures 4.11a_1, b_1, and c_1, respectively. The percentage of successful inversions was very low (21%, for LPM1 and WFG1 and 18% for EMP1) for PEN and the errors in swell height were 0.94m, 0.63m and 0.66m, respectively. The low rate of inverted data is due to the lack of detectable swell peaks in the swell region of the Doppler spectra. Some of these cases represent weak in situ swell signals (i.e., energy < 0.76 m^2/Hz that corresponds to RMS swell wave height 0.21m) that is not detectable by the radar. Similar low recoveries were experienced in applying the inversion Doppler spectra from PER (28%) with the errors being of similar value as those for PEN (see Table 4.5). The errors are significantly smaller (0.60m, 0.38m, and 0.42m, respectively) when averaging the estimates from both stations (see common in Table 4.5) but in this case the inversion is limited to only 9% to 18% of the record.

One site – two beams

The comparisons of inverted and in situ swell heights for all three methods that use two beams from a single site (LPM2_1, WFG2_1, and EMP2_1) are presented as scatter plots in Figure 4.11 and the statistics are listed in Table 4.5. The results clearly indicate that EMP2_1 provides the least favorable agreement (RMS error > 0.80m) as there is a large scatter between inverted and in situ values (see Figure 4.11c_2). In addition, it appears to overestimate swell heights (regression line slopes > 1, see Figure 4.11c_2 and Table 4.5). The other two methods (LPM2_1 and WFG2_1) perform slightly better in terms

of RMS errors, although the slope of the regression line suggests underestimation of wave heights; $WFG2_1$ seems to perform best for data from PEN (see Figure $4.11b_2$) while $LPM2_1$ appears to performs better for data from PER (see Figure $4.11a_2$).

B) Two sites

Using 2 beams from two different sites (i.e., methods $LPM2_2$, $WFG2_2$, and $EMP2_2$) seems to provide better agreement with the in situ data (see Table 4.5) than those shown in the previous section (2 beams from a single site). This is the case even when comparing the results against the "combined" $LPM2_1$, $WFG2_1$ and $EMP2_1$ methods that incorporate the estimates from both radar sites. The RMS errors estimated are 0.24m,0.39m, and 0.37 m for $LPM2_2$, $WFG2_2$ and $EMP2_2$, respectively, with the $LPM2_2$ derived data showing the highest correlation coefficient (r=0.85) and a regression slope of 0.87 (see Table 4.5). The data inverted using these methods represent 47% and 27% of the record when swell was present for $LPM2_2$/$WFG2_2$, and $EMP2_2$, respectively (see Table 4.5).

4.5.4 wind-wave spectrum inversion

In this section, the results from applying the Alattabi et al. (2019) wind wave inversion module (Eq. (4.24)) are presented. Alattabi et al. (2019) suggested that Eq. (4.24) might have universal applicability with a regression coefficient of the value of $\alpha_w = 0.255 \pm 0.015$. This is first verified with the data from this study using the 12 MHz HF radar systems.

Following Alattabi et al. (2019) the dependence of the calibration coefficient on wind wave frequency is examined using the wind wave part of the radar Doppler spectral

estimates and the in situ wave spectra with energy above the spectral noise floor which is assumed to be 0.15 m^2 Hz^{-1}. The latter was defined after an examination of the in situ wave spectra. The data quality criteria (i.e., energy levels for first σ_1 and second-order peaks must be greater than 10 dB and 5 dB, respectively, and first-order energy at least 2dB higher than the mean of the 1/3 highest second-order peaks, see section 4.4) are used for selecting the Doppler spectra to determine the coefficient required to invert for wind waves. The normalized weighted second-order spectral data ($R_W(f)$) were estimated from both radar sites (PEN and PER) using Doppler spectra corresponding to the buoy location and they are shown in Figure 4.12 in the form of time-stack diagrams. The estimated $R_W(f)$ values correspond to discreet frequency bands that span the range of frequencies from the swell cut-off (f_c, see black line in Figure 4.12) to 0.35 Hz. These were interpolated to match the frequency bands corresponding to the in situ wave spectra $S(f)$ estimates, which are limited to f_c and 0.35 Hz. Calibration coefficients $\alpha(f)$ were estimated for each wave frequency (f), as in Alattabi et al. (2019), using a least square fit between all $S(f_i)$ and $R_W(f_i)$ values from all Doppler spectra and for each frequency band *i* within the wind-wave frequency range only, and the results are shown in Figure 4.13.

The coefficients estimated (see Figure 4.13) for each site are similar to each other, independently on wave frequency. In the wave frequency range (0.05 to 0.2 Hz) the coefficients obtained are of similar magnitude across the wind wave frequency range, independently of the site used. Furthermore, the frequency averaged values of the wind wave regression coefficients, $\alpha_w = 0.37 \pm 0.012$ and 0.26 ± 0.04 for PEN and PER sites are close to that estimated in Alattabi et al (2019) using a 48 MHz as well as to other

empirical studies used weighting function $W(f)$ (see Figure 4.13 and Table 4.6). This suggests that the wind wave regression coefficient is not radar frequency dependent and a frequency and site averaged value of 0.32 ± 0.02 is estimated as long as the second-order Doppler spectrum is weighted using Barrick's weighting function. Here the averaged value of wind-wave regression coefficients from all studies listed in Table 4.6 is estimated and the value $\alpha_w = 0.3$ is adopted for the inversion of the wind wave spectrum using Eqs. (4.24) and (4.25).

4.5.5 Hybrid method to estimate total wave spectrum

LPM2$_2$ has shown the best overall performance (see section 4.5.3) as it provided a higher number of successful inversions than the other methods and the best accuracy in swell height estimates (RMS error of 0.24m). Therefore, this method is adopted for estimating swell frequency, direction, and height from the Doppler spectra. These parameters are then used to reconstruct the swell spectrum assuming a Gaussian distribution (Alattabi et al., 2019) of the energy within the swell frequency band with the peak energy centered at the inverted swell frequency (f_s):

$$S_{sw}(f) = \left(H_{sw}^2 / 8\sqrt{2\pi\sigma^2}\right) \cdot e^{-\frac{(f-f_s)^2}{2\sigma^2}} \tag{4.36}$$

where σ is the width of the swell spectrum and $f < f_c$. The value of σ can be determined from historical data from the area, if available, or from validated model results (e.g., Kumar et al., 2017). Here, we used the value of 0.011. If the method failed to provide swell estimations, then it is assumed that no swell wave is present and the parameters $\sum R_W(f_i < f_c)$ and $S_{sw}(f)$ are set to zero.

After reconstructing the swell $S_{sw}(f)$ and wind wave $S_{ww}(f)$ spectra, these are combined to a single on-dimensional spectrum $inv.S(f)$ as follows (Alattabi et al., 2019):

$$inv.S(f) = \begin{cases} S_{sw}(f < f_c) + S_{ww}(f \geq f_c), \ if & r \geq 0.3 \\ S_{ww}(f) \qquad\qquad\qquad\qquad\quad , if & r < 0.3 \end{cases} \tag{4.37}$$

$$r = \frac{\sum R_W(f_i < f_c)}{\sum R_W(f_i \geq f_c)} \tag{4.38}$$

Where f_c is the swell-wind wave separation frequency determined using the wind speed and wave age (see section 4.4). The critical value of 0.3 in Eq. (4.37) was selected after trial and error as smaller values tended to indicate the presence of swell even when this was not present in the in situ record. When r <0.3 the inverted wind-wave spectrum is used for the entire range of frequencies including the swell band ($f_i < f_c$).

Bulk inverted wind wave parameters are calculated by integrating the total inverted wave spectrum $inv.S(f)$ over the range 0.046-0.35 Hz with spectral resolution of 0.0078 Hz.

4.5.5.1 One-dimensional wave spectra

The ability of the inversion method to estimate the one-dimensional wave spectra is demonstrated in Figure 4.14, where inverted spectra (solid lines) corresponding to events A – H are shown together with the in situ spectra (dashed lines). As described earlier, these events are examples of both wind waves (C, D, E and F) and swell (A, B, G and H) dominated spectra (see Figures 4.5 and 4.7). Overall, the high energy peaks in the

inverted spectra agree overall in both magnitude and frequency location with the in situ peak spectra, although in cases B, C and E, the inverted spectra fail to identify the secondary wind wave peaks present at higher frequencies.

4.5.5.2 Mean direction as a function of frequency

The estimation of mean direction as a function of wave frequency is carried out using Eq. (4.29) (see section 4.2.3) with Doppler spectra from both radar sites PEN and PER using their corresponding beams aiming at the buoy location. An example of inverted mean direction as function of frequency is shown in Figure 4.14 for events A-H (solid lines) together with the in situ directions estimated using the buoy data (dashed lines). The method seems to provide accurate estimates at least for the frequencies where significant wave energy has been identified in the inverted energy spectrum (see shaded area in Figure 4.14).

4.5.5.3 Full directional wave spectra

The directional wave spectra $inv.S(f,\theta)$ are constructed using Eqs. (4.30), (4.31), and (4.32) and using the inverted total wave $inv.S(f)$ and mean direction $\theta(f)$ spectra. The peak frequency identified on the $inv.S(f)$ is used to determine the value of β for the distribution function [see Eqs. (4.31) and (4.32), section 4.2.5]. The results of inverted directional frequency spectra for events A to H are shown in Figure 4.15 together with the corresponding in situ directional spectra. Except for events B and C, the remaining of the events show good agreement with in situ data, in terms of both wave energy levels, and peak energy location.

4.5.5.4 Bulk wave parameters

In comparing our estimates with the in situ data, we report the root mean square (RMS) error as in previous studies. However, since the RMS error always depends on the magnitude of the wave conditions, we also report the normalized root mean square error (NRMS), and the scatter index (SI). Since Mentaschi et al. (2013) argued that these parameters might not reflect accurate performance especially in cases of negative bias and suggested using the corrected indicator of Hanna and Heinold (1985) this latter parameter is also estimated.

Wave height, peak and mean wave frequencies were determined from the inverted total wave height spectra and these are compared to the in situ wave parameters in Figure 4.16 and Table 4.7. For the period of the experiment (total wave heights 0.29 to 5.1 m, mean wave height, 1.4 m) the RMS error of total wave height is 0.35m, correlation coefficient $r = 0.92$, and SI of 0.21. The inverted mean frequency estimation agrees better with the in situ data than the peak frequency, as their corresponding RMS errors are 0.02 and 0.03 Hz. The correlation coefficients for the mean and peak frequency estimates are 0.55 and 0.63, respectively while the slopes of the regression lines (<0.85) suggest some underestimation. Mean wave direction estimates appear to be slightly better than peak direction estimates with an RMS error of 38° and a complex correlation coefficient $|r|$ of 0.72 and angle 15°. The corresponding values for peak direction are 46°, 0.57, and 19°, respectively. Wind direction estimates are the least accurate with a relatively high RMS error (~72°) and a complex correlation coefficient with magnitude of 0.60 and angle of -4° (see Table 4.7).

The inverted wind-wave spectra are used to estimate the corresponding inverted wind-wave RMS wave height, peak and mean wave frequencies, and directions. These are compared to the partitioned parameters from in situ spectra and the scatter plots and the statistics of this comparison are shown in Figure 4.16 (red dots) and Table 4.7, respectively. The RMS error in wind-wave height is 0.34m with correlation coefficient of 0.93 and SI of 0.25. Peak frequencies show error of 0.04 Hz with a correlation coefficient of 0.66, while the mean frequency errors are slightly improved (RMS error of 0.03 Hz and $r = 0.73$). The slopes of the regression lines suggest that mean and peak frequencies are underestimated (slope ≤ 0.82). The peak direction has an RMS error of 43° with complex correlation coefficient $|r|$ of 0.70 and angle 18°, while RMS error of 41° with $|r| = 0.78$ and angle 15° are found in mean direction comparisons.

4.6 Discussion

4.6.1 Inverted swell parameters from LPM Swell inversion method

The results of swell inversion (section 4.5.3) suggest that the $LPM2_2$ method (Lipa et al. 1981) performs better than the other two methods (WFG and EMP). Although the application of the method was explored using different combinations of radar sites and beams (i.e., one site-one beam, one site-two beam, and two sites-two beams), use of two beams from two different sites ($LPM2_2$) provided the most accurate swell wave heights and performed better than LPM1 and $LPM2_1$. This could be attributed to the angle between the two beams. In the two sites – two beams scenario, the PEN and PER beams are almost perpendicular to each other (99°) while the angle of the beams used in $LPM2_1$ is only 30°. This low angle does not seem to be suitable to allow adequate resolution of the swell waves in the Doppler spectra.

Although the LPM method was found to perform the best for swell height did not perform satisfactorily for swell direction. Estimation of swell wave height requires knowing swell direction and frequency which are used within the coupling coefficient equation. The importance of these two parameters that are obtained through inversion is examined through a sensitivity analysis. For this analysis, the swell frequency and direction values from the in situ data are used (instead of the inverted ones) to estimate swell heights with the LPM method. The results from this exercise are compared to the original swell height estimates using LPM1, $LPM2_1$ and $LPM2_2$ and listed in Table 4.8. The resulting swell heights, from either LPM1, $LPM2_1$ or $LPM2_2$, do not seem to be significantly different, suggesting that swell height estimates do not depend heavily on the accuracy of the inverted swell frequency and direction. For instance, the use of in situ data in $LPM2_2$ provided wave heights with RMS error of 0.31m and a correlation coefficient r=0.78, while the original $LPM2_2$ method shows better agreement (see Table 4.8). The same situation can be seen for the other two methods. Since swell frequency and direction do not seem to be responsible for the errors in swell height estimates, it is concluded that identifying the swell peak energy in the Doppler spectrum R_j [see Eq. (4.35)] is most important. Errors in estimating R_j can be due to noisy Doppler spectrum but most likely it relates to the limits used to integrate the swell energy in the Doppler spectrum and to define the energy of the first order peak.

4.6.2 Inverted bulk wave parameters

The time series of inverted total and swell wave parameters are shown in Figure 4.17 and these include data with swell cross angle >75°. In Figure 4.17b, e, and h, the $LPM2_2$ inverted swell parameters are shown. In there the cases with swell cross angle

>75º are identified with green triangle symbols and show that these instances correspond to overestimated swell wave heights. However, total wave height estimates are in good agreement with the in situ values. Although an agreement is found in the estimates of mean and peak wave frequency the inversion method provides slightly underestimated values (see Figure 4.17e-f). This is similar to the findings of Lopez and Conley (2019) who also noted underestimations in frequency estimates.

The lack of inverted values (Figure 4.17 a-i) is attributed mostly to failure of the swell inversion when: 1) no swell peaks were identified in the Doppler spectrum (49% of the in situ swell record) and 2) Doppler spectra do not satisfy the QA criteria required (6% of the in situ swell record). The estimation of wind direction is shown in Figure 4.17k, and shows good agreement with the in situ data. The differences in data availability for wave inversion and wind direction estimations are attributed to the fact that the wind direction method relies only on the Bragg peak energy which is far above the noise level. This is not always the case for the second-order peaks used for swell and wind wave inversion.

The performance of the wave inversion method presented in this study is examined by comparing the results with those from other theoretical and empirical wave inversion studies (see Table 4.9). Our method shows to perform well, and the estimates of total wave height have RMS error of 0.35m, r=0.92, and SI of 0.21. These values are comparable and often better than the errors reported using more complicated theoretical wave inversion techniques (see Table 4.9). For mean and peak frequency estimations, it seems most inversion methods including this study show a similar, fair correlation with the in situ data (see Table 4.9).

4.6.3 Inverted wave and directional wave spectra

The inverted and in situ directional and non-directional wave spectra for events A-H (Figures 4.14 and 4.15) show strong agreements. The non-directional wave spectra agree in terms of energy content for most events except B, C, and E (Figure 4.14). During these events, the in situ spectra show secondary energy peaks at ~0.24 Hz; these peaks are not present in the inverted spectra. This is attributed to the weighting function $W(f)$ used in forming the normalized second-order spectra $R_W(f)$ [see Eq. (4.25)]. Its purpose is to reduce the effects of second harmonic and corner reflection peaks generated by the interaction of EM and ocean waves (Barrick, 1972b; Ivonin et al., 2006) (see Figures 4.18 and 4.19) that appear at $\pm 2^{1/2} f_B$ and $\pm 2^{3/4} f_B$ (see Figure 4.18). However, this might have some undesirable effects which are further explored. As shown in Figure 4.18, the weighting function for a 48 MHz radar shows the corner reflection peak to be at high wave frequencies (~0.49 Hz). For the 12 MHz system these undesirable peaks appear at frequencies 0.146 Hz and 0.241 Hz, respectively (see Figure 4.18) which are areas where significant wave energy might be present. In this case the weighting function would suppress the wave energy at these frequencies which can be seen both in the in situ spectra ($S(f)$) and in the non-weighted second-order spectra $R(f)$ corresponding to events B, C and E (see Figure 4.19). An example of a clear corner reflection effect can be seen in Figure 4.19, cases F and H, where the unweighted normalized second-order spectra $R(f)$ at these events (F and H) contain a secondary peak at 0.24 Hz; its signature is not found in the in -situ measurements (see Figure 4.19F and H). This obstacle of the application of the weighting function role should be considered as one of the limitations of this wave inversion method, at least for lower radar frequencies like the one in this

study and its application should be critically examined. Despite this limitation the overall energy content of the inverted spectra is similar to that of the in situ wave spectra.

The accuracy of inverted wave parameters and directional wave spectra estimated from the inversion method developed in this study are similar to those reported in Lopez and Conley (2019) who used the more complicated inversion method of Wyatt (2000).

Some wave inversion studies use 0.25 Hz as the upper frequency limit for 12 MHz systems due the limitation of the inversion method (for more details, see Lopez and Conley, 2019 and Wyatt, 2011). In this study, we extended the upper frequency limit to 0.35 Hz and the inverted wave and directional wave spectra estimated were satisfactory.

In addition to the limitations presented above, singularities for swell cross angles >75º (for 12 MHz), pose an additional limit for wave inversion when swell energy is present. The range of cross angles that singularities appear increases with decreasing radar frequency (i.e., >60º for 4 MHz) making this an important limitation for lower frequency systems. As shown in section 4.6.1 the accuracy of the LPM method to estimate swell wave height is mainly related to the method used to identify and accurately determine the swell peak energies R_j [see Eqs. (4.6) and (4.35)], something that depends on the limits used for defining the energy of the first order peak especially when this is broad but also on the limits used to estimate the swell induced energy. The technique could benefit from the development of more accurate and robust methods for estimating these cut-off frequency limits. The comparison of the three different beam/site combinations used in the application of the LPM method has revealed that: the use of two beams from a single site requires an angle between the two beams that is greater than 30º. However, this assumes that there is homogeneity in the swell signal at the two beams

which might not be the case especially for longer ranges. In addition, this limits the allowed number of beams available from a single beam forming radar where the radial coverage is limited to -60^o to 60^o from the radar boresight. Furthermore, the inverted results from LPM method for one site-one beam show high reduction of data availability because it requires all four swell peaks are available from a single Doppler spectrum, something that is not always possible. The LPM method performs best when Doppler spectra from two beams from two different sites are used.

4.7 Concluding remarks

In this manuscript, we introduced a relatively simple, semi-empirical method to estimate full wave and directional wave spectra from radar data even when swell is present. This method requires treating the wind-wave and swell inversions separately. The wind wave spectra estimation is based on the empirical method introduced by Barrick (1977b), while the swell spectra estimation utilizes a simplified version of the theoretical swell inversion presented by Lipa et al. (1981) which was found to be better performing than the WFG (Wang et al., 2016) and EMP (swell empirical approach introduced in this study) methods. The LPM method was found to perform best when two beams from two different sites ($LPM2_2$) are used as long as the swell cross-angle is below 75^o, for the 12 MHz system used in this study.

The inversion of the wind wave component is similar to that presented in Alattabi et al (2019), and the regression coefficient α_w was consistent for the two systems used in the study (PEN and PER sites) (see Figure 4.13). The value of 0.32 is found for α_w over ocean wave frequencies 0.05 - 0.2 Hz. This value is similar to other wave inversion studies that include the weighting function derived by Barrick (1977b) and used different

operating radar frequencies (see Table 4.6). This suggests that a constant value of 0.3 for wind wave regression coefficient would be sufficient for universal application independent of operation frequency.

Table 4.1: List of the swell wave inversion models evaluated in this study (see section 4.2) and their corresponding equations for swell frequency, direction, and height estimates. The sites and beam geometry (azimuth and range) used for each version of the model are also listed. The numbers in the model naming convention denote the number of sites and number of beams used in the inversion (i.e., $LPMJ_i$, where J denotes number of beams and subscript *i* indicates number of sites the beams are from, for example, $LPM2_1$ denotes two beams from one site, while $LPM2_2$ denotes 2 beams from 2 sites).

Model	**Peak Freq. Eq.**	**Swell Dir. Eq.**	**Swell Height Eq.**	**Radar Site(s)**	**beam 1 (° N)**	**beam 2 (° N)**	**Range 1 (km)**	**Range 2 (km)**
$LPM1_1$	(4.2)	(4.3)	(4.6)	PEN / PER	13 /272	-	20/31	-
$LPM2_1$	(4.10) (4.11)	(4.10) (4.11)	(4.12) (4.13)	PEN / PER	28 / 287	355 / 256	20/31	20/30
$LPM2_2$	(4.10) (4.11)	(4.10) (4.11)	(4.12) (4.13)	PRN & PER	13	272	20	31
$WFG1_1$	(4.10) (4.11)	(4.10) (4.11)	(4.15)	PEN / PER	13 / 272	-	20/31	-
$WFG2_1$	(4.10) (4.11)	(4.10) (4.11)	(4.16)	PEN / PER	28 / 287	355 / 256	20/31	20/30
$WFG2_2$	(4.10) (4.11)	(4.10) (4.11)	(4.16)	PRN &PER	13	272	20	31
$EMP1_1$	(4.2)	(4.18)	(4.20)	PEN / PER	13 /272	-	20/31	-
$EMP2_1$	(4.23)	(4.18)	(4.21) (4.22)	PEN / PER	28 / 287	355 / 256	20/31	20/30
$EMP2_2$	(4.23)	(4.18)	(4.21) (4.22)	PRN &PER	13	272	20	31

Table 4.2: Partitioned and total wave parameters for events A to H (see Figure 4.3) as estimated from the wave buoy data. The corresponding HF radar Doppler spectra parameters from sites PEN and PER are also listed for each event.

			Event							
			A	**B**	**C**	**D**	**E**	**F**	**G**	**H**
Wave Buoy	Time (day)		33.8	34.5	37.1	43.5	45.4	51.5	56.3	57.1
	Total H_{rms} (m)		0.61	0.64	0.72	0.95	0.62	1.32	1.30	1.40
	Swell H_{rms} (m)		0.52	0.37	0.26	0.47	0.36	0.91	1.10	1.30
	Wind H_{rms} (m)		0.33	0.5	0.54	0.73	0.38	0.86	0.72	0.37
	Peak freq. f_P (Hz)		0.08	0.09	0.15	0.15	0.13	0.09	0.10	0.09
	Mean freq. f_m (Hz)		0.12	0.18	0.19	0.16	0.18	0.14	0.13	0.12
	Mean wave dir. (°N)		102	113	183	117	124	89	52	69
	Swell dir. (°N)		94	97	148	113	103	94	53	81
	Mean wind wave dir. (°N)		134	123	186	119	132	84	51	52
	Wind dir. (°N)		101	175	6	141	230	201	281	212
	Wind speed (m/s)		6.2	8.5	5.5	6.4	5.4	7.6	3.1	4.8
Radar Sites	PEN	Noise (dB)	-162	-165	-164	-158	-162	-160	-159	-159
		σ_1 (dB)	53.2	50.7	50.8	45.5	55	42	49.2	45.4
		σ_2 (dB)	18.2	21.1	30.2	17	21.9	19	29.3	22.9
		$(\sigma_1/\sigma_2)_{peak}$	34.9	29.5	20.5	28.5	33.4	23.6	19.9	22.4
		Swell cross dir. (°)	82	85	43	78	88	82	41	69
	PER	Noise (dB)	-160	-161	-167	-163	-167	-166	-165	-168
		σ_1 (dB)	37.3	41	46.4	40.9	43.5	45	47.2	43.7
		σ_2 (dB)	14	15	20.6	23.2	15	26.9	25.4	25.8
		$(\sigma_1/\sigma_2)_{peak}$	23.2	26	25.7	17.7	28.4	18	21.7	17.8
		Swell cross dir. (°)	2	5	56	21	12	2	38	10

Table 4.3: List of statistical parameters from the comparison of in situ swell frequency with estimations from LPM and EMP (see Figure 4.9). RMSE: root-mean-square error, r: correlation coefficient; slope: regression slope; N and % represent the number and percentage of records used in the comparison.

No Sites / Beams Used	**Model**	**Site**	**Beam1 (º N)**	**Beam2 (º N)**	***N***	**%**	**RMS error (Hz)**	***r***	**Slope**
1 site / 1 beam	LPM1 Eq. (4.3)	PEN	13	-	263	48	0.01	0.40	0.92
		PER	272	-	324	60	0.01	0.59	0.90
		Common	-	-	164	30	0.01	0.60	0.92
		Combined	-	-	423	78	0.01	0.50	0.90
1 site / 2 beams	$LPM2_1$ Eq. (4.10-4.11)	PEN	28	355	400	74	0.01	0.31	0.95
		PER	287	256	375	69	0.01	0.60	1.07
		Common	-	-	270	50	0.01	0.60	1.03
		Combined	-	-	505	93	0.01	0.42	1.00
	$EPM2_1$ Eq. (4.23)	PEN	28	355	269	49	0.01	0.55	0.95
		PER	287	256	394	72	0.01	0.62	0.93
		Common	-	-	222	41	0.01	0.60	0.94
		Combined	-	-	441	81	0.01	0.66	0.93
2 sites / 2 beams	$LPM2_2$ Eq. (4.10-4.11)	PEN & PER	13	272	366	67	0.01	0.60	0.97
	$EPM2_2$ Eq. (4.23)	PEN & PER			280	51	0.01	0.61	0.94

Table 4.4: Evaluation of the different swell direction inversion methods (see text for details and Figure 4.10) against in situ data. The parameters listed are RMS error (RMSE), magnitude (|*r*|) and angle (in degrees) of complex correlation coefficient (*r*), and number (N) and corresponding percentage of data points used for the comparison.

No Sites / Beams Used	***Model***	**Site**	**Beam1 (º N)**	**Beam2 (º N)**	***N***	**%**	**RMS error (º)**	**Complex *r***	
								|*r*|	**Angle (º)**
1 site / 1 beam	LPM1 Eq. (4.2)	PEN	13	-	116	21	59	0.18	40
		PER	272	-	155	28	54	0.06	-46
		Common	-	-	50	9	40	0.09	4
		Combined	-	-	221	41	54	0.09	6
	EMP1 Eq. (4.18)	PEN	13	-	101	19	57	0.34	-13
		PER	272	-	146	27	44	0.31	4
		Common	-	-	99	18	51	0.37	-8
		Combined	-	-	148	27	49	0.39	-1
1 site / 2 beams	$LPM2_1$ Eqs. (4.10-4.13)	PEN	28	355	176	32	86	0.39	19
		PER	287	256	135	25	57	0.20	6
		Common	-	-	44	8	73	0.40	37
		Combined	-	-	267	49	99	0.33	16
	$EMP2_1$ Eq. (4.18)	PEN	28	355	46	8	85	0.52	-27
		PER	287	256	212	39	71	0.03	1
		Common	-	-	11	2	68	0.57	4
		Combined	-	-	247	45	73	0.10	-12
2 sites / 2 beams	$LPM2_2$ Eq. (4.10-4.13)	PEN&PER	13	272	267	49	48	0.53	20
	$EMP2_2$ Eq. (4.18)	PEN&PER			148	27	46	0.37	-7

Table 4.5: Evaluation of the different swell wave height inversion methods (see text for details and Figure 4.11) against in situ data. The parameters listed are RMS error (in m), correlation coefficient (*r*), regression slope, normalized RMS error (NRMS), scatter index (SI), corrected indicator (HH) and bias (BI) are listed. The number (N) and percentage (%) of data points used are also shown.

No Sites / Beams Used	**Model**	**Site**	**Beam1 (° N)**	**Beam2 (° N)**	***N***	**%**	**RMS error (m)**	***r***	**Slope**	**NRMS error**	**SI**	**HH**	**BI**
1 site / 1 beam	LPM1 Eq. (4.6)	PEN	13	-	116	21	0.94	0.53	1.23	0.97	0.92	0.97	0.28
		PER	271	-	154	28	0.75	0.53	1.26	0.82	73	0.73	0.33
		Common	-	-	50	9	0.60	0.63	1.20	0.58	0.50	0.53	0.31
		Combined	-	-	220	40	0.80	0.56	1.26	0.87	0.80	0.77	0.31
	WFG1 Eq. (4.15)	PEN	13	-	116	21	0.63	0.51	0.72	0.64	0.62	0.75	-0.17
		PER	272	-	154	28	0.55	0.62	1.11	0.60	0.57	0.57	0.17
		Common	-	-	50	9	0.38	0.72	0.88	0.36	0.36	0.39	-0.03
		Combined	-	-	220	40	0.55	0.57	0.95	0.61	0.60	0.62	0.04
	EMP1 Eq. (4.20)	PEN	13	-	99	18	0.66	0.64	1.08	0.67	0.66	0.64	0.10
		PER	272	-	144	26	0.47	0.70	1.02	0.47	0.46	0.46	0.10
		Common	-	-	97	18	0.42	0.77	1.05	0.42	0.40	0.41	0.11
		Combined	-	-	146	27	0.40	0.79	1.04	0.40	0.39	0.39	0.09
1 site / 2 beams	$LPM2_1$ Eqs. (4.12-4.13)	PEN	28	355	170	31	0.45	0.77	0.54	0.52	0.38	0.70	-0.31
		PER	287	256	130	24	0.41	0.73	0.75	0.43	0.40	0.50	-0.15
		Common	-	-	42	8	0.43	0.82	0.67	0.41	0.30	0.51	-0.29
		Combined	-	-	258	47	0.41	0.77	0.63	0.46	0.38	0.58	-0.23
	$WFG2_1$ Eq. (4.16)	PEN	28	355	194	36	0.44	0.78	0.55	0.51	0.39	0.69	-0.29
		PER	287	256	199	37	0.87	0.43	1.03	0.91	0.90	0.90	0.15
		Common	-	-	75	14	0.52	0.57	0.70	0.53	0.51	0.64	-0.14
		Combined	-	-	318	58	0.66	0.50	0.85	0.74	0.74	0.80	-0.05

	$EMP2_1$ Eqs. (4.21-4.22)	PEN	28	355	45	8	0.83	0.78	1.43	0.79	0.66	0.66	0.45
		PER	287	256	210	39	1.14	0.57	1.84	1.38	1.07	1.06	0.72
		Common	-	-	11	2	0.41	0.86	1.06	0.40	0.33	0.39	0.23
		Combined	-	-	244	45	1.10	0.61	1.77	1.28	0.99	0.96	0.70
2 sites / 2 beams	$LPM2_2$ Eqs. (4.12-4.13)	PEN&PER	13	272	253	47	0.24	0.85	0.87	0.32	0.32	0.34	-0.02
	$WFG2_2$ Eq. (4.16)	PEN&PER			258	47	0.39	0.62	0.84	0.52	0.52	0.56	-0.02
	$EMP2_2$ Eqs. (4.21-4.22)	PEN&PER			145	27	0.37	0.79	1.04	0.42	0.42	0.42	0.08

Table 4.6: List of wind wave coefficient α_w estimates for use with the empirical wave inversion algorithm [see Eq. (4.24)] reported in this and previous studies. The transmitting frequencies used are also listed.

Study	**Radar Frequency (MHz)**	$\boldsymbol{\alpha_w}$
Heron and Heron (1998)	25.4	0.30
Ramos et al. (2009)	25.4	0.34
Alattabi et al. (2019)	48	0.25
This study	12	0.32

Table 4.7: Statistical comparison of in situ and inverted estimates of total and wind-wave RMS wave height, mean and peak frequency, mean and peak direction (see Figure 4.16). The root-mean-square (RMS) error, correlation coefficient (r) for wave height, frequency estimates and direction (complex, shown as r and Angle). In addition, regression slope, normalized RMS error (NRMS), scatter index (SI), corrected indicator (HH) and bias (BI) are listed for wave heights and frequencies. Note, in this comparison 626 data points are used that corresponds to 93% of total data availability (674 data points).

	Parameter	**RMS error**	***r***	**Angle (º)**	**Slope**	**NRMS error**	**SI**	**HH**	**BI**
Total	H_{rms}	0.35 m	0.92	n/a	1.02	0.21	0.21	0.21	0.03
	f_P	0.03 Hz	0.63	n/a	0.85	0.25	0.24	0.27	-0.01
	f_m	0.02 Hz	0.55	n/a	0.82	0.22	0.15	0.24	-0.02
	Peak Dir.	46ºN	0.57	19	n/a	n/a	n/a	n/a	n/a
	Mean Dir.	38ºN	0.72	15	n/a	n/a	n/a	n/a	n/a
Wind-wave	H_{rms}	0.34 m	0.93	n/a	1.11	0.26	0.25	0.25	0.12
	f_P	0.04 Hz	0.66	n/a	0.80	0.28	0.24	0.32	-0.02
	f_m	0.03 Hz	0.73	n/a	0.82	0.21	0.13	0.23	-0.03
	Peak Dir.	43º	0.70	18	n/a	n/a	n/a	n/a	n/a
	Mean Dir.	41º	0.78	15	n/a	n/a	n/a	n/a	n/a
Wind	*Wind Dir.*	72º	0.60	-4	n/a	n/a	n/a	n/a	n/a

Table 4.8: Comparison of the performance of the swell inversion method (LPM) to estimate swell wave height using inverted (LPM) and measured (<LPM>) swell frequency (f_s) and direction (θ_{sw}) as described in section 4.5.3. The comparisons of inverted vs in situ swell height are presented in terms of RMS error (in m), correlation coefficients (r) and regression slope. N is number of data points used.

No Sites / Beams Used	**Model**	**Site**	**Beam1 (º N)**	**Beam2 (º N)**	***N***	**%**	**RMS error (m)**	***r***	**Slope**
1 site / 1 beam	LPM1 Eq. (4.6)	PEN	13	-	116	21	0.94	0.53	1.23
		PER	271	-	154	28	0.75	0.53	1.26
	<LPM1>	PEN	13	-	262	48	0.56	0.44	0.86
		PER	272	-	433	80	0.71	0.44	1.12
1 site / 2 beams	$LPM2_1$ Eqs. (4.12-4.13)	PEN	28	355	170	31	0.45	0.77	0.54
		PER	287	256	130	24	0.41	0.73	0.75
	<$LPM2_1$>	PEN	28	355	92	17	0.53	0.63	0.72
		PER	287	256	340	63	0.57	0.47	1.01
2 sites / 2 beams	$LPM2_2$ Eqs. (4.12-4.13)	PEN&PER	13	272	253	47	0.24	0.85	0.87
	<$LPM2_2$>	PEN&PER			125	23	0.31	0.78	0.95

Table 4.9: Comparison of the performance of the hybrid model presented in this study with other (theoretical and empirical) wave inversion methods reported in the literature. Root-mean-square errors (RMSE) and correlation coefficients (*r*) of total wave height, peak and mean wave period estimated using in situ measurements are listed.

Inversion Type	**Study**	f_{radar} **(MHz)**	H_{rms} **(m)**		T_P **(s)**		T_m **(s)**	
			RMSE (m)	r	**RMSE (s)**	r	**RMSE (s)**	r
Theoretical	Wyatt et al. (2006)	7-10	0.19-0.46	0.55-0.94	-	-	1.27-4.56	0.13-0.81
	Wyatt et al. (2009)	16	0.28-0.32	0.96-0.97	-	-	-	-
	Hisaki (2016)	24.5	0.15-0.86	0.63-0.76	-	-	0.26-0.95	0.69-0.82
	Saviano et al. (2019)	25	0.23-0.66	0.50-0.75				
Empirical	Chen et al. (2013)	7.5-25	0.19-1.29	0.45-0.82	-	-	-	-
	Gomez et al. (2015)	12	0.25-0.48	0.78-0.93	1.46-4.23	0.33-0.76	0.81-2.81	0.52-0.81
	Middleditch (2013)	8.34	0.36-0.70	0.35-0.51	0.89-2.44	0.3-0.57	0.72-1.26	0.28-0.50
	Ramos et al. (2009)	25.4	0.14-0.50	0.68-0.95	-	-	-	-
	Lopez et al. (2016)	12	0.18-0.36	0.88-0.96	-	-	-	-
	Lopez and Conley (2019)	12.3	0.30-0.45	0.87-0.94				
	Alattabi et al. (2019)	48	0.16-0.25	0.86-0.94	1.38-2.16	0.51-0.84	0.79-0.84	0.80-0.95
Semi-Empirical	This study	12	0.35	0.92	2.1	0.63	0.88	0.55

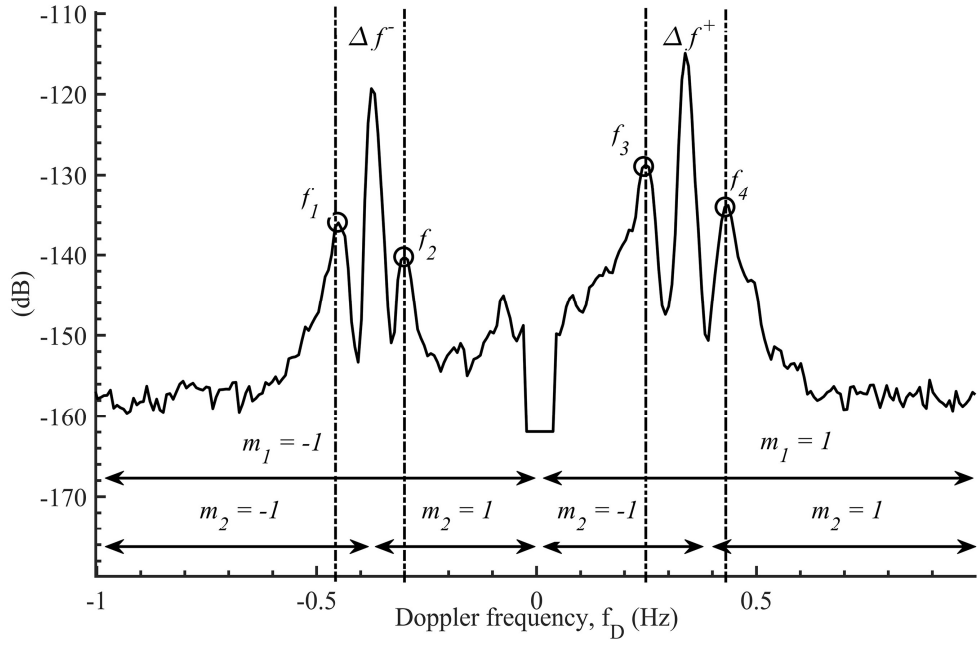

Figure 4.1: Example of HF radar Doppler backscatter spectrum obtained from the HF radar (12 MHz) used in this study. The locations of the four peaks (f_1 to f_4) due to swell waves are shown. The horizontal lines denote the regions of the Doppler spectra that the values of m_1 and m_2 correspond to [see Eq. (4.1)].

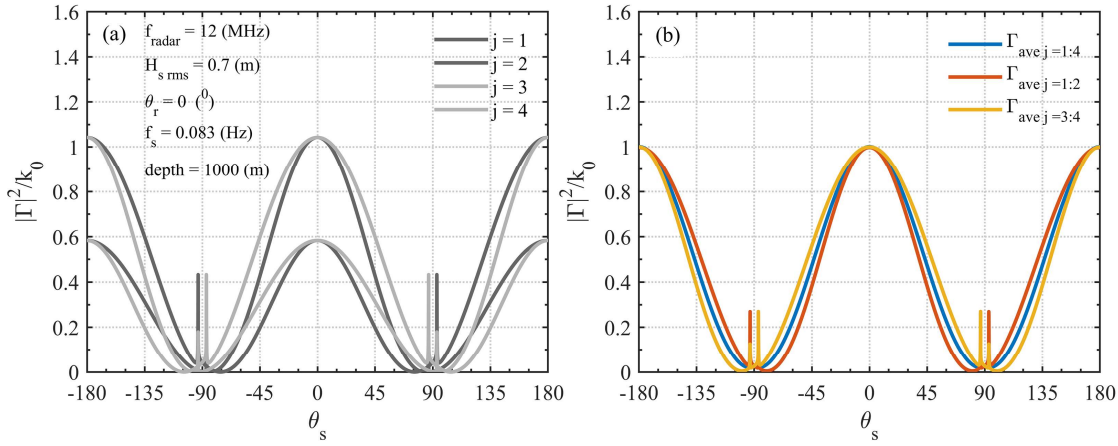

Figure 4.2: (a)Variability of normalized coupling coefficient for each swell peak around the Bragg peaks (j = 1 to 4) (gray lines) as a function of swell cross-angle. (b)Variability of various combinations of averages using the values shown on the left: (i) average of all 4 coefficients (j=1:4, in blue); (ii) average of the two coupling coefficients corresponding to the negative (j = 1:2, in red) and positive (j=3:4, in orange) sides of the Doppler spectrum.

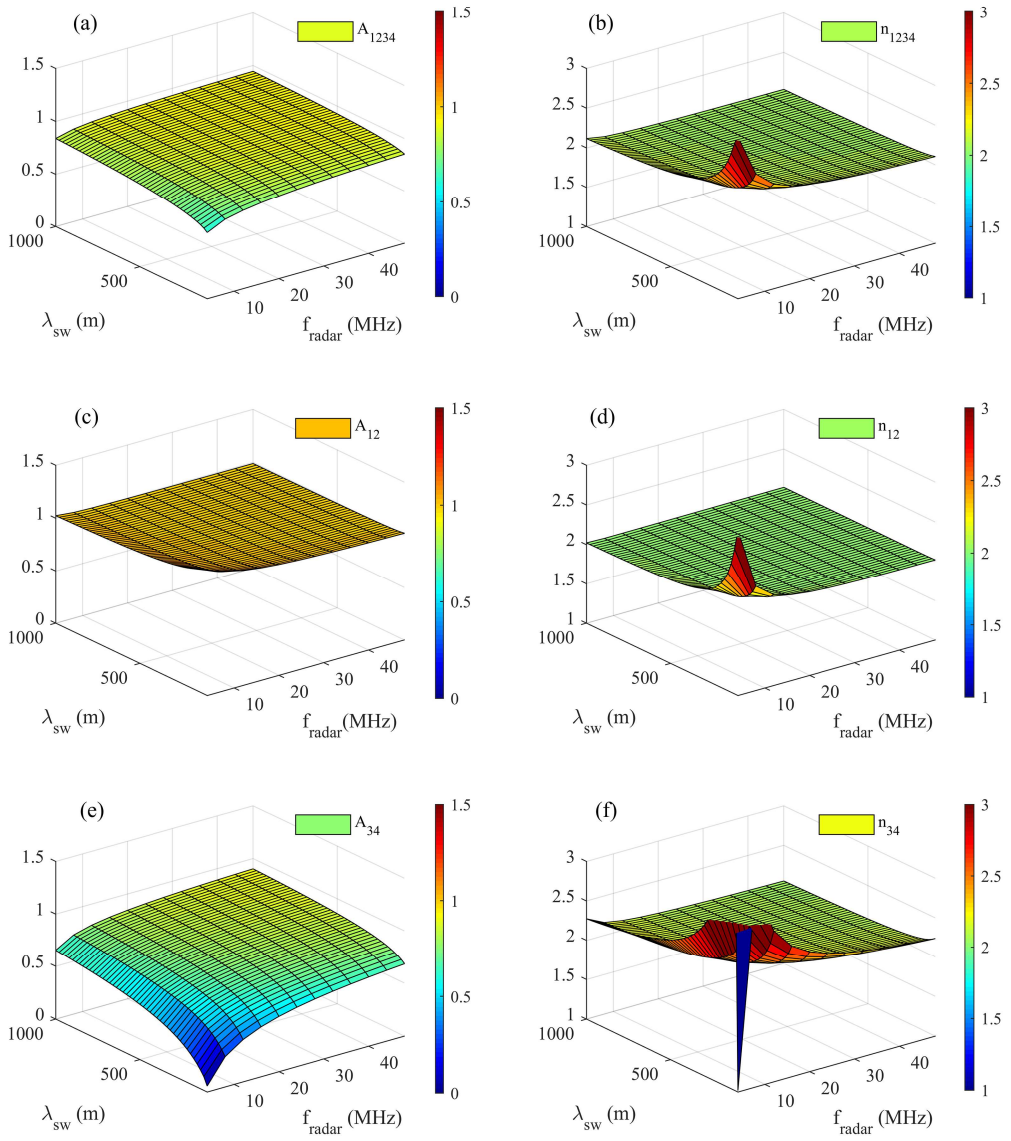

Figure 4.3: Variability of maximum value of the averaged coupling coefficients (A_j) for swell peaks around the Bragg peaks (left panels) and the exponent (n) in (see Eqs. (4.19) and (4.20), right panels) as a function of radar frequency (f_{radar}) and swell wavelength (λ_{sw}). (a) Maximum of the mean of all four coupling coefficients (A_{1234}), and (b) the corresponding (n_{1234}) exponent. (c) Maximum of the average (A_{12}) of two coupling coefficients from the negative side (j = 1 to 2), and (d) the corresponding exponent (n_{12}). (e) Maximum of the average (A_{34}) of the two coupling coefficients from the positive side of the Doppler spectrum (j = 3 to 4), and (f) the corresponding exponent (n_{34}).

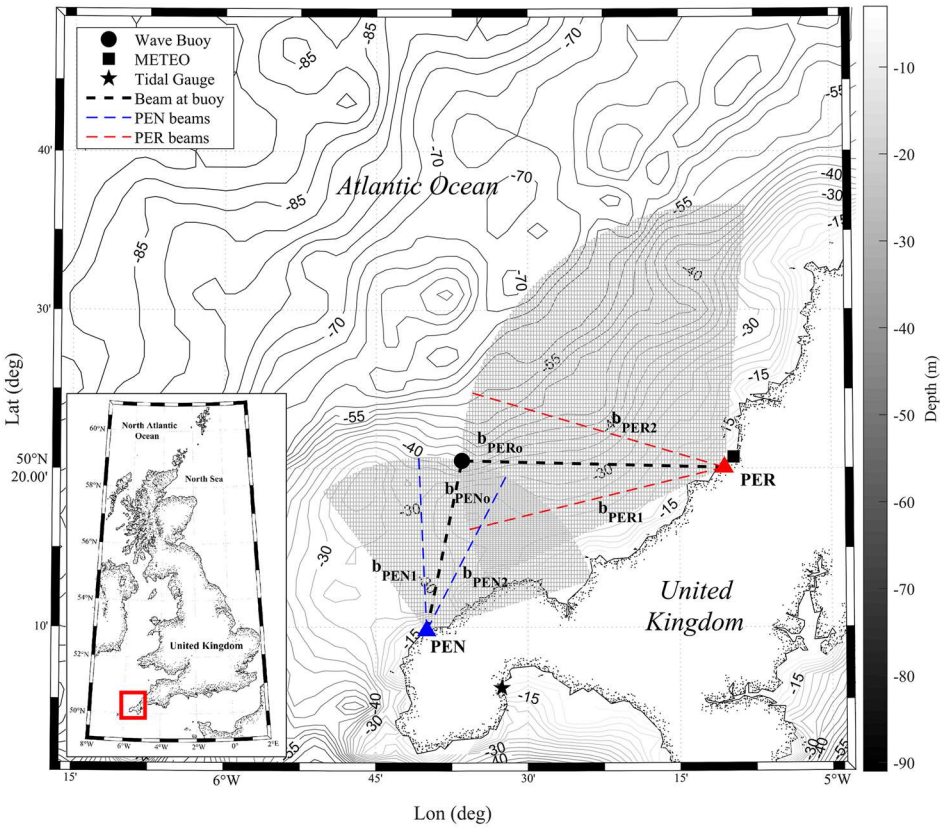

Figure 4.4: Map showing the study area in Cornwall (United Kingdom) and the HF radar installation sites at Pendeen (PEN) and Perranporth (PER) shown as blue and red triangles, respectively. The locations of the wind and tide gauge stations used in this study are indicated by a square and star symbol, respectively, while the wave buoy deployment location is shown as a solid black circle. The black dashed lines indicate the radials (beams) used for the inversions (b_{PENo} and b_{PERo} for PEN and PER sites, respectively). The dashed blue and red lines denote the two radials (beams) used for single site inversions and they form a 30° angle (b_{PEN1} and b_{PEN2} for PEN site, and b_{PER1} and b_{PER2} for PEN site). Depth contours are shown in meters.

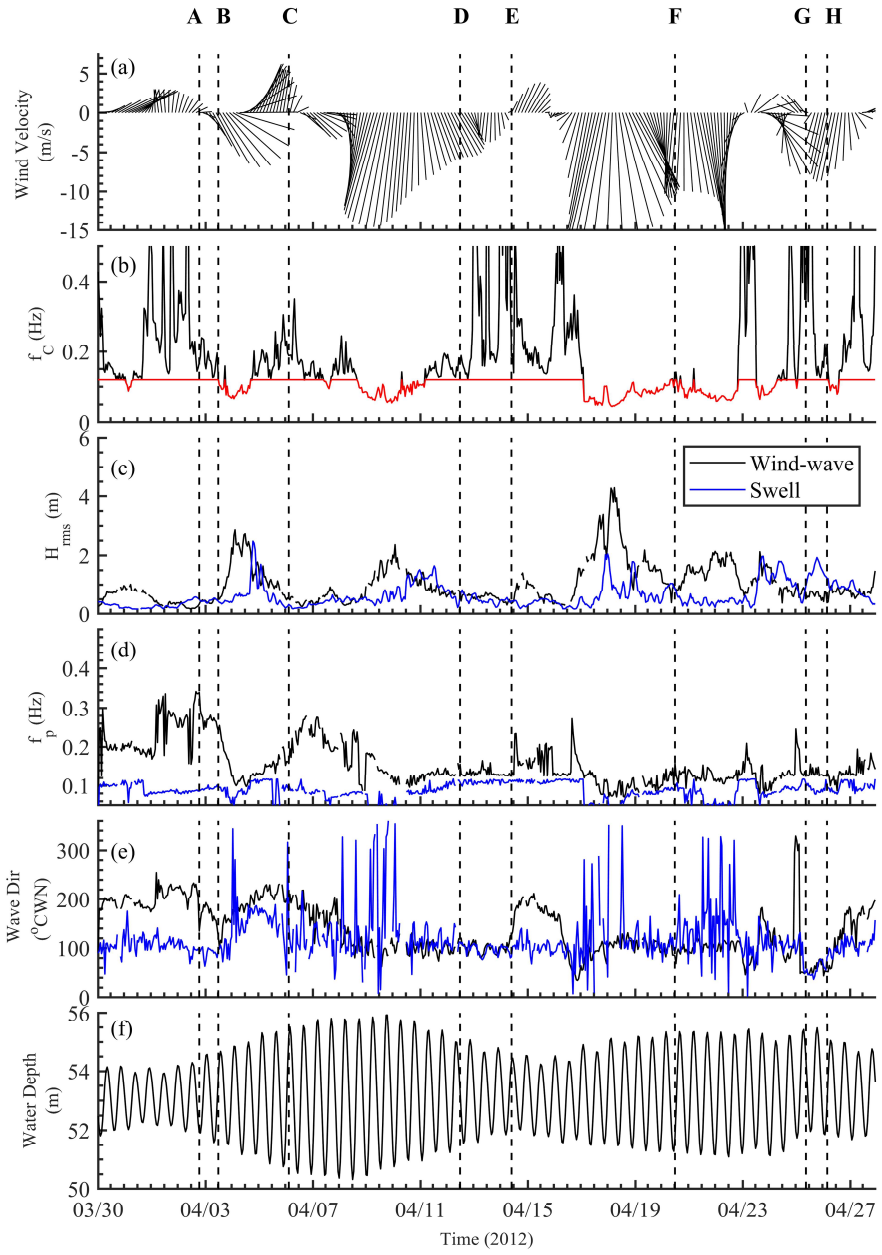

Figure 4.5: Time series of wind forcing (measured at the coastline near PER) and partitioned wind-wave (black) and swell (blue) parameters at the wave buoy location (see Figure 4.3): (a) wind vector diagram, (b) swell/wind separation frequency. The black line shows the values estimated using Eq. (4.33), while the red line shows the values adopted after applying the maximum cutoff frequency limit of 0.12 Hz (see text for details), (c) partitioned wind-wave and swell RMS wave heights, (d) partitioned peak frequencies for wind-waves and swell, (e) mean direction for wind-waves and swell (from true north), and (f) water depth (in m) measured at Newlyn tide gauge station (station ID 202). The vertical dashed lines identify specific wind waves/swell events (A to H) discussed in detail in this study (see text for details).

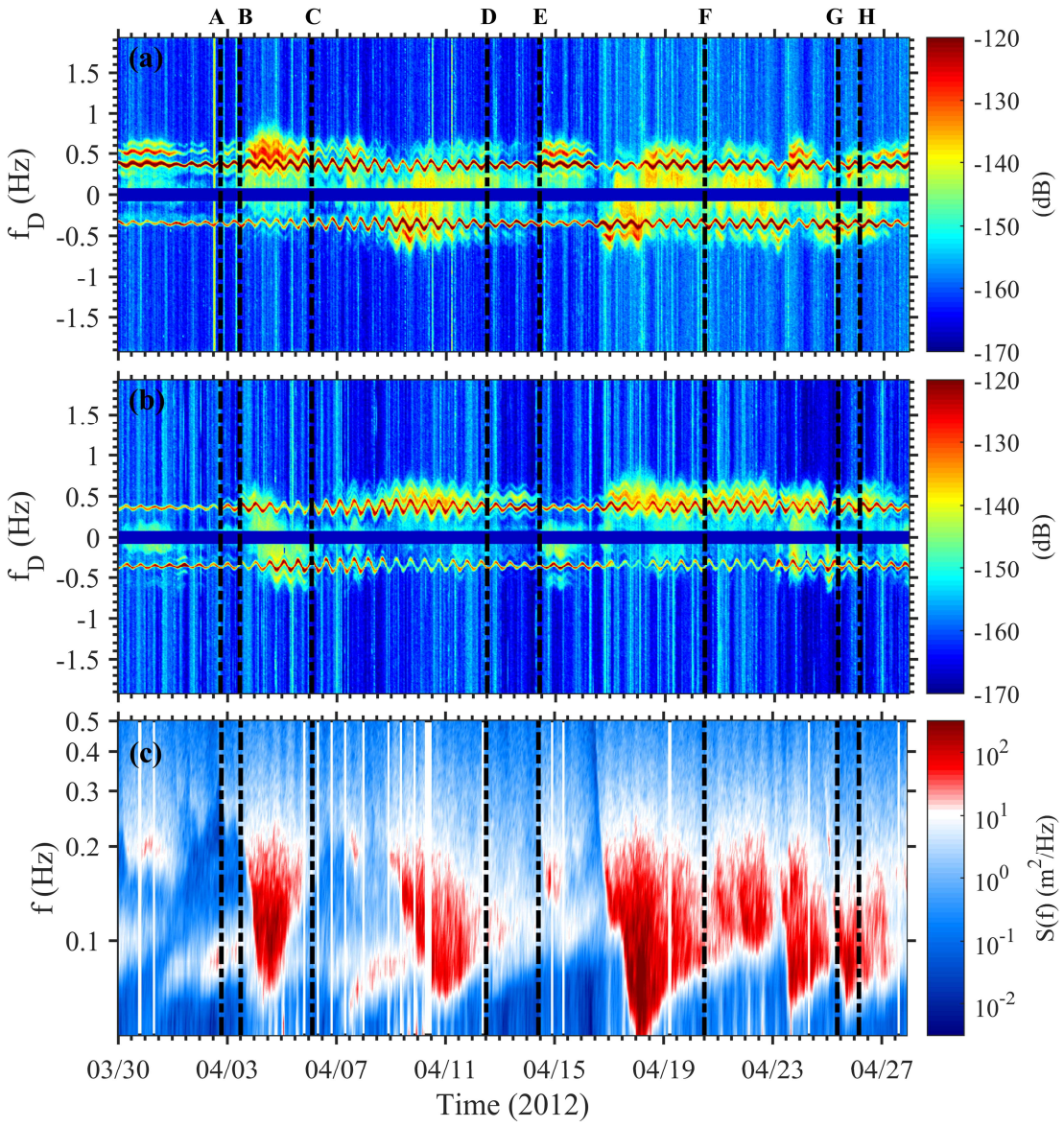

Figure 4.6: Time stacks of radar Doppler spectra at the wave buoy location from (a) PEN and (b) PER radar systems (b_{PENo} and b_{PERo} beams, see Figure 4.4). (c) Time stack of corresponding wave spectral energy density $S(f)$ as estimated using the wave buoy data. Vertical dashed lines A to H identify specific wind waves/swell events (see text and Table 4.2 for details).

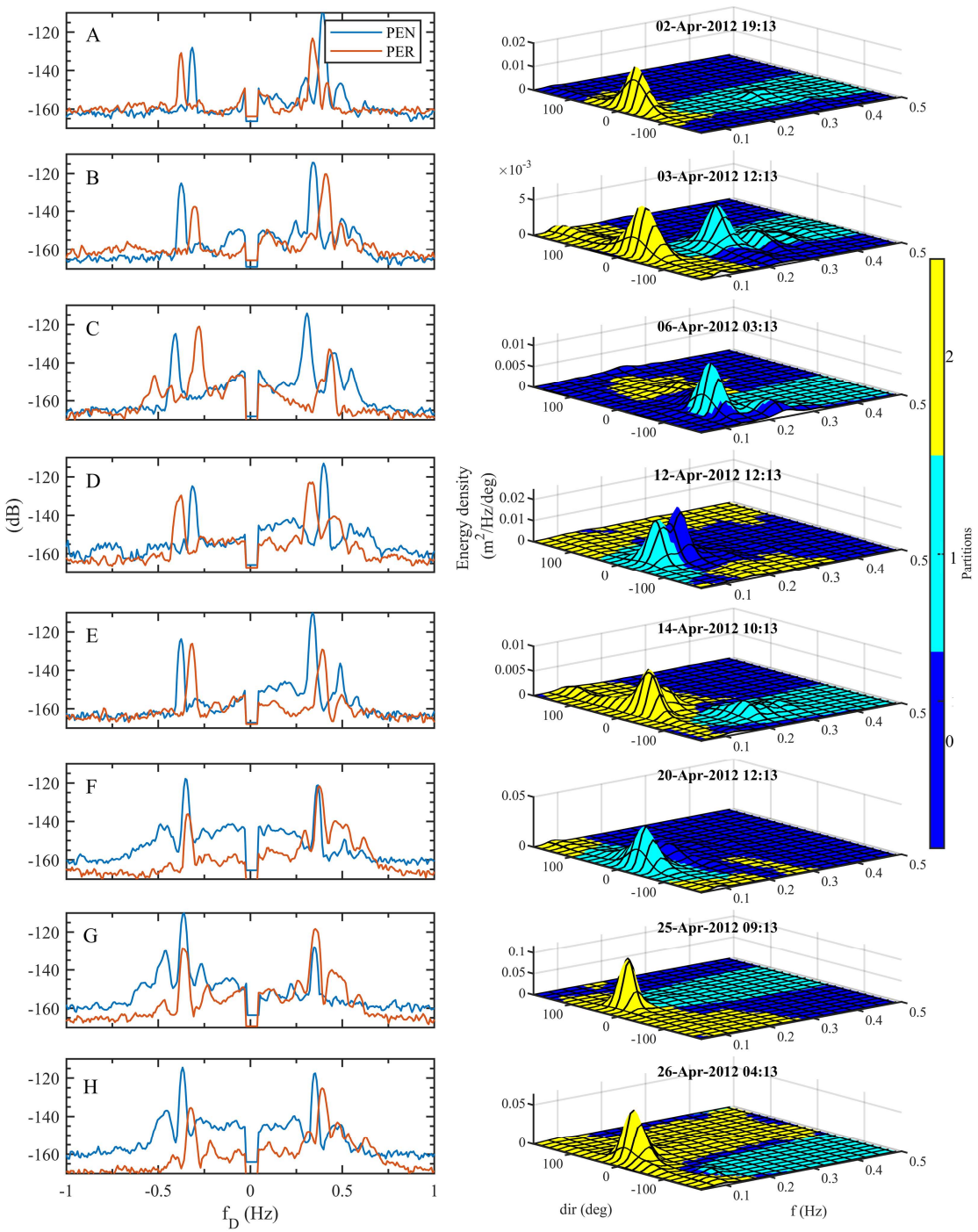

Figure 4.7: Left: Individual HF radar Doppler spectra for PEN (blue) and PER (red) sites corresponding to wave events A to H (see Figure 4.6). Right: Directional wave spectra for the same events with the swell and wind wave partitions identified using yellow and light blue shadings. Dark blue corresponds to background noise not associated with surface waves.

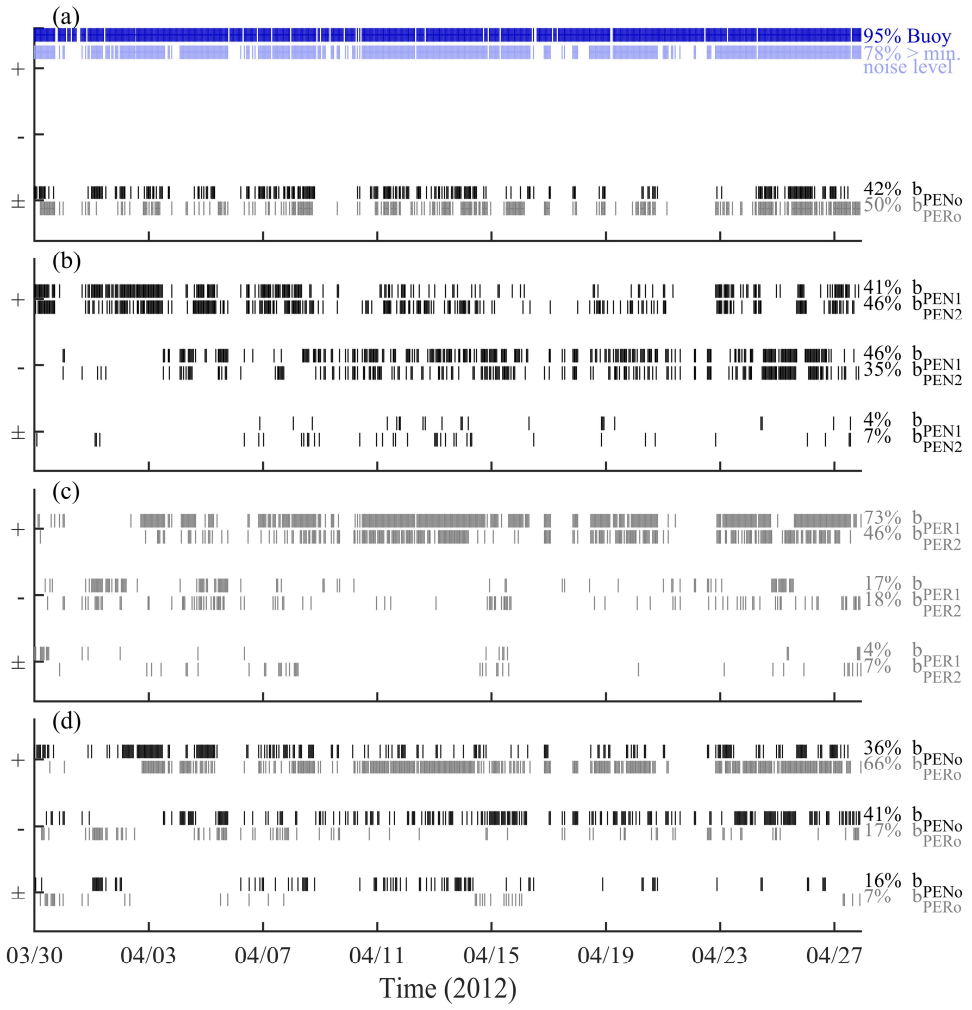

Figure 4.8: Instances when swell peaks are identifiable in the Doppler spectra for use in the swell inversion using (a) one beam from a one site method, (b) two beams from one site (PEN), (c) two beams from one side (PER), and (d) two beams from two sites. Key: (±) represents instances where all four swell-induced peaks are identifiable in a single Doppler spectrum; (-) and (+) when two peaks are identifiable on the negative and positive side of the Doppler spectra, respectively. The black and gray lines denote the data beams from PEN and PER radar sites, respectively. Note: b_{PENo} and b_{PERo} denote beams from PEN and PER sites pointed at buoy location, b_{PEN1} and b_{PEN2} beams from PEN site, and b_{PER1} and b_{PER2} beams from PER site (see Figure 4.4). The dark blue marks in (a) denote swell recorded by the wave buoy while the light blue marks denote instances when the recorded swell was above the minimum noise level (0.15 m^2 Hz^{-1}) required for evaluating the swell inversion algorithms. Their percentages are estimated over the total data available. The percentage of radar data availability is shown for each case and represent data availability over the number of in situ swell data points that passed the minimum noise level criterion.

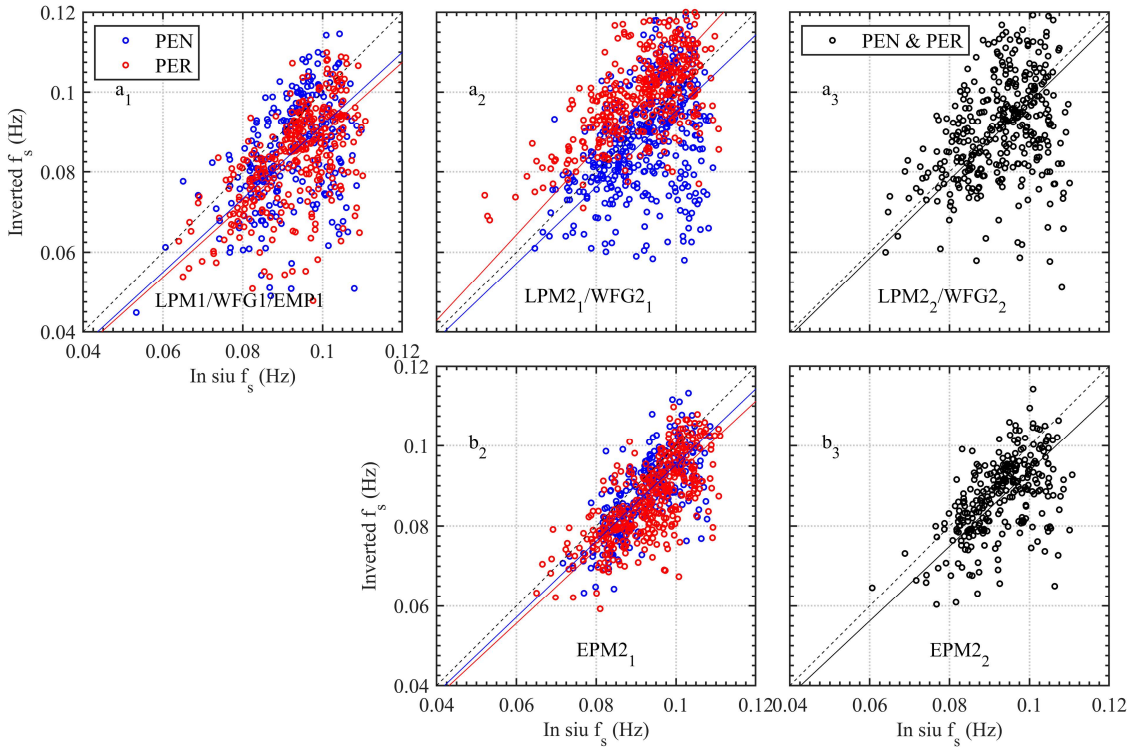

Figure 4.9: Scatter plot of inverted and in situ swell frequencies using: (a_1) one beam from a single site (LPM1, WFG1, and EPM1); (a_2) two beams from a single site ($LPM2_1$ and $WFG2_1$); (a_3) two beams from sites PEN and PER, respectively ($LPM2_2$ and $WFG2_2$); (b_2) two beans from a single site ($EPM2_1$); and (b_3) same beams and sites as in (a_3) using the $EPM2_2$ method. For statistics see Table 4.3.

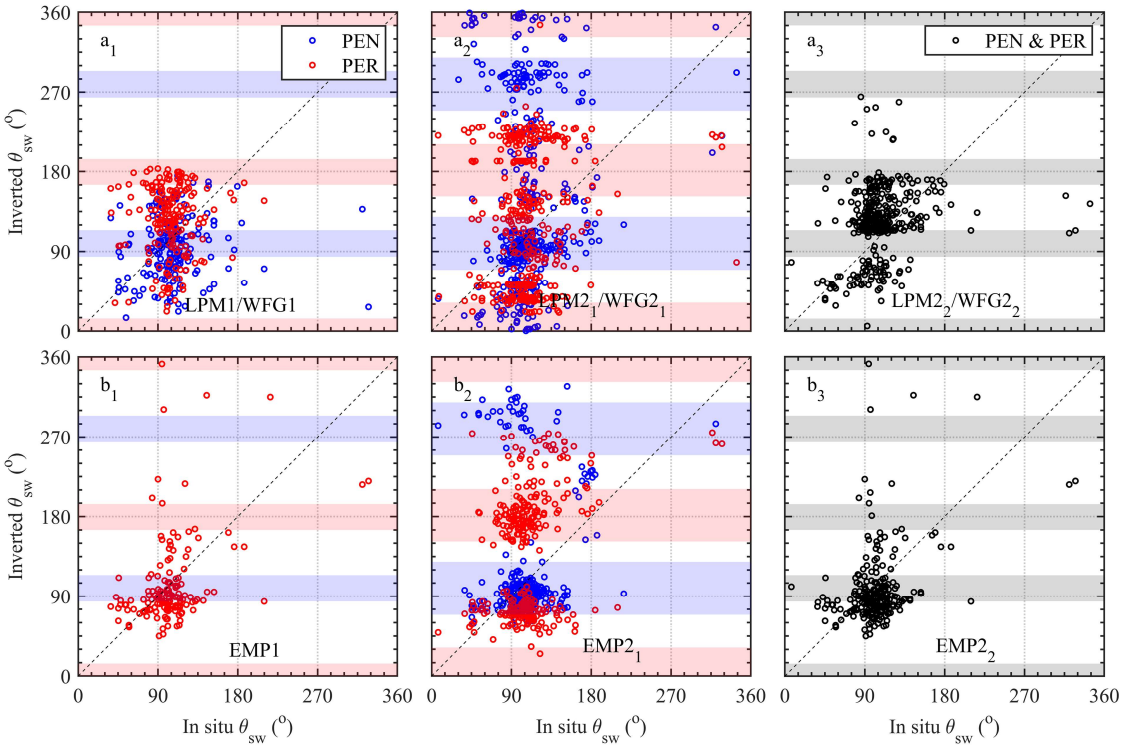

Figure 4.10: Scatter plot of inverted and in situ swell directions using the LPM (a_1-a_3), and EMP (b_1-b_3) methods, for PEN (blue circles) and PER (red circles). The methods utilized used one site - one beam (a_1 and b_1), one site-two beams (a_2 and b_2), and two sites - two beams (a_3 and b_3). The shaded ranges denote the range of inverted swell cross angle $|\theta_s|$ >75° which are excluded from swell wave height inversions. For statistics see Table 4.4.

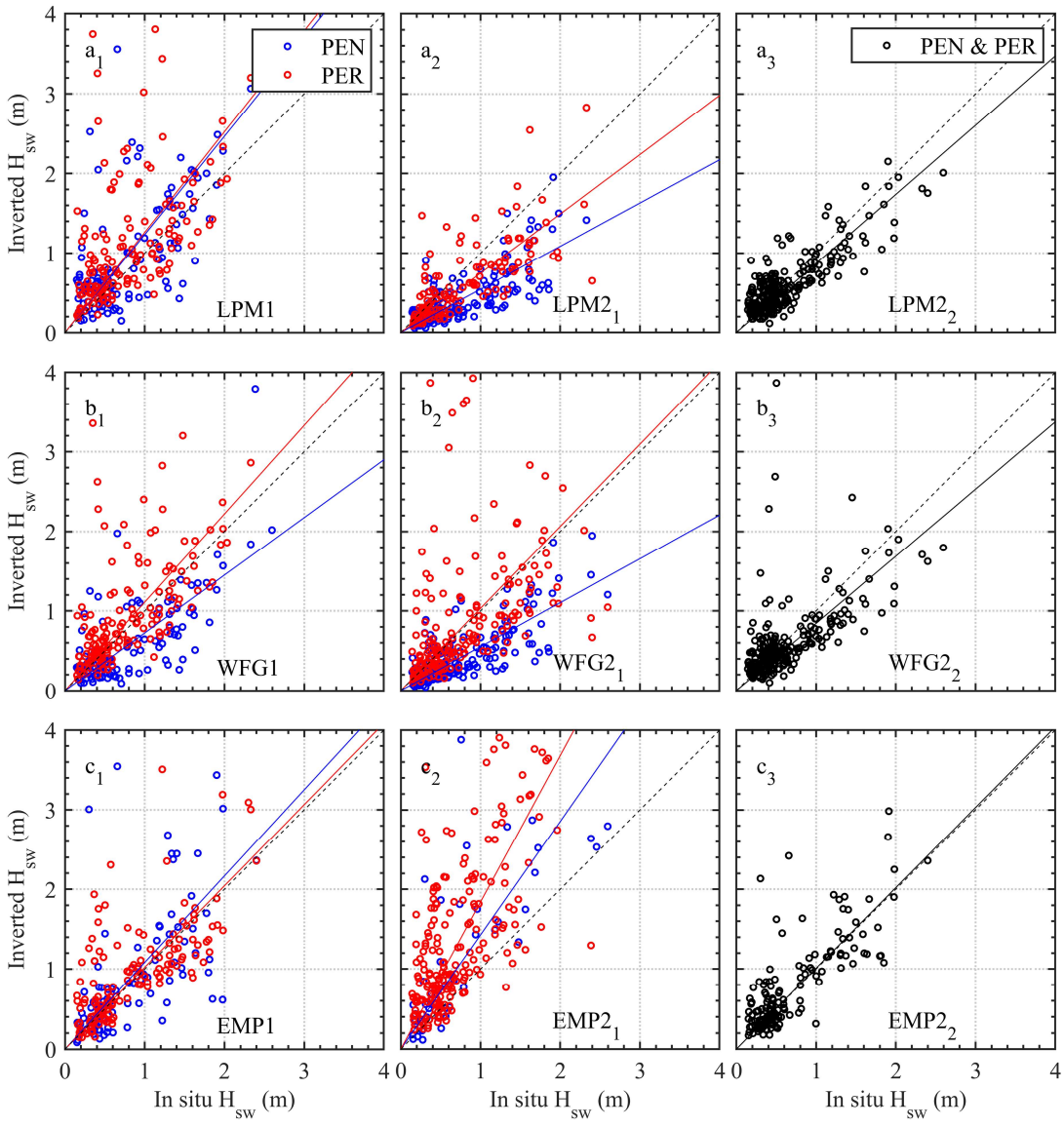

Figure 4.11: Scatter plot of in situ and inverted RMS swell wave heights using LPM (a_1-a_3), WFG (b_1-b_3), and EMP (c_1-c_3) for PEN (blue circles) and PER (red circles) for one sit- one beam (left panel), one site-two beam (middle panels), and two sites – two beams (right panels). For statistics see Table 4.5.

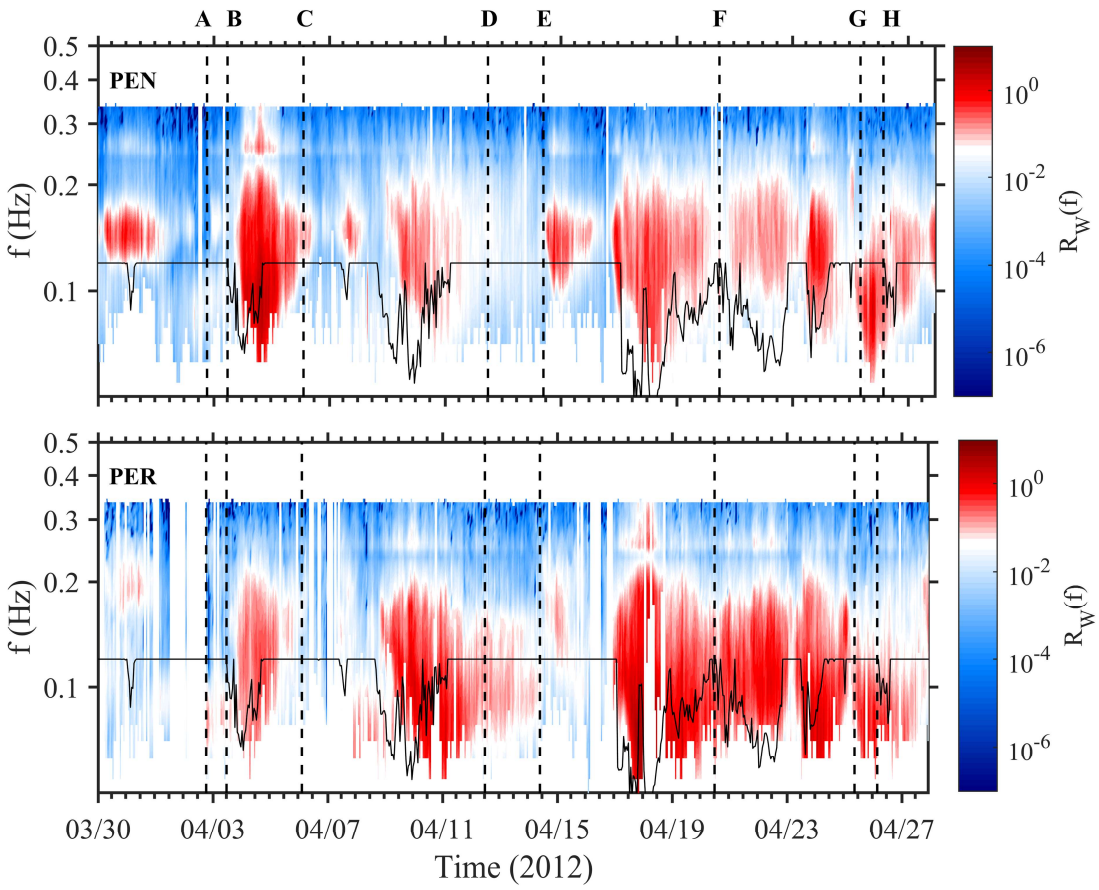

Figure 4.12: Time stacks of weighted normalized second-order radar spectra $R_W(f)$ for PEN (top panel) and PER (bottom panel) estimated using Doppler spectra from the range and azimuth corresponding to the buoy location [see Eq. (4.25)]. The solid black curve denotes the separation frequency used in this study (see text for details). Vertical dashed lines marked A–H identify specific wind waves/swell events (see Figure 4.6a, b).

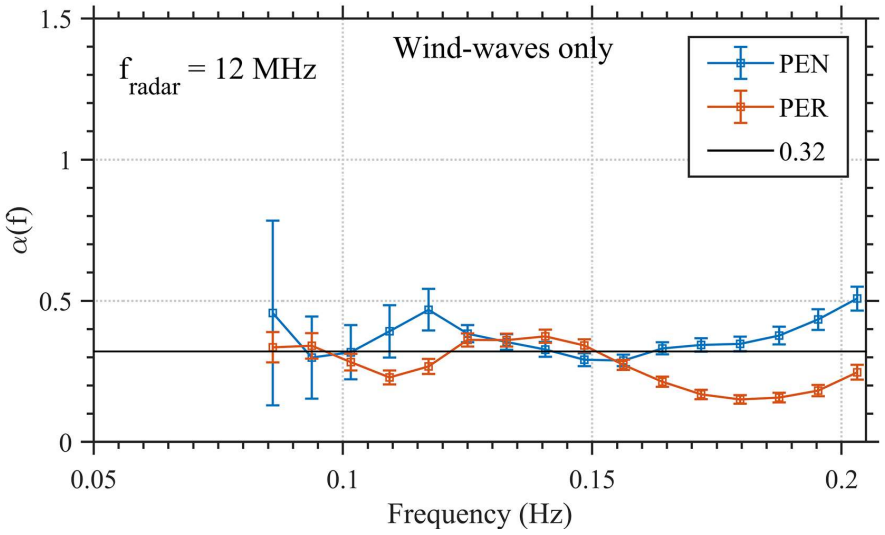

Figure 4.13: Wind wave coefficient $\alpha(f)$ values determined from weighted normalized second-order spectra from PEN (blue) and PER (red) beam data pointing at buoy location using the method described in Alattabi et al. (2019). The solid horizontal line is the averaged $\alpha_w = \langle \alpha(f) \rangle = 0.32$ over the frequency range 0.05 to 0.2 Hz.

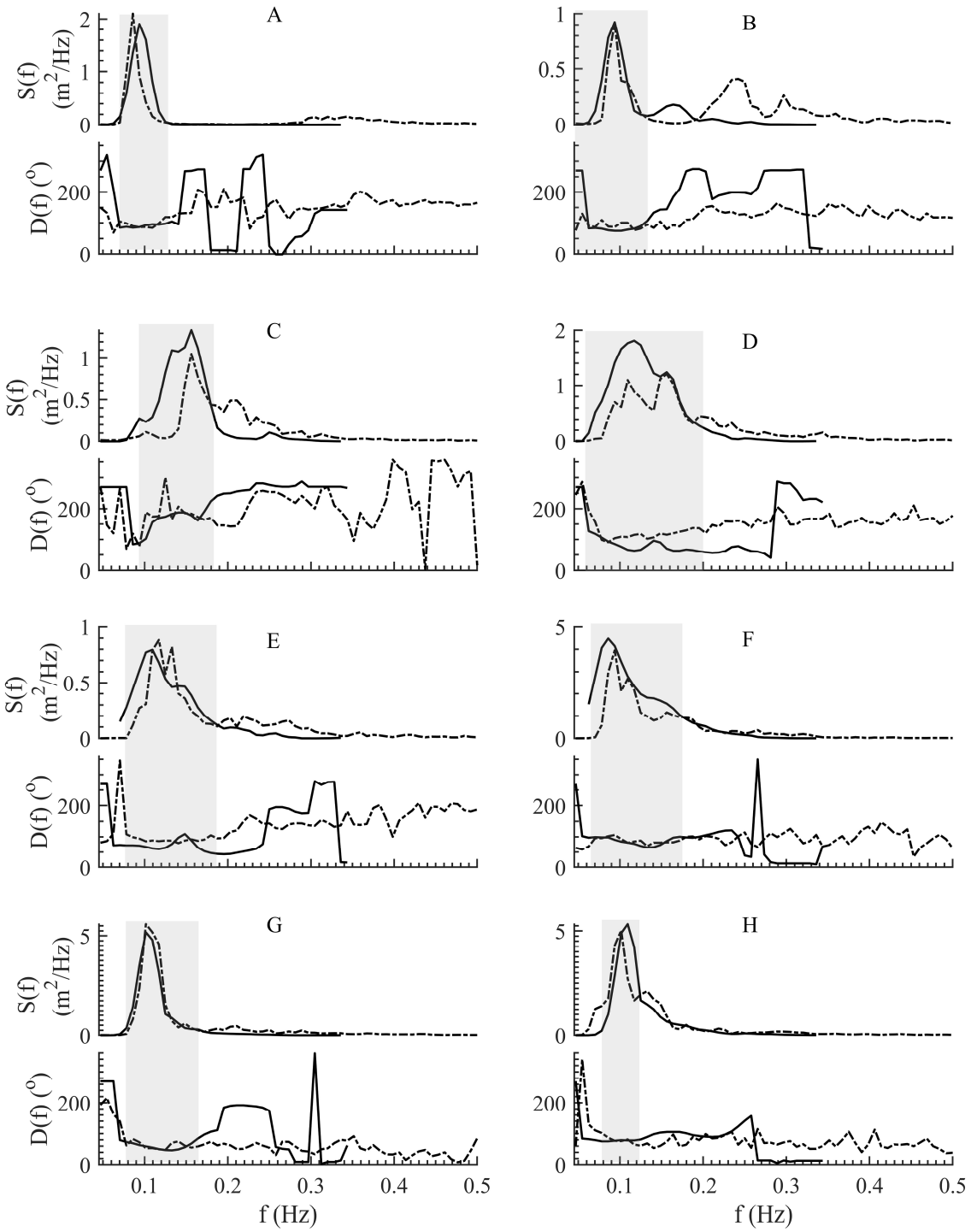

Figure 4.14: Comparison of inverted (solid lines) and in situ (dashed lines) wave energy $S(f)$ and mean direction $D(f)$ spectra for A to H. The total inverted wave energy spectra are obtained using the LPM2$_2$ method for swell and the average of the wind wave spectra from the two sites (PEN and PER).

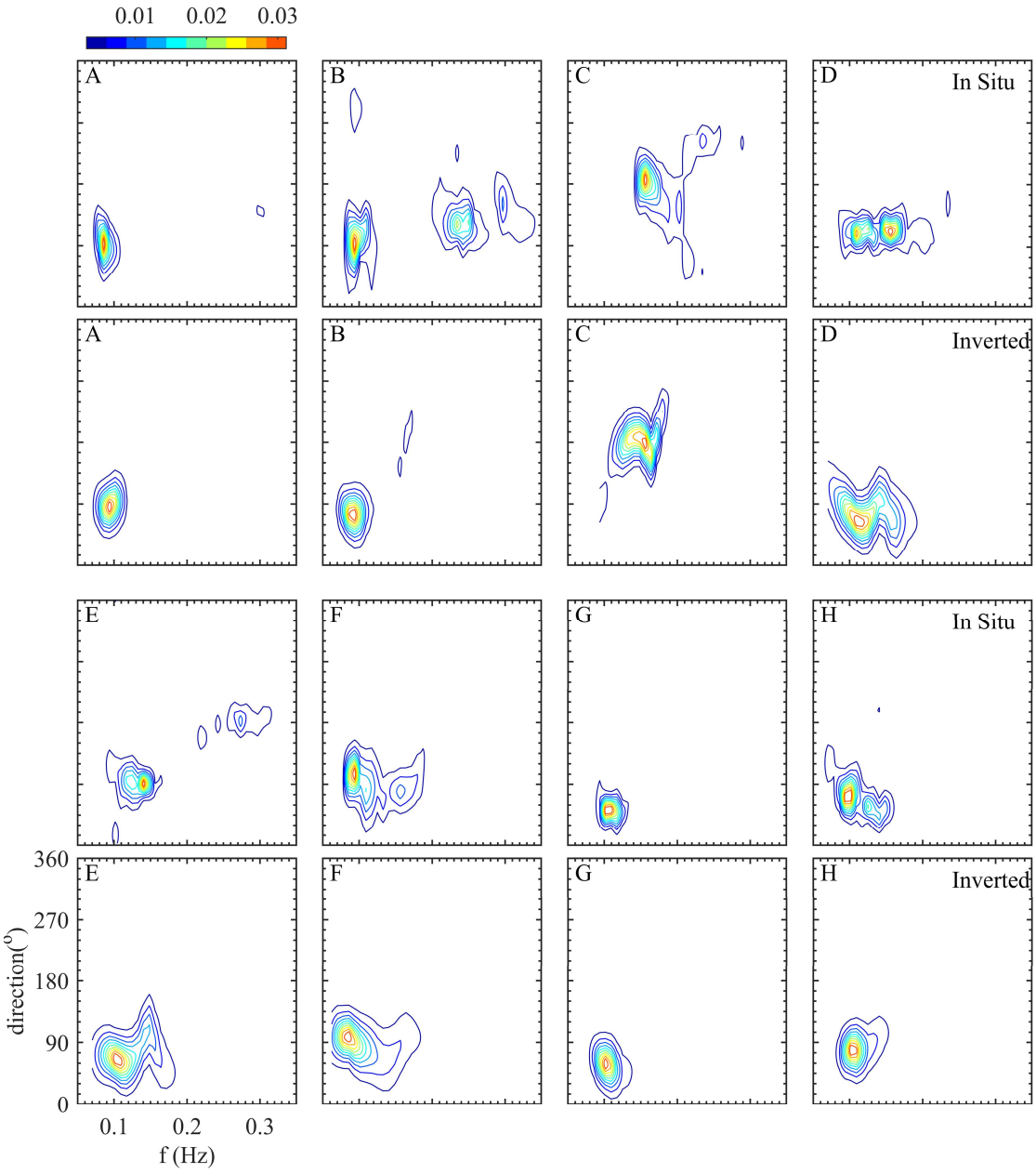

Figure 4.15: Comparison of full directional inverted ($Inv.S(f,\theta)$) and in situ ($In\ Situ.S(f,\theta)$) spectra for events A-H.

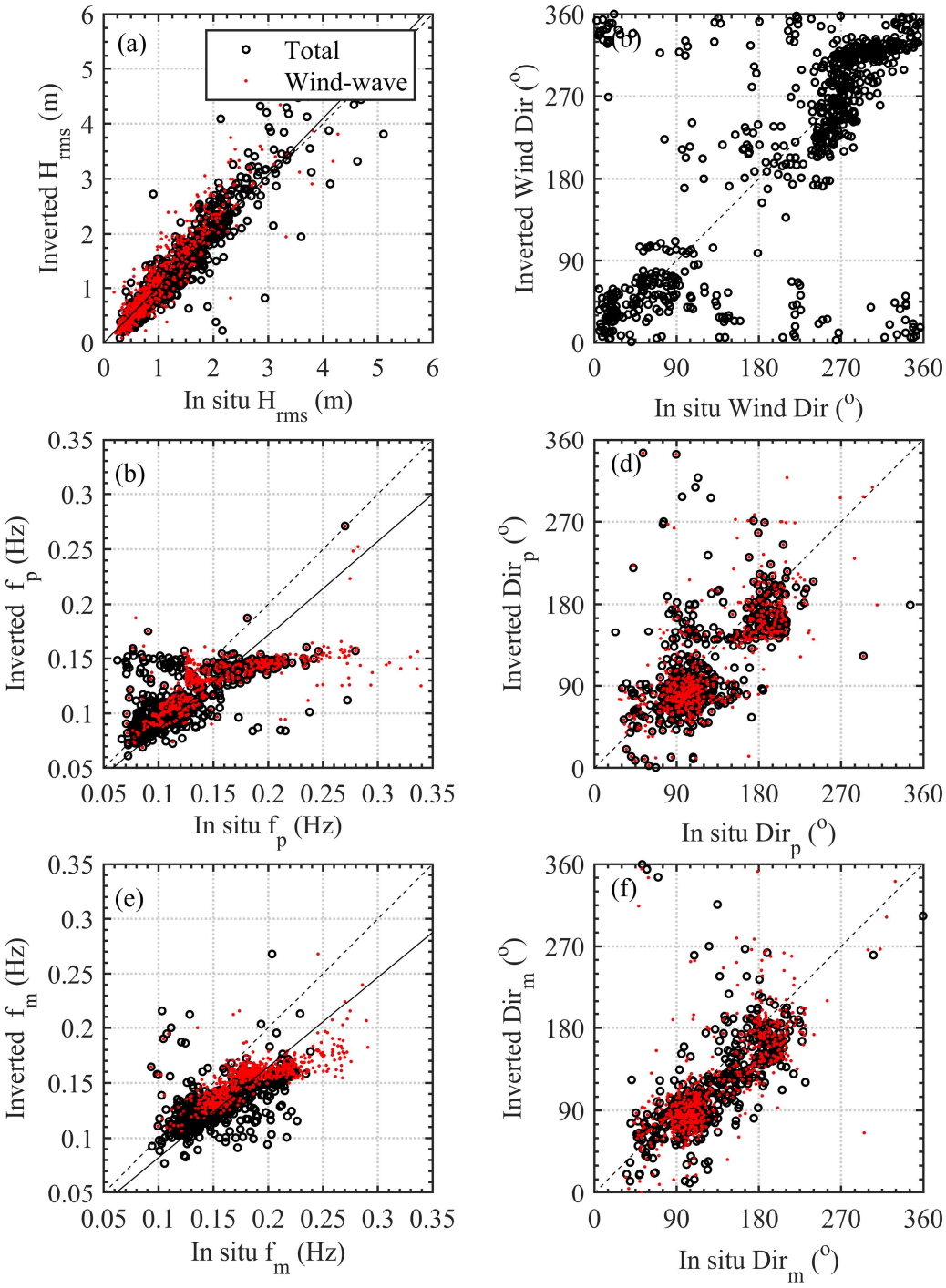

Figure 4.16: Comparison of wave bulk parameters (RMS wave height, (H_{rms}), peak (f_p) and mean (f_m) wave frequency, peak (Dir_p) and mean (Dir_m) wave directions as well as wind direction) using beams from 2 sites (PEN and PER). Black circles represent total (swell and wind waves) while red dots represent wind waves only. The 1:1 (dashed) and the best fit (solid) lines are also shown while the statistics are listed in Table 4.7.

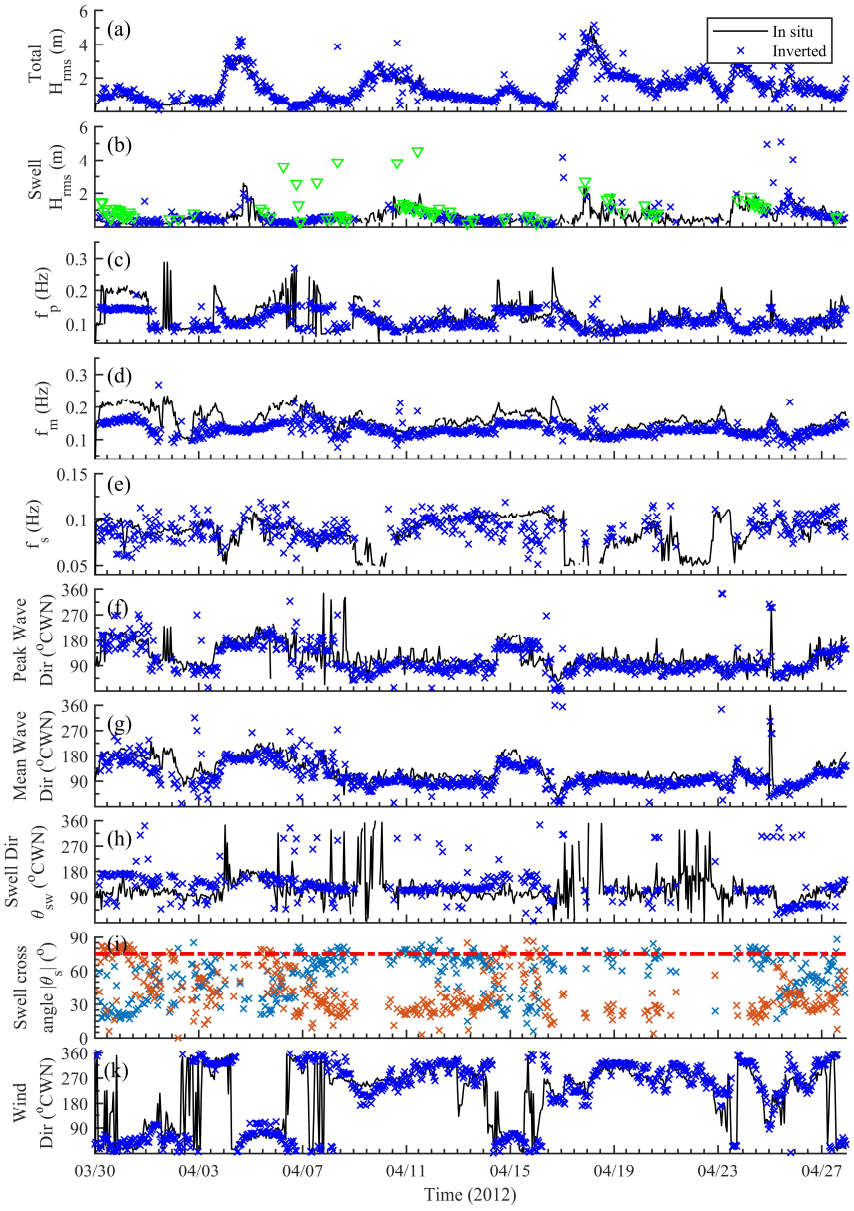

Figure 4.17: Time series comparison of in situ and inverted total and swell wave parameters using data from two sites - two beams ($LPM2_2$ method) including data with swell cross angle $|\theta_s|$ >75°: (a) total (wind and swell) RMS wave height, (b) swell RMS wave height (green triangles denote data when $|\theta_s|$ >75°), (c) peak frequency, (d) mean wave frequency, (e) swell frequency, (f) peak direction, (g) mean wave direction, (h) swell only direction, (i) swell cross angle for PEN (blue) and PER (red) beams, and (k) wind direction. Note that the white gaps in total and swell results are attributed to Doppler spectra that did not pass the quality criteria (see text for details) as well as to cases where no swell was detected by the radar.

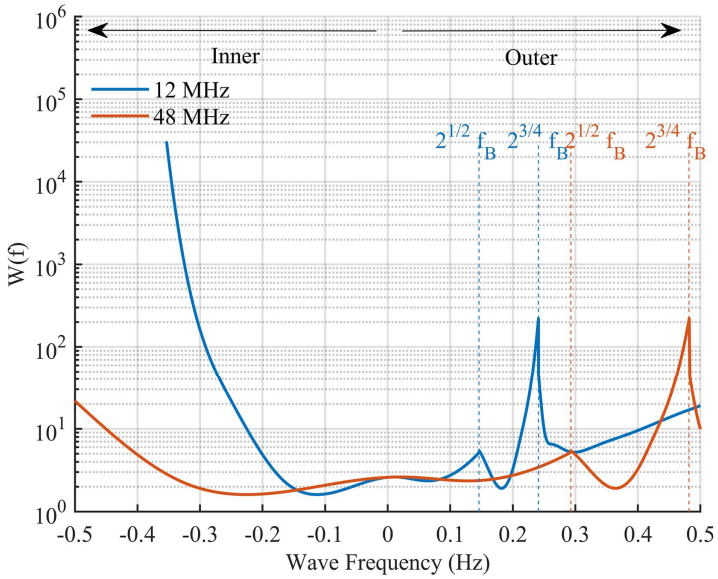

Figure 4.18: Barrick's weighting function for 12 and 48 MHz in term of ocean wave frequency. ''Inner'' and "Outer" refer to second-order sidebands toward the zero Doppler frequency (i.e., left/right of the Bragg peak for positive/negative Doppler frequencies), and toward $\pm\infty$ Doppler frequency (i.e., right/left of the Bragg peak for positive/negative Doppler frequencies), respectively.

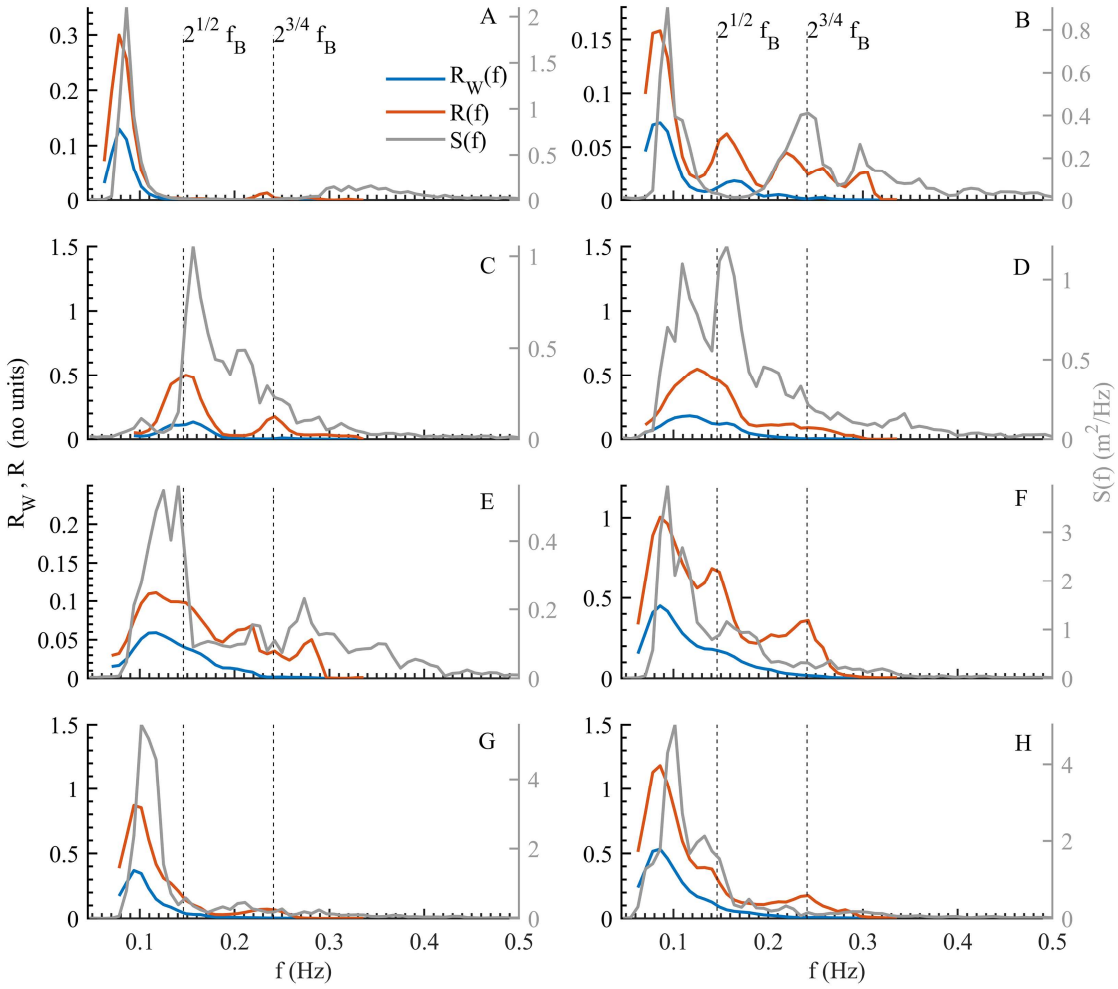

Figure 4.19: Examples from A-H events showing the contribution of the weighting function in reducing the effect of the second harmonic and corner reflection peaks (located at $2^{1/2}f_B$ and $2^{3/4}f_B$, where f_B is the Bragg frequency) in the normalized second-order spectra $R_W(f)$. R is the unweighted normalized second-order spectra, and $S(f)$ denotes in situ wave spectra from wave buoy (m^2/Hz).

CHAPTER 5

CONCLUSIONS

The work presented in this dissertation contributed in enhancing our understanding of the wave inversion methods for HF radar data. The focus was on empirical wave inversion methods that can extract accurate ocean wave information from single and two radar systems and using two different operational frequencies (48 and 12 MHz) and environmental settings (nearshore vs offshore oceanic conditions). This dissertation has shown the capabilities and limitations of HF radars to measure ocean wave conditions using simple semi-empirical wave inversion techniques.

In Chapter 3, a new approach of ocean wave inversion was introduced that treats wind-wave and swell waves separately. The wind-wave spectra inversion utilizes the original empirical method of Barrick (1977b) as adapted by Heron and Heron (1998). The swell spectra were inverted using a rather simplified swell inversion method that was appropriate only for nearshore conditions where swell propagation is nearly normal to the coastline. Data collected over a 22-day period from a single VHF (48 MHz) radar system were used to validate this method against in situ recorded wave conditions measured over a variety of ranges and beam angles within the radar footprint. This work presented the first application of VHF radar (48 MHz) system for ocean wave estimates.

The analysis concluded that the wind-wave inversion module does not require wave frequency dependent regression coefficients as suggested by Gurgel et al. (2006) and Lopez et al. (2016) and implemented in the software supplied by the manufacturer of the WERA systems. Instead, a constant value of 0.255 was estimated, a value similar to those reported by Ramos et al. (2009) and Heron and Heron (1998) using different radar frequencies. It is important to note that this consistency between this and the other studies

is attributed to the use of Barrick's weighting function, which helps suppressing energy from the second harmonic and corner reflection peaks in second-order spectra.

For swell inversion, a separate empirical model is used which for nearshore conditions, where a constant swell cross-angle can be assumed ($\pm 30^{o}$ from perpendicular), does not show a swell wave directional dependance. The inverted wind and swell waves were combined to provide estimates of total wave energy spectra including directional characteristics. The bulk ocean wave parameters estimated from the inverted wave spectra were in good agreement with the in situ data with wave height RMS errors between 0.16-0.25m and with a correlation coefficient ranging from 0.86 to 0.94. Further, it is found that the RMS error of the inverted wave height increases with range, and beam angle from boresight. High RMS error of wave height is found at higher beam angles something attributed to the sidelobe effects.

The accuracy is comparable to results obtained from other studies that used different radar frequencies and theoretical and empirical wave inversion methods. The inverted wave spectra exhibit a high-frequency roll-off range similar to that expected from the theory (f^{-4} to f^{-5}). This is not the case when the inversion does not use the weighting function.

The theoretical limitation criteria suggested by Barrick (1977b) $0.15 < k_0 m_o < 1$ (or $0.42 < k_0 H_{rms} < 2.82$) seem to not always be applicable, as the wave inversion analysis was successful under wave conditions exceeding these limits. Despite the shallow water depths of the study no significant shallow water effects were noted

affecting the evolution of the Doppler spectra as it has been suggested for lower radar frequencies.

Chapter 4 focused more on the swell inversion under offshore oceanic conditions where there were no restrictions on the propagation of the swell. Doppler spectra from two WERA radar sites operated at 12 MHz were used. The separation of wind wave and swell spectra partitioning was automated using the wave age formulation and three swell inversion methods LPM (Lipa et al., 1981), WFG (Wang et al., 2016), and EMP (chapter 3) that allows for swell directionality were evaluated. It was concluded that the LPM method used with the signal from two beams from two sites ($LPM2_2$) provides the most accurate swell wave height estimates, as long as the swell cross-angle is below 75°. The analysis suggested that the swell cross angles $|\theta_s|$ that do not allow the inversion for swell due to singularities vary as function of radar frequency. For radar frequencies of 4, 12, and 48 MHz, singularities occur for swell cross angles $|\theta_s| > 60^o, 75^o$ and 85^o, respectively and a more general relationship is suggested defining the limit of cross-angles where swell inversion is possible: $|\theta_s| < 23 \log_{10}(f_{radar}) + 48$, where f_{radar} is the radar operating frequency in MHz.

Similarly, to the findings using the 48 MHz system the 12 MHz data showed that the empirical wind-wave model does not require a wave frequency dependent coefficient as suggested elsewhere. An averaged value of 0.32 was determined and the value of 0.3 is suggested for use with the model and all radar frequencies.

In this dissertation, it was shown that a 12 MHz system can be used to invert waves with a frequency up to 0.35 Hz instead of 0.25 Hz as in some studies (Wyatt, 2005,

2017; Lopez et al., 2016; Lopez and Conley, 2019) have suggested. In terms of ocean wave spectra and ocean wave parameters estimation, the method presented has shown its ability to accurately estimate one-dimensional wave spectra where both the energy level and peak frequency are in good agreement with in situ data. We found that the error in swell wave height estimations does not depend on the accuracy of the inverted swell frequency and direction, but it significantly depends on how accurately identifying swell peak energies in Doppler spectrum.

The analysis of the wave inversion method has practical implications. It provides an algorithm that can be included in the radar software and use for routine, real time ocean wave observations. Despite the encouraging finding, the ocean wave parameters estimated from radars using this wave inversion method might not accurate enough for scientific research into air-sea interaction and wave studies but certainly suitable for providing wave conditions as auxiliary environmental data for a variety of applications.

Future investigations need to be carried out to develop a more accurate method to estimate swell peak energies that increase the accuracy of estimated swell wave height. The results presented in this dissertation only focus on enhancing the wave inversion method by using radar and in situ data from individual locations in the area studied, Further investigations are suggested to better understanding the limitation of the method and the effect of sidelobes by involving the concept of beam pattern remains unknown. It is required to use simulated wave data over a large radial range and measured beam patterns.

BIBLIOGRAPHY

Alattabi, Z. R., Cahl, D. and Voulgaris, G., 2019. Swell and wind wave inversion using a single Very High Frequency (VHF) radar. *Journal of Atmospheric and Oceanic Technology*, *36*(6), pp.987-1013.

Armstrong, B. N., Warner, J. C., Voulgaris, G., List, J. H., Thieler, R., Martini, M. A., Montgomery, E. T., McNinch, J. E., Book, J. W. and Haas, K., 2013. *Carolinas Coastal Change Processes Project data report for nearshore observations at Cape Hatteras, North Carolina* (No. 2012-1219). US Geological Survey.

Barrick, D. E. and Weber, B. L., 1977. On the nonlinear theory for gravity waves on the ocean's surface. Part II: Interpretation and applications. *Journal of Physical Oceanography*, *7*(1), pp.11-21.

Barrick, D. E., 1971. Theory of HF and VHF propagation across the rough sea, 1, The effective surface impedance for a slightly rough highly conducting medium at grazing incidence. *Radio Science*, *6*(5), pp.517-526.

Barrick, D. E., 1972. First-order theory and analysis of MF/HF/VHF scatter from the sea. *IEEE Transactions on Antennas and Propagation*, *20*(1), pp.2-10.

Barrick, D. E., 1972a. Remote sensing of sea state by radar. In Ocean *72-IEEE International Conference on Engineering in the Ocean Environment* (pp. 186-192). IEEE.

Barrick, D. E., 1977a. The ocean waveheight nondirectional spectrum from inversion of the HF sea-echo Doppler spectrum. *Remote Sensing of Environment*, *6*(3), pp.201-227.

Barrick, D. E., 1977b. Extraction of wave parameters from measured HF radar sea-echo Doppler spectra. *Radio Science*, *12*(3), pp.415-424.

Barrick, D. E., 2008. 30 Years of CMTC and CODAR. In *2008 IEEE/OES 9th Working Conference on Current Measurement Technology* (pp. 131-136). IEEE.

Barrick, D. E., Evans, M. W. and Weber, B. L., 1977. Ocean surface currents mapped by radar. *Science*, *198*(4313), pp.138-144.

Barth, A., Alvera-Azcárate, A. and Weisberg, R. H., 2008. Assimilation of high-frequency radar currents in a nested model of the West Florida Shelf. *Journal of Geophysical Research: Oceans*, *113*(C8).

Bathgate, J. S., Heron, M. L. and Prytz, A., 2006. A method of swell-wave parameter extraction from HF ocean surface radar spectra. *IEEE Journal of Oceanic Engineering*, *31*(4), pp.812-818.

Bidlot, J. R., 2001. ECMWF wave model products. *ECMWF Newsletter*, *91*, pp.9-15.

Bishop, C. T. and Donelan, M. A., 1987. Measuring waves with pressure transducers. *Coastal Engineering*, *11*(4), pp.309-328.

Bjorkstedt, E. and Roughgarden, J., 1997. Larval transport and coastal upwelling: An application of HF radar in ecological research. *Oceanography*, *10*(2), pp.64-67.

Broche, P., Forget, P., De Maistre, J. C., Devenon, J. L. and Crochet, M., 1987. VHF radar for ocean surface current and sea state remote sensing. *Radio Science*, *22*(1), pp.69-75.

Cahl D. and G. Voulgaris, 2019. WavePART V.1.1 MATLAB(r) software for the partition of directional ocean wave spectra.

Cahl, D., G. Voulgaris, and Z. Alattabi, 2019. Wave Radar Inversion Code (WaveRIC) V1.1.1.

Chen, Z., Zezong, C., Yanni, J., Lingang, F. and Gengfei, Z., 2013. Exploration and validation of wave-height measurement using multifrequency HF radar. *Journal of Atmospheric and Oceanic Technology*, *30*(9), pp.2189-2202.

Chen, Z., Zhang, L., Zhao, C., Chen, X. and Zhong, J., 2015. A practical method of extracting wind sea and swell from directional wave spectrum. *Journal of Atmospheric and Oceanic Technology*, *32*(11), pp.2147-2159.

Churchill, J. H., Plueddemann, A. J. and Faluotico, S. M., 2006. *Extracting wind sea and swell from directional wave spectra derived from a bottom-mounted ADCP* (No. WHOI-2006-13). WOODS HOLE OCEANOGRAPHIC INSTITUTION MA.

Collard, F., Ardhuin, F. and Chapron, B., 2005. Extraction of coastal ocean wave fields from SAR images. *IEEE Journal of Oceanic Engineering*, *30*(3), pp.526-533.

Crombie, D. D., 1955. Doppler spectrum of sea echo at 13.56 Mc./s. *Nature*, *175*(4459), pp.681-682.

De Farias, E. G., Lorenzzetti, J. A. and Chapron, B., 2012. Swell and wind-sea distributions over the mid-latitude and Tropical North Atlantic for the period 2002–2008. *International Journal of Oceanography*, *2012*.

Donelan, M. A., Hamilton, J. and Hui, W., 1985. Directional spectra of wind-generated ocean waves. *Philosophical Transactions of the Royal Society of London. Series A, Mathematical and Physical Sciences*, *315*(1534), pp.509-562.

Dzvonkovskaya, A., Gurgel, K.W., Rohling, H. and Schlick, T., 2008, September. Low power high frequency surface wave radar application for ship detection and tracking. In *2008 International Conference on Radar* (pp. 627-632). IEEE.

Earle, M. D., 1984. Development of algorithms for separation of sea and swell. *National Data Buoy Center Tech Rep MEC-87-1, Hancock County*, *53*, pp.1-53.

Essen, H. H., Gurgel, K. W. and Schlick, T., 1999. Measurement of ocean wave height and direction by means of HF radar: an empirical approach. *Deutsche Hydrografische Zeitschrift*, *51*(4), pp.369-383.

Fernandez, D. M., Graber, H. C., Paduan, J. D. and Barrick, D. E., 1997. Mapping wind direction with HF radar. *Oceanography*, *10*(2), pp.93-95.

Forget, P., Broche, P., De Maistre, J. C. and Fontanel, A., 1981. Sea state frequency features observed by ground wave HF Doppler radar. *Radio Science*, *16*(05), pp.917-925.

Gilhousen, D. B. and Hervey, R., 2002. Improved estimates of swell from moored buoys. In *Ocean Wave Measurement and Analysis (2001)* (pp. 387-393).

Gill, E. W. and Walsh, J., 2001. High-frequency bistatic cross sections of the ocean surface. *Radio Science*, *36*(6), pp.1459-1475.

Gill, E. W., 1990. *An algorithm for the extraction of ocean wave parameters from wide beam HF radar (CODAR) backscatter* (Doctoral dissertation, Memorial University of Newfoundland).

Gomez, R., Helzel, T., Wyatt, L., Lopez, G., Conley, D., Thomas, N., Smet, S. and Sicot, G., 2015, May. Estimation of wave parameters from HF radar using different methodologies and compared with wave buoy measurements at the Wave Hub. In *OCEANS 2015-Genova* (pp. 1-9). IEEE.

Gopalakrishnan, G., 2008. *Surface current observations using high frequency radar and its assimilation into the New York Harbor observing and prediction system* (Doctoral dissertation, Stevens Institute of Technology).

Graber, H. C. and Heron, M. L., 1997. Wave height measurements from HF radar. *Oceanography, 10*(2), pp.90-92.

Gurgel, K. W., Antonischki, G. and Schlick, T., 1998. HF radar systems for wave and current measurement. In *Proceedings of Oceanology'98 conference* (pp. 423-433).

Gurgel, K. W., Antonischki, G., Essen, H. H. and Schlick, T., 1999. Wellen Radar (WERA): a new ground-wave HF radar for ocean remote sensing. *Coastal engineering*, *37*(3-4), pp.219-234.

Gurgel, K. W., Dzvonkovskaya, A., Pohlmann, T., Schlick, T. and Gill, E., 2011. Simulation and detection of tsunami signatures in ocean surface currents measured by HF radar. *Ocean Dynamics*, *61*(10), pp.1495-1507.

Gurgel, K. W., Essen, H. H. and Kingsley, S. P., 1999. High-frequency radars: physical limitations and recent developments. *Coastal engineering*, *37*(3-4), pp.201-218.

Gurgel, K. W., Essen, H. H. and Schlick, T., 2003, September. HF surface wave radar for oceanography-a review of activities in Germany. In *2003 Proceedings of the International Conference on Radar (IEEE Cat. No. 03EX695)* (pp. 700-705). IEEE.

Gurgel, K. W., Essen, H. H. and Schlick, T., 2006. An empirical method to derive ocean waves from second-order Bragg scattering: Prospects and limitations. *IEEE Journal of Oceanic Engineering*, *31*(4), pp.804-811.

Gurgel, K.W. and Schlick, T., 2009, September. Remarks on signal processing in HF radars using FMCW modulation. In *Proc. IRS* (pp. 1-5).

Guymer, T. H., 1990. Measuring ocean waves with altimeters and synthetic aperture radars. In *Microwave Remote Sensing for Oceanographic and Marine Weather-Forecast Models* (pp. 65-97). Springer, Dordrecht.

Hammond, T. M., Pattiaratchi, C. B., Eccles, D., Osborne, M. J., Nash, L. A. and Collins, M. B., 1987. Ocean surface current radar (OSCR) vector measurements on the inner continental shelf. *Continental Shelf Research*, *7*(4), pp.411-431.

Hanna, S. R. and Heinold, D. W., 1985. *Development and application of a simple method for evaluating air quality models* (No. 4409). American Petroleum Institute.

Hanson, J. L. and Phillips, O. M., 2001. Automated analysis of ocean surface directional wave spectra. *Journal of atmospheric and oceanic technology*, *18*(2), pp.277-293.

Hasselmann, D. E., Dunckel, M. and Ewing, J. A., 1980. Directional wave spectra observed during JONSWAP 1973. *Journal of physical oceanography*, *10*(8), pp.1264-1280.

Hasselmann, K., 1971. Determination of ocean wave spectra from Doppler radio return from the sea surface. *Nature Physical Science*, *229*(1), pp.16-17.

Hasselmann, K., Barnett, T. P., Bouws, E., Carlson, H., Cartwright, D. E., Enke, K., Ewing, J. A., Gienapp, H., Hasselmann, D. E., Kruseman, P. and Meerburg, A., 1973. Measurements of wind-wave growth and swell decay during the Joint North Sea Wave Project (JONSWAP). *Ergänzungsheft 8-12*.

Haus, B. K., Shay, L. K., Work, P. A., Voulgaris, G., Ramos, R. J. and Martinez-Pedraja, J., 2010. Wind speed dependence of single-site wave-height retrievals from high-frequency radars. *Journal of Atmospheric and Oceanic Technology*, *27*(8), pp.1381-1394.

Helzel, T. and Kniephoff, M., 2010, September. Software beam forming for ocean radar WERA features and accuracy. In *OCEANS 2010 MTS/IEEE SEATTLE* (pp. 1-3). IEEE.

Herbers, T. H. C., Elgar, S. and Guza, R. T., 1999. Directional spreading of waves in the nearshore. *Journal of Geophysical Research: Oceans*, *104*(C4), pp.7683-7693.

Heron, M. and Rose, R., 1986. On the application of HF ocean radar to the observation of temporal and spatial changes in wind direction. *IEEE journal of oceanic engineering*, *11*(2), pp.210-218.

Heron, M. L. and Prytz, A., 2002. Wave height and wind direction from the HF coastal ocean surface radar. *Canadian journal of remote sensing*, *28*(3), pp.385-393.

Heron, M. L., Dexter, P. E. and McGann, B. T., 1985. Parameters of the air-sea interface by high-frequency ground-wave Doppler radar. *Marine and Freshwater Research*, *36*(5), pp.655-670.

Heron, S. F. and Heron, M. L., 1998. A comparison of algorithms for extracting significant wave height from HF radar ocean backscatter spectra. *Journal of Atmospheric and oceanic technology*, *15*(5), pp.1157-1163.

Hessner, K. and Hanson, J. L., 2010. Extraction of coastal wavefield properties from X-band radar. In *2010 IEEE International Geoscience and Remote Sensing Symposium* (pp. 4326-4329). IEEE.

Hildebrand, P. H. and Sekhon, R. S., 1974. Objective determination of the noise level in Doppler spectra. *Journal of Applied Meteorology*, *13*(7), pp.808-811.

Hisaki, Y., 1996. Nonlinear inversion of the integral equation to estimate ocean wave spectra from HF radar. *Radio science*, *31*(1), pp.25-39.

Hisaki, Y., 2016. Ocean wave parameters and spectrum estimated from single and dual high-frequency radar systems. *Ocean Dynamics*, *66*(9), pp.1065-1085.

Howell, R. and Walsh, J., 1993. Measurement of ocean wave spectra using narrow-beam HE radar. *IEEE Journal of Oceanic Engineering*, *18*(3), pp.296-305.

Ivonin, D. V., Shrira, V. I. and Broche, P., 2006. On the singular nature of the second-order peaks in HF radar sea echo. *IEEE Journal of Oceanic Engineering*, *31*(4), pp.751-767.

Jackson, F. C., 1981. An analysis of short pulse and dual frequency radar techniques for measuring ocean wave spectra from satellites. *Radio science*, *16*(06), pp.1385-1400.

Kirincich, A., Emery, B., Washburn, L. and Flament, P., 2019. Improving Surface Current Resolution Using Direction Finding Algorithms for Multiantenna High-Frequency Radars. *Journal of Atmospheric and Oceanic Technology*, *36*(10), pp.1997-2014.

Kumar, N., 2011: Advancing Land-based Directional Wave Measurements using Beamforming HF radars (unpublished).

Kumar, N., Cahl, D. L., Crosby, S. C. and Voulgaris, G., 2017. Bulk versus spectral wave parameters: Implications on stokes drift estimates, regional wave modeling, and HF radars applications. *Journal of Physical Oceanography*, *47*(6), pp.1413-1431.

Kumar, N., Voulgaris, G., List, J. H. and Warner, J. C., 2013. Alongshore momentum balance analysis on a cuspate foreland. *Journal of Geophysical Research: Oceans*, *118*(10), pp.5280-5295.

Kundu, P. K., 1976. Ekman veering observed near the ocean bottom. *Journal of Physical Oceanography*, *6*(2), pp.238-242.

Laws, K., 2001. *Measurements of near surface ocean currents using HF radar* (Doctoral dissertation, University of California, Santa Cruz).

Limouzy-Paris, C. B., Graber, H. C., Jones, D. L., Röpke, A. W. and Richards, W. J., 1997. Translocation of larval coral reef fishes via sub-mesoscale spin-off eddies from the Florida Current. *Bulletin of Marine Science*, *60*(3), pp.966-983.

Lipa, B. J. and Barrick, D. E., 1980. Methods for the extraction of long-period ocean wave parameters from narrow beam HF radar sea echo. *Radio Science*, *15*(4), pp.843-853.

Lipa, B. J. and Barrick, D. E., 1982. CODAR measurements of ocean surface parameters at ARSLOE--Preliminary results. In *OCEANS 82* (pp. 901-906). IEEE.

Lipa, B. J. and Barrick, D. E., 1983. Least-squares methods for the extraction of surface currents from CODAR crossed-loop data: Application at ARSLOE. *IEEE Journal of Oceanic Engineering*, *8*(4), pp.226-253.

Lipa, B. J., 1977. Derivation of directional ocean-wave spectra by integral inversion of second-order radar echoes. *Radio Science*, *12*(3), pp.425-434.

Lipa, B. J., 1978. Inversion of second-order radar echoes from the sea. *Journal of Geophysical Research: Oceans*, *83*(C2), pp.959-962.

Lipa, B. J., Barrick, D. E. and Maresca Jr, J. W., 1981. HF radar measurements of long ocean waves. *Journal of Geophysical Research: Oceans*, *86*(C5), pp.4089-4102.

Lipa, B. J., Nyden, B., Barrick, D. E. and Kohut, J., 2008. HF radar sea-echo from shallow water. *Sensors*, *8*(8), pp.4611-4635.

List, J. H., Warner, J. C., Thieler, E. R., Haas, K., Voulgaris, G., McNinch, J. E. and Brodie, K. L., 2011. A nearshore processes field experiment at Cape Hatteras, North Carolina, USA. In *The Proceedings of the Coastal Sediments 2011: In 3 Volumes* (pp. 2144-2157).

Long, A. and Trizna, D., 1973. Mapping of North Atlantic winds by HF radar sea backscatter interpretation. *IEEE Transactions on Antennas and Propagation*, *21*(5), pp.680-685.

Longuet-Higgins, M.S., 1963. The effect of non-linearities on statistical distributions in the theory of sea waves. *Journal of fluid mechanics*, *17*(3), pp.459-480.

Lopez, G. and Conley, D. C., 2019. Comparison of HF radar fields of directional wave spectra against in situ measurements at multiple locations. *Journal of Marine Science and Engineering*, *7*(8), p.271.

Lopez, G., Conley, D. C. and Greaves, D., 2016. Calibration, validation, and analysis of an empirical algorithm for the retrieval of wave spectra from HF radar sea echo. *Journal of Atmospheric and Oceanic Technology*, *33*(2), pp.245-261.

Maresca Jr, J. W. and Georges, T. M., 1980. Measuring rms wave height and the scalar ocean wave spectrum with HF skywave radar. *Journal of Geophysical Research: Oceans*, *85*(C5), pp.2759-2771.

Mentaschi, L., Besio, G., Cassola, F. and Mazzino, A., 2013. Problems in RMSE-based wave model validations. *Ocean Modelling*, *72*, pp.53-58.

Middleditch, A., 2013. Spatiotemporal spectral averaging of High-Frequency radar wave data. *Report for ARC Linkage project: Wave Climate in the Southern Great Barrier Reef*.

Molcard, A., Poulain, P.M., Forget, P., Griffa, A., Barbin, Y., Gaggelli, J., De Maistre, J.C. and Rixen, M., 2009. Comparison between VHF radar observations and data from drifter clusters in the Gulf of La Spezia (Mediterranean Sea). *Journal of Marine Systems*, *78*, pp.S79-S89.

Paduan, J. D. and Rosenfeld, L. K., 1996. Remotely sensed surface currents in Monterey Bay from shore-based HF radar (Coastal Ocean Dynamics Application Radar). *Journal of Geophysical Research: Oceans*, *101*(C9), pp.20669-20686.

Paduan, J. D. and Shulman, I., 2004. HF radar data assimilation in the Monterey Bay area. *Journal of Geophysical Research: Oceans*, *109*(C7).

Paduan, J. D. and Washburn, L., 2013. High-frequency radar observations of ocean surface currents. *Annual review of marine science*, *5*, pp.115-136.

Phillips, O. M., 1966. *The dynamics of the upper ocean*. Cambridge university press.

Quentin, C. G., 2002. *Etude de la surface océanique, de sa signature radar et de ses interactions avec les flux turbulents de quantité de mouvement dans le cadre de l'experience FETCH* (Doctoral dissertation in French).

Ramos, R. J., 2006. *2-D analysis of wave energy evolution using wavelet transforms* (Doctoral dissertation, Ph. D. dissertation, RSMAS/Applied Marine Physics Department, University of Miami).

Ramos, R. J., Graber, H. C. and Haus, B. K., 2009. Observation of wave energy evolution in coastal areas using HF radar. *Journal of Atmospheric and Oceanic Technology*, *26*(9), pp.1891-1909.

Saviano, S., Kalampokis, A., Zambianchi, E. and Uttieri, M., 2019. A year-long assessment of wave measurements retrieved from an HF radar network in the Gulf of Naples (Tyrrhenian Sea, Western Mediterranean Sea). *Journal of Operational Oceanography*, *12*(1), pp.1-15.

Savidge, D., Amft, J., Gargett, A., Archer, M., Conley, D., Voulgaris, G., Wyatt, L. and Gurgel, K.W., 2011, March. Assessment of WERA long-range HF-radar performance from the user's perspective. In *2011 IEEE/OES 10th Current, Waves and Turbulence Measurements (CWTM)* (pp. 31-38). IEEE.

Shay, L. K., Cook, T. M., Peters, H., Mariano, A. J., Weisberg, R., An, P. E., Soloviev, A. and Luther, M., 2002. Very high-frequency radar mapping of surface currents. *IEEE Journal of Oceanic Engineering*, *27*(2), pp.155-169.

Shen, C., Gill, E. and Huang, W., 2012. Simulation of HF radar cross sections for swell contaminated seas. In *2012 Oceans* (pp. 1-5). IEEE.

Shen, C., Gill, E. and Huang, W., 2013. Extraction of swell parameters from simulated noisy HF radar signals. In *2013 IEEE Radar Conference (RadarCon13)* (pp. 1-6). IEEE.

Shrira, V. I., Ivonin, D. V., Broche, P. and de Maistre, J. C., 2001. On remote sensing of vertical shear of ocean surface currents by means of a Single-frequency VHF radar. *Geophysical research letters*, *28*(20), pp.3955-3958.

Srivastava, S. K. and Ponsford, A. M., 1991. Long Range Detection Of Iceberg Using Ground Wave Radar. In *The First International Offshore and Polar Engineering Conference. International Society of Offshore and Polar Engineers*.

Stewart, R. H. and Barnum, J. R., 1975. Radio measurements of oceanic winds at long ranges: An evaluation. *Radio Science*, *10*(10), pp.853-857.

Stewart, R., 1971. Higher order scattering of radio waves from the sea. In *1971 Antennas and Propagation Society International Symposium* (Vol. 9, pp. 190-193). IEEE.

Teague, C. C., Vesecky, J. F. and Fernandez, D. M., 1997. HF radar instruments, past to present. *Oceanography*, *10*(2), pp.40-44.

Toro, V. G., Ocampo-Torres, F. J., Osuna, P., García-Nava, H., Flores-Vidal, X. and Durazo, R., 2014. Analysis of fetch-limited wave growth using high-frequency radars in the Gulf of Tehuantepec. *Ciencias Marinas*, *40*(2), pp.113-132.

Tracy, B., Devaliere, E.M., Hanson, J., Nicolini, T. and Tolman, H., 2007, November. Wind sea and swell delineation for numerical wave modeling. In *10th international workshop on wave hindcasting and forecasting & coastal hazards symposium, JCOMM Tech. Rep* (Vol. 41, p. 1442).

Venugopal, V., Davey, T., Smith, H., Smith, G., Holmes, B., Barrett, S., Prevosto, M., Maisondieu, C., Cavalieri, L., Bertotti, L. and Lawrence, J., 2011. EquiMar. Deliverable D2. 2. Wave and tidal resource characterisation.

Voulgaris, G., Haus, B. K., Work, P., Shay, L. K., Seim, H. E., Weisberg, R. H. and Nelson, J. R., 2008. Waves initiative within SEACOOS. Marine *Technology Society Journal*, *42*(3), pp.68-80.

Voulgaris, G., Kumar, N., Gurgel, K. W., Warner, J. C. and List, J. H., 2011, March. 2-D inner-shelf current observations from a single VHF WEllen RAdar (WERA) station. In *2011 IEEE/OES 10th Current, Waves and Turbulence Measurements (CWTM)* (pp. 57-65). IEEE.

Wang, W. and Gill, E.W., 2016. Evaluation of beamforming and direction finding for a phased array HF ocean current radar. *Journal of Atmospheric and Oceanic Technology*, *33*(12), pp.2599-2613.

Wang, W., Forget, P. and Guan, C., 2014. Inversion of swell frequency from a 1-year HF radar dataset collected in Brittany (France). *Ocean Dynamics*, *64*(10), pp.1447-1456.

Wang, W., Forget, P. and Guan, C., 2016. Inversion and assessment of swell waveheights from HF radar spectra in the Iroise Sea. *Ocean Dynamics*, *66*(4), pp.527-538.

Waters, J., Wyatt, L. R., Wolf, J. and Hines, A., 2013. Data assimilation of partitioned HF radar wave data into Wavewatch III. *Ocean Modelling*, *72*, pp.17-31.

Weber, B. L. and Barrick, D. E., 1977. On the nonlinear theory for gravity waves on the ocean's surface. Part I: Derivations. *Journal of Physical Oceanography*, *7*(1), pp.3-10.

Welch, P., 1967. The use of fast Fourier transform for the estimation of power spectra: a method based on time averaging over short, modified periodograms. *IEEE Transactions on audio and electroacoustics*, *15*(2), pp.70-73.

WMO, 1998. Guide to Wave analysis and forecasting. (2nd Edition) WMO-No. 702. World Meteorological Organization. 152pp

Work, P. A., 2008. Nearshore directional wave measurements by surface-following buoy and acoustic Doppler current profiler. *Ocean Engineering*, *35*(8-9), pp.727-737.

Wu, X., Voulgaris, G. and Kumar, N., 2017. Parameterization of synoptic weather systems in the South Atlantic Bight for modeling applications. *Ocean Dynamics*, *67*(10), pp.1231-1249.

Wyatt, L. R., 1986. The measurement of the ocean wave directional spectrum from HF radar Doppler spectra. *Radio science*, *21*(3), pp.473-485.

Wyatt, L. R., 1990. A relaxation method for integral inversion applied to HF radar measurement of the ocean wave directional spectrum. *International Journal of Remote Sensing*, *11*(8), pp.1481-1494.

Wyatt, L. R., 1999. HF radar measurements of the development of the directional wave spectrum. *The Wind-Driven Air-Sea Interface, ed ML Banner, pub School of Mathematics, University of New South Wales, Australia*, pp.433-440.

Wyatt, L. R., 2000. Limits to the inversion of HF radar backscatter for ocean wave measurement. *Journal of Atmospheric and Oceanic Technology*, *17*(12), pp.1651-1666.

Wyatt, L. R., 2002. An evaluation of wave parameters measured using a single HF radar system. *Canadian Journal of Remote Sensing*, *28*(2), pp.205-218.

Wyatt, L. R., 2005, June. HF radar for coastal monitoring-a comparison of methods and measurements. In *Europe Oceans 2005* (Vol. 1, pp. 314-318). IEEE.

Wyatt, L. R., 2007, June. Wave and Tidal Power measurement using HF radar. In *Oceans 2007-Europe* (pp. 1-5). IEEE.

Wyatt, L. R., 2017, June. Wave power measurements in the Celtic Sea using HF radar. In *OCEANS 2017-Aberdeen* (pp. 1-4). IEEE.

Wyatt, L. R., Green, J. J. and Middleditch, A., 2009. Signal sampling impacts on HF radar wave measurement. *Journal of Atmospheric and Oceanic Technology*, *26*(4), pp.793-805.

Wyatt, L. R., Green, J. J. and Middleditch, A., 2011. HF radar data quality requirements for wave measurement. *Coastal Engineering*, *58*(4), pp.327-336.

Wyatt, L. R., Green, J. J., Binks, L. A., Moorhead, M. and Holt, M., 2003. Performance of the PISCES HF radar during the DEFRA trials. In *Elsevier Oceanography Series* (Vol. 69, pp. 161-167). Elsevier.

Wyatt, L. R., Green, J. J., Middleditch, A., Moorhead, M. D., Howarth, J., Holt, M. and Keogh, S., 2006. Operational wave, current, and wind measurements with the Pisces HF radar. *IEEE Journal of Oceanic Engineering*, *31*(4), pp.819-834.

Wyatt, L. R., Liakhovetski, G., Graber, H. C. and Haus, B. K., 2005. Factors affecting the accuracy of SHOWEX HF radar wave measurements. *Journal of Atmospheric and Oceanic Technology*, *22*(7), pp.847-859.

Young, I. R. and Verhagen, L. A., 1996. The growth of fetch limited waves in water of finite depth. Part 1. Total energy and peak frequency. *Coastal Engineering*, *29*(1-2), pp.47-78.

Young, I. R., 1995. The determination of confidence limits associated with estimates of the spectral peak frequency. *Ocean engineering*, *22*(7), pp.669-686.

Zhang, J. and Gill, E. W., 2006. Extraction of ocean wave spectra from simulated noisy bistatic high-frequency radar data. *IEEE Journal of Oceanic Engineering*, *31*(4), pp.779-796.

APPENDIX A

COPYRIGHT PERMISSIONS

Earth, Ocean and Environment

Zaid Rahman <zrahman@geol.sc.edu>

Permission Letter

Gumbel, Erin <egumbel@ametsoc.org> Mon, Sep 14, 2020 at 3:50 PM
To: Zaid Rahman <zrahman@geol.sc.edu>
Cc: permissions <permissions@ametsoc.org>

Dear Zaid,

Thank you for your email. This signed message constitutes permission to use the material requested below.

You may include your 2019 JTECH article in your dissertation with the following conditions:

1. Include the complete bibliographic citation of the original source.
2. Include the following statement with that citation: © **American Meteorological Society. Used with permission.**

Best wishes on completing your dissertation. If you have any questions or need additional information, please feel free to contact me.

Please note: If the material in an AMS journal is credited to another source, the requester must obtain permission or license from that source directly. That material may not be used without permission or license from the copyright holder.

Best,

Ms. Erin Gumbel, she/her/hers
Senior Peer Review Support Assistant
Senior Permissions Specialist
egumbel@ametsoc.org
617-226-3926

AMS
American Meteorological Society